Active Nematics for Living Matter: From Topological Defects to Tissue Organisation



Liam Julian Ruske

St Anne's College

University of Oxford

This dissertation is submitted for the degree of

Doctor of Philosophy in Theoretical Physics

March 2023

Abstract

Living matter describes systems which convert chemical energy from their surroundings to grow or to generate active forces. Biological tissues are composed of many anisotropic and active cells, which can exhibit nematic long-range orientational order. The continuous injection of energy on the single-cell level can lead to complex flow patterns on the tissue scale and topological defects in the cell orientation field. This thesis explores different applications of active nematic theories to living systems. By including key biological features in active hydrodynamic models, we investigate the interplay between collective flows, shape formation and topological defects in two- and three-dimensional tissues.

Using continuum simulations, we investigate the morphology of active, self-deforming cell aggregates, where cell-generated active stress drives flows which can deform the surface. The resulting shape dynamics, such as the formation of finger-like protrusions, surface wrinkles or invagination, are reminiscent of many biological processes, ranging from morphogenesis to collective cancer invasion. We explore how spatial variations of active stress affect the dynamics in active nematic systems. We find that activity gradients induce forces which cause cell orientations and topological defects to preferentially align along a particular direction. Based on these results, we subsequently investigate multicellular spheroids, which are spherical cell clusters widely used as model systems for studying tumor dynamics. The competition over limited resources within spheroids generates proliferation gradients, leading to radial cell flows and activity gradients, both of which can affect the orientation axis of cells. As a result, distinct cell alignment patterns emerge within aggregates, which allows us to infer dynamical tissue parameters for different cell types based on experimental measurements of cell orientations inside spheroids. Finally, we motivate a continuum model for two-dimensional tissues, in which the direction of active stress is decoupled from the orientation axis of cell shape. We show that misalignment between active forces and cell shapes in tissues is linked to topological defects in the cell orientation field, both in simulations and experiments. This suggests that the direction of active stress can vary continuously within tissues, which challenges the underlying assumptions of some widely used tissue models.

This thesis demonstrates how physical continuum models of active materials can help us to understand shape formation and collective cell organisation in living matter.

To my parents, Anja and Thomas

Acknowledgements

First and foremost, I would like to thank my supervisor, Prof. Julia Mary Yeomans, for her constant guidance and support during my time in Oxford and abroad. I am very grateful that I had the opportunity to freely pursue my own research interests, while you were always there to help me putting things into perspective and not losing sight of the bigger picture. Above all, you have taught me to always keep in mind why we are doing things and why they matter.

I would also like to thank all the people who have made life in the Physics Department so much more enjoyable. This includes all the members of the Yeomans group and my office mates over the years, in particular Saraswat Bhattacharyya, Ioannis Hadjifrangiskou, Samantha Lish, Muriel van der Laan, Francesco Mori, Mehrana Nejad and Jan Rozman. I really enjoyed our social meetings and loved discussing random (and sometimes even scientific) topics during the coffee breaks. Special thanks to R0k Medves, for frequently joining me to enjoy classical and not-so-classical music, and to Saraswat, for dragging me to the airfield once in a while.

My time in Oxford certainly would not have been the same without my friends from 41 Stockmore: Nicolas Garraud, Daniel Hortelano, Svenja Küchenhoff and Augustin Vanrietvelde. Thanks to all of you for making our flat a beautiful and cosy place to live, with lovely conversations, board games, movie nights, dinners and Mario Kart. I will dearly miss that.

Finally, I would like to thank my parents, Anja and Thomas, who laid the foundation for my early interest in science and mathematics and enabled me to study physics in the first place. Thank you for your unconditional support.

Publications

Authored publications contributing to this thesis

- Ruske, L. J. & Yeomans, J. M. Morphology of active deformable 3D droplets. *Physical Review X* **11,** 021001 (2021)
- Ruske, L. J. & Yeomans, J. M. Activity gradients in two-and three-dimensional active nematics. *Soft Matter* **18,** 5654–5661 (2022)
- Ruske, L. J. & Yeomans, J. M. Activity-driven tissue alignment in proliferating spheroids. *Soft Matter* **19,** 921–931 (2023)
- Ruske, L. J. *et al.* Topological defects drive stress-shape misalignment in confluent cell layers (in preparation)

During my DPhil I also worked on related topics, including the following:

- Hadjifrangiskou, I. *et al.* Active nematics with deformable particle (in preparation)
- Ruske, L. J. *et al.* Coupled differentiation and division of embryonic stem cells inferred from clonal snapshots. *Physical Biology* **17,** 065009 (2020)

Contents

1 Introduction **1**

2 A brief introduction to active nematics **5**

2.1 Phase-separation and multiphase flows in isotropic fluids 6

2.1.1 The Navier-Stokes equations 6

2.1.2 The Cahn-Hillard equation 7

2.2 Adding anisotropy: Liquid crystals 8

2.2.1 The nematic order parameter 9

2.2.2 The free energy of liquid crystals 11

2.2.3 Discontinuities in the director field 15

2.2.4 Nematohydrodynamics 18

2.3 Adding activity: Active nematics 20

2.3.1 The origin of active stress 21

2.3.2 Active turbulence 22

2.4 Conclusion 25

3 Active matter under soft confinement **26**

3.1 Introduction 27

3.2 Simulation method 29

3.2.1 Membrane free energy 30

3.2.2 Mapping of simulation parameters to experimental values . . 30

3.3 Active surface anchoring 32

3.4 Disclination line dynamics in spherical droplets 35

3.4.1 Defect nucleation and twist-angles in the presence of a surface 37

3.4.2 Characteristic length-scales in 3D active turbulence 37

3.4.3 Self-propulsion of line segments 39

3.5 Activity-induced droplet deformations 40

3.5.1 Extensile droplets 40

3.5.2 Contractile droplets 45

3.6 Summary and Discussion 51

4 Concerning activity gradients **54**
4.1 Introduction . . . 55
4.2 Simulation method . . . 56
4.3 Active forces in the absence of defects . . . 57
4.4 Active turbulence in 2D systems . . . 59
4.4.1 Cross-over to active turbulence . . . 59
4.4.2 Polarization of +1/2 defects . . . 60
4.5 Active turbulence in 3D systems . . . 64
4.5.1 Average director field alignment . . . 64
4.5.2 Polarization of disclination lines . . . 66
4.6 Summary and Discussion . . . 68

5 Application I: Proliferating multicellular spheroids **70**
5.1 Introduction . . . 71
5.2 Governing equations . . . 72
5.3 Simulation method . . . 74
5.3.1 Mapping of simulation parameters to experimental values . . . 75
5.4 Growth-induced converging cell flows . . . 76
5.5 Growth-induced activity gradients . . . 80
5.6 Interplay between converging cell flows and activity gradients . . . 84
5.6.1 Cell orientation inside spheroids . . . 84
5.6.2 Spheroid rotation and dancing disclinations . . . 86
5.7 Parameter inference for biological systems . . . 89
5.7.1 Estimating tissue parameters . . . 89
5.7.2 Inference of the flow-alignment parameter . . . 90
5.8 Summary and Discussion . . . 92

6 Application II: Decoupling cell orientation and active forces **95**
6.1 Introduction . . . 96
6.2 Governing equations . . . 97
6.2.1 Biological Motivation . . . 97
6.2.2 Coupling director fields for cell shape and stress fibres . . . 99
6.3 Simulation method . . . 101
6.4 Flow-driven misalignment between cell orientation and forces . . . 101
6.4.1 Spatial misalignment patterns . . . 101
6.4.2 Topological defects . . . 102
6.4.3 Comparison to biological experiments . . . 105
6.5 Summary and Discussion . . . 105

7 Discussion **107**
7.1 Summary 107
7.2 Outlook 109

Appendices

A The hybrid lattice Boltzmann algorithm **114**
A.1 Background 114
A.2 The lattice Boltzmann equation 115
A.3 Finite-difference method 117

B Detection of topological defects and disclination lines **119**
B.1 2D topological defects 119
B.2 3D disclination lines 119

C Additional information and measurements **122**
C.1 Phase-field modelling of biological membranes 122
C.2 Active and passive torques acting on defects 124
C.3 Stability analysis of isotropic spheroids 127

References **128**

1 Introduction

Cells are the fundamental building blocks of life, and their ability to generate active forces and coordinate their motion plays a crucial role in tissue organisation. Collective cell motion plays an important role in many biological processes, including embryonic development, cancer metastasis and wound healing. Because a cell's motion in dense tissues is strongly constrained by its neighbours, remodelling biological structures often requires tissues to locally flow like a fluid while maintaining overall mechanical integrity like a solid. This leads to glassy dynamics in 2D [7] and 3D [8] cell collectives and it has been shown that many biological tissues can switch from a solid-like to a fluid-like state [9, 10]. This unjamming transition is believed to influence tissue remodelling in asthma [10], tumour progression [11] and morphogenesis, the process of tissue shape formation during embryonic development [12, 13]. Unlike in passive granular materials [14], the jamming transition in confluent tissues happens at constant density since there are no gaps between cells. The solid-to-liquid transition in tissues is driven by *active*, cell-generated forces, such as cell motility [15], cell division and death [16] or active contractions of the cell's actomyosin cortex [17, 18].

Rather than moving individually, cells in tissues often coordinate their motion by interacting with their surroundings via cell–cell junctions or mechanosensitive adhesion complexes at the cell–substrate interface [19, 20]. Therefore, the collective

motion of cells inside dense aggregates can be described in a continuum limit, where the local concentration, orientation and direction of motion of cells are defined by coarse-grained, continuous fields. Several theoretical frameworks have been developed over the years to study this type of collective behaviour. One continuum theory in particular has been successfully used to model the dynamics in a variety of active matter systems: *Active Nematics*.

Active nematic fluids have recently received considerable attention in the physics community because of their potential in designing mesoscopic engines, as examples of non-equilibrium statistical physics, and as a way of interpreting biological mechanics [21–24]. The archetypal experimental example is microtubules driven by kinesin motor proteins [25, 26]. Other active nematics include myosin-driven actin-microtubule networks [27], shaken granular rods [28], bacterial biofilms [29] and confluent monolayers of eukaryotic cells [30–34].

The theory of active nematics describes flows and orientations of anisotropic particles in dense systems with hydrodynamic interactions. The orientational dynamics of particles in passive fluids can be described by the physics of nematic liquid crystals. Active particles, such as cells, continuously take energy from their environment in the form of chemical energy and convert it into mechanical stress which drives the system out of equilibrium. A key property of active nematics, which distinguishes them from passive liquid crystals, is that the continuous injection of energy can lead to active turbulence. This is a chaotic flow state characterised by strong vorticity and motile topological defects, which are points at which domains of different particle orientations meet and the nematic order is frustrated. Topological defects in two-dimensional systems are singular points, but in three dimensions they typically form continuous lines which span the system, called disclination lines. Unlike in passive systems, where topological defects and disclination lines tend to annihilate over time, in active systems there is a finite number of defects at steady-state with some defect types moving through the fluid like self-propelled particles [35, 36]. Considerable experimental and theoretical work has been devoted

to understand the statistical properties of active turbulence and the motion of the associated topological defects or disclination lines [36–38].

More recently, it has been shown that topological defects are not merely a natural consequence of the nematic organisation of tissues, but that local stresses and flows generated by active defects can serve biological functions in a variety of living systems. Examples include defect-mediated cell death and extrusions in epithelial cell layers [30], formation of secondary layers at the positions of defects in bacterial colonies [39], and self-organization in Hydra [40] and myoblast tissues [41]. Topological defects are also associated with local changes in cell density in mesothelial cell layers. Since these layers serve as a barrier to cancer metastasis by preventing tumour cells to invade through them, defects can influence cancer cell clearance and spreading [42].

Physical mechanisms and topology thus offer important new perspectives on biological research. The aim of this work is to extend the understanding of the organisation of living matter in terms of the interplay between orientational structures and collective flows. This thesis consists of four main chapters, each exploring a different aspect of active nematics in the context of biological systems.

We first consider the behaviour of three-dimensional, active nematic droplets that are confined by a soft interface in chapter 3. We numerically investigate the effect of confinement on disclination line dynamics and how active flows can deform the confining interface. We show that the interplay between confinement and active flows inside droplets leads to an unprecedented range of complex droplet morphologies.

In chapter 4, we explore the effects of spatial variations of active stress on active nematic bulk systems in two and three dimensions. We find that activity gradients drive flows, that re-orient the nematic director field, acting as an effective anchoring force. At high activity, the system transitions into active turbulence. We show that activity gradients induce active torques on defects, which align two-dimensional $+1/2$ defects parallel to the gradient direction. In three-dimensional nematics, we find that disclination lines preferentially lie in the plane perpendicular to activity gradients due to active torques acting along the lines, where the average

orientation of the defect structure within the plane perpendicular to the line tangent depends on the defect type.

In chapter 5, we model biological systems in more detail by using continuum theories to study cell flows and cell alignment inside multicellular spheroids. Using analytical arguments and three-dimensional simulations, we show that the proliferation gradients in spheroids result in flows and gradients of activity, both of which can align the orientation axis of cells inside the aggregates. We identify three distinct alignment regimes and show that the continuum description of tissue dynamics inside spheroids can be used to infer dynamical cell parameters from experimentally measured cell orientation profiles.

In the last chapter 6, we relax the assumption that active forces must always point along the cell orientation axis. We investigate the relationship between cell orientations, flows, and the directions of cell-generated forces in confluent cell layers. We show that misalignment between cell orientations and active forces is linked to topological defects in the cell orientation field in two-dimensional tissues. We also report the emergence of domains in which the misalignment between cell orientations and active forces reaches 90°, effectively creating domains of extensile activity in a monolayer of contractile cells. This challenges the prevailing understanding that cells create either contractile or extensile forces and shows that the direction of active stress can vary continuously within tissues.

Thus, in this thesis, we show how physical continuum models of active materials can help us to understand the collective organisation of active entities in dense systems such as tissues. We show that collective cell motion in tissues is associated with active stress patterns and features in the orientation field, such as topological defects. This is a step towards the broader goal of understanding the role of physical theories in the life sciences.

2

A brief introduction to active nematics

In this chapter we present the theoretical framework on which the rest of this thesis is built. As discussed in the introduction, we investigate active fluids which consist of active constituents that are self-propelled or exert mechanical forces on their environment. We consider systems of microscopic particles which move collectively on length-scales significantly larger than the size of an individual particle. In this thesis we will focus on active nematic fluids, systems consisting of active anisotropic particles with hydrodynamical interactions.

Active nematics display chaotic flows in bulk due to the collective hydrodynamic forces particles generate by converting chemical energy from their surroundings into active stress. The goal is to investigate how active nematic theories can be used to describe the organisation and motion of cells inside living tissues. To describe tissue dynamics in vastly different biological systems, we must simplify all the incredibly complicated biochemical processes inside biological cells and define cell dynamics in terms of the most fundamental physical symmetries. This will allows us to model a large variety of biophysical systems using the same framework which describes systems in terms of a small number of order parameters: (i) A fluid velocity $\mathbf{u}$ describing the collective motion of particles on the macroscopic scale. (ii) A scalar phase-field φ describing the particle concentration in phase-separated systems. (iii) A second-rank, symmetric, traceless tensor $\mathbf{Q}$ describing

the orientational order of anisotropic particles that align along a certain axis, but with no preferred direction along that axis.

We start this chapter by introducing the equations of motion for the fluid flow $\mathbf{u}$ and phase-field φ in section 2.1. This framework, termed 'model H', is commonly used in soft matter physics to model the time evolution of a conserved order parameter which is coupled to an isotropic fluid. In the following section 2.2, we introduce nematic liquid crystals which consist of anisotropic particles. The magnitude and direction of orientational order can be described by a tensorial order parameter $\mathbf{Q}$. Based on nematic symmetries, we can construct a Landau-de Gennes free energy from the order parameter which, in the context of tissue dynamics, can be interpreted as tissue free energy arising from cell elasticity and cell-cell interactions. We then describe discontinuities in the orientation field, termed 'topological defects' in 2D and 'disclination lines' in 3D systems. Finally, we consider the ways in which anisotropic particles can be rotated by flows and present the Beris-Edwards equation, which couples the nematic order parameter $\mathbf{Q}$ to the vorticity and strain rate in the flow field $\mathbf{u}$. In the last section 2.3, we show that the generation of active forces by particles gives rise to an active stress term in the time evolution of the macroscopic flow field. We explain how active stress results in a hydrodynamic instability which creates chaotic flows and topological defects.

2.1 Phase-separation and multiphase flows in isotropic fluids

2.1.1 The Navier-Stokes equations

Most living matter systems are complex materials that are viscoelastic, combining both viscous (liquid-like) and an elastic (solid-like) properties. In this thesis we consider incompressible systems, such as dense cell aggregates [43–45], in which the build-up of macroscopic flows occur over time scales much larger than the viscoelastic relaxation time. Therefore, we can neglect the elasticity of systems and describe them in the liquid limit. The viscous response of many complex fluids can exhibit non-trivial rheological behaviour, where the viscosity depends on the

shear-rate [46, 47]. Since the rheological behaviour depends on the microscopic dynamics of the system, for simplicity, we assume that the flow field $\mathbf{u}$ follows the equations of motion of an incompressible, Newtonian fluid,

$$\nabla \cdot \mathbf{u} = 0 \,, \tag{2.1}$$

$$\rho \left(\partial_t + \mathbf{u} \cdot \nabla\right) \mathbf{u} = \nabla \cdot \mathbf{\Pi} \,, \tag{2.2}$$

where ρ is the density of the fluid and $\mathbf{\Pi}$ is the stress tensor which includes all hydrodynamic forces acting on the fluid. The continuity equation 2.1 and Navier-Stokes equation 2.2 are the conservation equations of mass and momentum, respectively. The stress tensor on the right-hand side of eqn. 2.2 has many different components, which we will explain in detail over the course of this chapter. For now, the stress tensor only consists of the viscous stress of a Newtonian fluid,

$$\mathbf{\Pi}^{visc} = 2\eta \mathbf{E} \,, \tag{2.3}$$

where η is the shear viscosity and $E_{ij} = (\partial_i u_j + \partial_j u_i)/2$ is the strain rate tensor.

2.1.2 The Cahn-Hillard equation

In phase-separated systems, distinct fluid phases can be described by a phase-field φ which can be interpreted as a concentration field which is locally conserved. Diffusive transport of a conserved order parameter follows Model-B dynamics, thus the time evolution of φ follows the Cahn-Hilliard convection-diffusion equation [48],

$$\left(\partial_t + \mathbf{u} \cdot \nabla\right) \varphi = \Gamma_\varphi \, \nabla^2 \mu \,, \tag{2.4}$$

where $\mathbf{u}$ is the velocity field and Γ_φ is the mobility which quantifies how fast φ responds to gradients in the chemical potential $\mu = \delta\mathcal{F}/\delta\varphi$. The mixing free energy $\mathcal{F} = \int f_{GL} dV$ can be expanded in powers of the order parameter and its gradients. Throughout most parts of this thesis, we choose the following Ginzburg-Landau free energy density:

$$f_{GL} = \frac{A_\varphi}{2} \varphi^2 \left(1 - \varphi\right)^2 + \frac{K_\varphi}{2} \left(\nabla\varphi\right)^2 \,, \tag{2.5}$$

where A_φ and K_φ are positive constants. The first term drives phase separation into two stable phases $\varphi = 1, 0$ and the second term penalises phase gradients. This description of binary fluids results in smooth concentration profiles between regions of different phases, where interfaces have a finite width $\ell \propto \sqrt{K_\varphi/A_\varphi}$ and introduce a surface tension $\gamma \propto \sqrt{K_\varphi}$ [48].

Gradients in the chemical potential μ not only set up diffusive currents of φ, but also give rise to an additional stress term in the Navier-Stokes equation 2.2, the capillary stress

$$\mathbf{\Pi}^{cap} = (f_{GL} - \mu\varphi)\mathbf{I} - \nabla\varphi \left(\frac{\partial f_{GL}}{\partial(\nabla\varphi)} \right) . \tag{2.6}$$

By taking the divergence of the capillary stress, we can obtain an intuitive expression for the force density acting on the fluid in terms of the chemical potential [49],

$$\nabla \cdot \mathbf{\Pi}^{cap} = -\varphi\nabla\mu \, . \tag{2.7}$$

The elastic properties of interfaces are thus solely determined by their free energy.

2.2 Adding anisotropy: Liquid crystals

Liquid crystals are a phase of matter that shares properties with both solids and fluids. While crystalline solids have long-range positional and orientational order, in fluids the positions and orientations of particles are disordered, with only short-range correlations. Liquid crystals sit between those two regimes, exhibiting solid-like properties such as long-range orientational order and elasticity, while having liquid-like characteristics such as fluidity and the inability to support shear (Fig. 2.1). Typically, molecular liquid crystals are composed of elongated, rod-shaped particles. Below a critical temperature or at high densities, these particles locally align with each other, thereby forming a nematic state with long-range orientational order [50]. The axis along which particles align is called the director field $\mathbf{n}$ (Fig. 2.1 b), which is one of the coarse-grained variables we will use throughout this thesis to describe anisotropic structures.

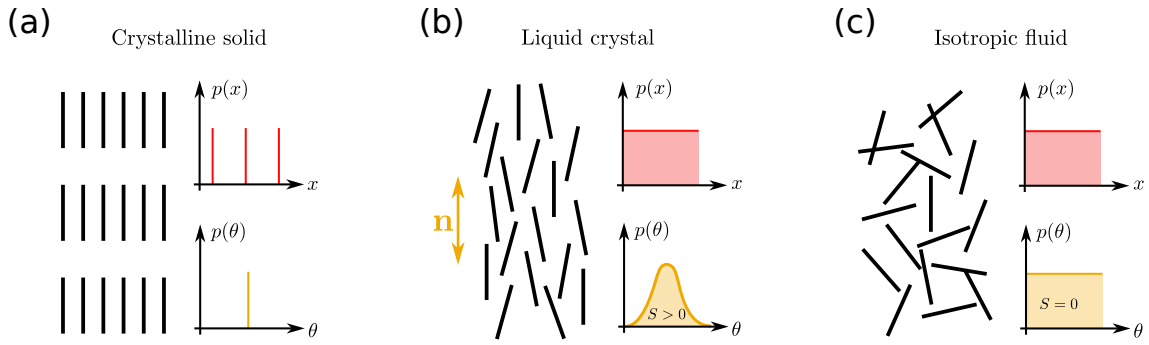


Figure 2.1: Schematic illustration of various possible phases of matter. **(a)** Crystalline solid with a periodic distribution of particle positions x and fixed particle orientations θ. **(b)** Nematic liquid crystal have a random distribution of particle positions, but particle orientations prefer to align along a common director axis $\mathbf{n}$. The magnitude of alignment S can be defined in terms of the distribution of particle orientations $p(\theta)$. **(c)** Isotropic liquids with a random distribution of particle positions and orientations show no long-range spatial or orientational order.

It should be noted that individual particles do not necessarily need to have a nematic symmetry in order to form a nematic phase. In fact, many tissues show nematic cell ordering although individual cells and their sub-cellular structures are highly polar (persistent cell migration, actin polymerization, polar microtubules). On the macroscale, nematic ordering of polar particles can arise if (i) interactions between particles have a nematic symmetry or (ii) polar particles switch direction much faster than the time scale of macroscopic dynamics. This is the case for many cells in dense tissues in the absence of mechanical or chemical gradients [51–53].

2.2.1 The nematic order parameter

To quantify the nematic phase it is helpful to construct an order parameter which describes the magnitude as well as the direction of local alignment. In a coarse-grained description, the local average orientation of anisotropic particles within a small volume is described by a head-less director field $\mathbf{n}$. The director field is not a standard vector field, since $\mathbf{n}$ and $-\mathbf{n}$ are indistinguishable under nematic symmetry. This head-tail symmetry means that the director angle θ is invariant under rotation $\theta = \theta + \pi$, unlike polar vectors which are invariant under $\theta_p = \theta_p + 2\pi$ [50].

If we denote all particle orientations within a small volume by unit vectors $\{\mathbf{b}^{(\alpha)}\}$, we can define the local magnitude of alignment S in terms of the distribution particle

orientations (Fig. 2.1 b). If we take the average alignment $\mathbf{n}$ to point along the z-axis, $\mathbf{b} = (\sin\theta\cos\phi, \sin\theta\sin\phi, \cos\theta)$ can be defined in terms of polar angles θ and ϕ. The average local alignment can be quantified by the probability distribution over particle orientations $f(\theta, \phi)d\Omega$. In this thesis we will focus on uniaxial nematics by assuming that the distribution function has cylindrical symmetry around $\mathbf{n}$, thus $f(\theta, \phi)$ is independent of the azimuthal angle ϕ. Systems without this symmetry are called biaxial nematics [50]. Additionally, the head-tail symmetry of the director field $\mathbf{n} = -\mathbf{n}$ must be reflected in the distribution function, thus $f(\theta) = f(\pi - \theta)$. The magnitude of alignment can then be characterised by the first non-zero term in the multipole expansion in θ, which is the quadrupole term

$$S = \frac{1}{2}\langle 3\cos^2\theta - 1\rangle = \int f(\theta)\left(\frac{3}{2}\cos^2\theta - \frac{1}{2}\right)d\Omega\,. \tag{2.8}$$

When particles are well aligned, $f(\theta)$ is sharply peaked around 0 or π and $S = 1$. On the other hand, if $f(\theta)$ is randomly distributed, $S = 0$.

Up to now, we have used two distinct coarse-grained order parameters S and $\mathbf{n}$ to quantify the magnitude and direction of orientational order, respectively. For convenience, we can also define a single tensorial order parameter $\mathbf{Q}$ which simultaneously describes the magnitude and direction of orientational order via a quadrupole expansion [50],

$$Q_{ij}(\mathbf{x}) = \frac{1}{N}\sum_{\alpha}\left(b_i^{(\alpha)}b_j^{(\alpha)} - \frac{1}{3}\delta_{ij}\right)\,, \tag{2.9}$$

where δ_{ij} is the Kronecker delta and the sum is over N particles in a small volume around $\mathbf{x}$. By definition, the tensorial order parameter is symmetric and traceless and therefore contains only five independent components. The $\mathbf{Q}$-tensor can be expressed in terms of the coarse-grained quantities $\mathbf{n}$ and S as

$$Q_{ij} = \frac{3S}{2}\left(n_i n_j - \delta_{ij}/3\right)\,. \tag{2.10}$$

A major advantage of this approach is that it allows us to simultaneously describe the time evolution of S and $\mathbf{n}$, and that $\mathbf{Q}$, by construction, automatically accounts for the head-tail symmetry of the director field.

2.2.2 The free energy of liquid crystals

The free energy of liquid crystals can be decomposed into two components, $f_{LC} = f_{bulk} + f_{dist}$. The first contribution f_{bulk} is called the bulk energy and describes how the energy of the system varies as a function of the magnitude of nematic order S. The second contribution is the distortion free energy f_{dist} which includes terms associated with distortions of the director field $\mathbf{n}$ and gradients in S. In the following, we will present how these energies can be constructed as a function of the nematic order parameter $\mathbf{Q}$.

Bulk free energy

As shown by Onsager [54], the isotropic-nematic transition can be understood in terms of the orientational and positional entropy of rod-like particles. If rods are oriented at an angle to each other, they have a large orientational entropy, but at the same time create a large excluded volume that is felt by other particles in their vicinity. On the other hand, if rods are oriented in the same direction, there is minimal excluded volume due to their anisotropy, so each rod has more space available which increases the positional entropy. Consequently, a loss in orientational entropy in the nematic phase is counterbalanced by an increased positional entropy. This results in the nematic state being a free energy minimum at high particle densities. The transition between isotropic and nematic states is a first-order phase transition which can be described by the Landau free energy [50]

$$f_{bulk} = a\, S^2 + b\, S^3 + c\, S^4 + \dots \,, \tag{2.11}$$

where the coefficients a, b, c are a function of the control parameters of the system. Since the only rotationally invariant functions of a traceless three-dimensional tensor are $\mathrm{Tr}(\mathbf{Q}^2)$ and $\mathrm{Tr}(\mathbf{Q}^3)$ [50], the bulk free energy can be also written as

$$f_{bulk} = \frac{\mathcal{A}}{2}\,\mathrm{Tr}(\mathbf{Q}^2) + \frac{\mathcal{B}}{3}\,\mathrm{Tr}(\mathbf{Q}^3) + \frac{\mathcal{C}}{4}\,\mathrm{Tr}(\mathbf{Q}^2)^2 \,, \tag{2.12}$$

where the expansion is taken to fourth-order to ensure thermodynamic stability and $\mathcal{A}, \mathcal{B}, \mathcal{C}$ are called the Landau-de Gennes coefficient. The values of $\mathcal{A}$, $\mathcal{B}$ and

$\mathcal{C}$ determine whether the system has an isotropic or nematic ground state. For stability reasons, to prevent unbounded growth of the scalar order parameter S, $\mathcal{C} > 0$ must be chosen to take a positive value. The isotropic-nematic transition in passive liquid crystals typically depends on the microscopic details of the system, like the interaction potential between particles, and external control parameters, such as the temperature T or particle concentration φ. Since biological systems operate at a constant temperature, in this thesis we focus on the transition as a function of particle concentration. This yields the Landau-de Gennes bulk energy as a function of particle concentration in terms of the nematic tensor $\mathbf{Q}$,

$$f_{bulk} = A_{LC}\left(\frac{1}{2}\left(1 - \frac{\bar{\eta}(\varphi)}{3}\right)\,\mathrm{Tr}(\mathbf{Q}^2) - \frac{\bar{\eta}(\varphi)}{3}\,\mathrm{Tr}(\mathbf{Q}^3) + \frac{\bar{\eta}(\varphi)}{4}\,\mathrm{Tr}(\mathbf{Q}^2)^2\right), \quad (2.13)$$

where A_{LC} sets the bulk energy scale and the function $\bar{\eta}(\varphi)$ quantifies the dependence of bulk energy on the particle concentration φ. Eqn. 2.13 predicts a first-order phase transition between a nematic ($\bar{\eta} > \eta_c$) and an isotropic ($\bar{\eta} < \eta_c$) phase at the critical value $\eta_c = 2.7$.

It should be noted that the dimension of the $\mathbf{Q}$-tensor affects the expression for the bulk free energy, since the term $\mathrm{Tr}(\mathbf{Q}^3)$ is only allowed in three dimensions. In two dimensional systems, this term disappears due to symmetry, and the isotropic-nematic transition becomes continuous [55].

Distortion free energy

The equilibrium state of a nematic liquid crystal is one of uniform alignment, thus distortions in the director field $\mathbf{n}$ are penalised through an elastic free energy. In three dimensional nematics there are three distinct types of deformations: bend, splay and twist (Fig. 2.2). The elastic energies associated with each distortion can be written in terms of the director field $\mathbf{n}$ [56],

$$f_{Frank} = \frac{K_1}{2}[\nabla \cdot \mathbf{n}]^2 + \frac{K_2}{2}[\mathbf{n} \cdot (\nabla \times \mathbf{n})]^2 + \frac{K_3}{2}[\mathbf{n} \times (\nabla \times \mathbf{n})]^2\,, \quad (2.14)$$

where K_1, K_2 and K_3 are the splay, twist and bend Frank elastic constants, respectively. For simplicity, in this thesis we assume that the elastic constants

are equal, $K_1 = K_2 = K_3 = K$. This commonly used one-elastic-constant approximation has been shown to accurately describe many biophysical systems in 2D and 3D [30, 34, 37, 57–59].

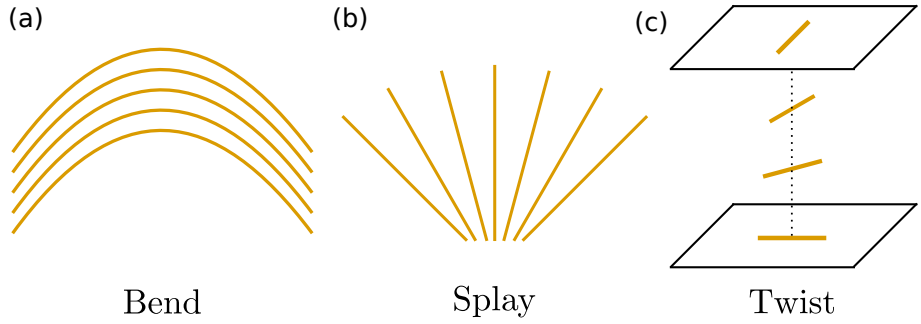


Figure 2.2: There are three distinct types of distortions in 3D nematics. **(a)** Bend. **(b)** Splay. **(c)** Twist.

We can also write down a free energy penalizing distortions in terms of the tensorial order parameter by expanding the distortion free energy in derivatives of $\mathbf{Q}$. In the one-elastic-constant approximation, this yields the simple expression

$$f_{dist} = \frac{K_{LC}}{2} (\nabla \mathbf{Q})^2 \ , \tag{2.15}$$

where the elastic constant K_{LC} in the tensor representation is related to the Frank elastic constant through the relation $K_{LC} = (2/9S)K$.

The total free energy of liquid crystals $f_{LC} = f_{bulk} + f_{dist}$ gives rise to an hydrodynamic elastic stress,

$$\mathbf{\Pi}^{el} = \mathbf{QH} - \mathbf{HQ} - \nabla \mathbf{Q} \left(\frac{\partial f_{LC}}{\partial (\nabla \mathbf{Q})} \right) - \xi [\mathbf{H}\tilde{\mathbf{Q}} + \tilde{\mathbf{Q}}\mathbf{H} - 2\tilde{\mathbf{Q}} \, \mathrm{Tr}(\mathbf{QH})] \, , \tag{2.16}$$

where $\tilde{\mathbf{Q}} = \left(\mathbf{Q} + \frac{1}{3}\mathbf{I} \right)$. ξ and $\mathbf{H}$ are the flow-alignment parameter and the molecular field, respectively, which we will introduce in section 2.2.4.

The free energy of tissues

Eukaryotic cells in confluent tissues generate active junctional forces between themselves, which can distort their shape. The average aspect ratio ω_0 of cells therefore not only depends on the equilibrium geometry of a certain cell type, but also on the force balance between junctional forces and cell elasticity [18, 60].

Tissues consisting of fairly isotropic cells ($\omega_0 \approx 1$) typically do not exhibit long-range orientational order ($S = 0$), since cells do not have a strong polarization. On the other hand, highly anisotropic cells ($\omega_0 > 1$) usually form macroscopic domains in which cell orientations are well aligned ($S > 0$) [30, 31, 61–63]. Long-range nematic order has also been observed in monolayers of elongated bacterial cells [29, 64]. These observations suggest that nematic order on the tissue scale S is correlated with the the aspect ratio of cells ω_0, however, the details of this coupling are still being investigated [5]. While it is theoretically possible for elongated cells to form isotropic tissues, for the purposes of this thesis, we will disregard this possibility and instead assume, that the nematic order of tissues is directly linked to the cell shape (Fig. 2.3 a).

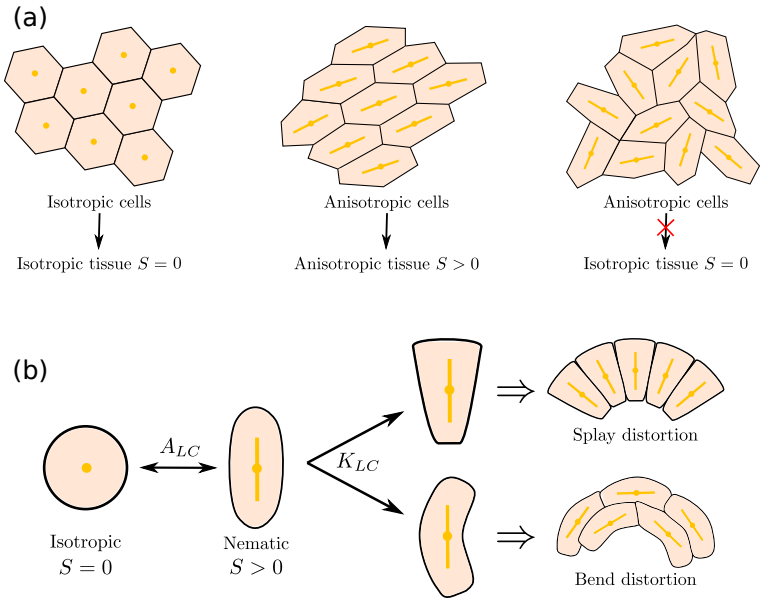


Figure 2.3: **(a)** Nematic order S in tissues is typically coupled to aspect ratio ω of cell shape. For the purposes of this thesis we assume $S = \omega - 1$, implying that anisotropic cells always form nematic tissues. **(b)** The mechanical properties of cells give rise to a free energy where distinct cell shape deformations are associated with different elastic constants: A_{LC} penalises cell stretching, which changes the aspect ratio of cells. K_{LC} penalises cell bending, which results in distortions of the nematic director field.

The Landau-de Gennes bulk energy eqn. 2.13 was originally derived to describe the first-order isotropic-nematic transition in systems of rod-like molecules at thermodynamic equilibrium. Clearly, those assumptions only hold for equilibrium systems and cannot be directly applied to living cells, which are far from equilibrium

and where active noise dominates thermal fluctuations. However, we note that deep in the isotropic or nematic phase, eqn. 2.13 gives rise to a harmonic potential in S around an equilibrium value S_0, $f_{bulk} \propto A_{LC}(S - S_0)^2$. Assuming that cell shape deformations are associated with a quadratic elastic energy, $f_{def} \propto (\omega - \omega_0)^2$, the liquid crystal bulk energy f_{bulk} can be identified as the cell deformation energy f_{def} using the relation $\omega = S + 1$. The bulk constant A_{LC} therefore quantifies the elastic energy associated with cell deformations which change the aspect ratio ω_0. On the other hand, since cells must physically deform when the nematic order in tissues is distorted, the elastic constant K_{LC} quantifies the elastic energy associated with bending, splaying or twisting cells (Fig. 2.3 b). The liquid crystal free energy f_{LC} therefore can be used as a proxy to encode mechanical cell properties. It should be noted, however, that 3D cell shapes do not need to be rotationally symmetric, which implies that $\mathbf{Q}$ could have a biaxial component. This would modify the ways in which cells mechanically interact which each other, thus adding additional terms to the elastic energy.

2.2.3 Discontinuities in the director field

The coarse-grained director field $\mathbf{n}$ described the direction of orientational order and usually varies smoothly across systems due to the elastic energy penalising strong distortions. However, points at which domains of different orientations meet, orientational order is frustrated and the director cannot be properly defined. These singularities are called topological defects, because they cannot be resolved through a smooth reorientation of the director field.

2D systems

In two-dimensional systems, topological defects are singular points, which can be characterised by a topological charge. The charge measures how many times the director winds along a contour taken around the defect core. The topological charge of a defect is defined as

$$m = \frac{1}{2\pi} \oint d\theta \,, \tag{2.17}$$

where the line integral is taken around the defect core and θ is the director angle of a 2D director field $\mathbf{n} = [\cos\theta, \sin\theta]$. Since the total topological charge of a system is conserved, the only way defects can be added or removed is by creation or annihilation in pairs of opposite charge.

The orientation of the director field around topological defects of charge m can be found by minimising the distortion free energy eqn. 2.14 using the one-elastic-constant approximation. This yields $\theta = \theta_0 + m\phi$, where ϕ is the polar angle around the defect core and θ_0 is an arbitrary offset. Because the director field has nematic symmetry, $\theta \to \theta + \pi$, the topological charge m can take any half-integer value. However, since the distortion energy around defects scales as $f_{dist} \propto Km^2$, defects of charge $m = \pm 1/2$ are energetically favoured over defects of higher charge, which makes them the dominant singularities in 2D nematics (Fig. 2.4 a).

3D systems

Discontinuities in a three-dimensional director field form disclination lines, which either form closed loops or terminate at the boundary of systems. If the director field in the plane perpendicular to a disclination line segment has no out-of-plane component, it is called a wedge-type disclination and resembles a $\pm 1/2$ defect in 2D systems. However, in 3D the director field can also rotate out of the plane while moving around the disclination core, thereby creating a twist disclination which is inherently three-dimensional (Fig. 2.4 b). When moving around the core of a disclination in the plane perpendicular to its line tangent, the director $\mathbf{n}$ winds around a given rotation vector $\mathbf{\Omega}$ by an angle π.

Disclination lines can be classified in terms of the *twist angle* $\beta \in [0, \pi]$, which is the angle between the rotation vector $\mathbf{\Omega}$ and the local line tangent $\mathbf{t}$ (Fig. 2.4 c). Wedge-type disclinations correspond to $\beta \approx 0, \pi$ and pure twist defects are indicated by $\beta \approx \pi/2$. However, it should be emphasised that β can take any value between 0 and π and varies continuously along disclination lines.

Unlike in 2D systems, where $\pm 1/2$ defects can only nucleate or annihilate in pairs of opposite charge, the director configuration around a disclination line

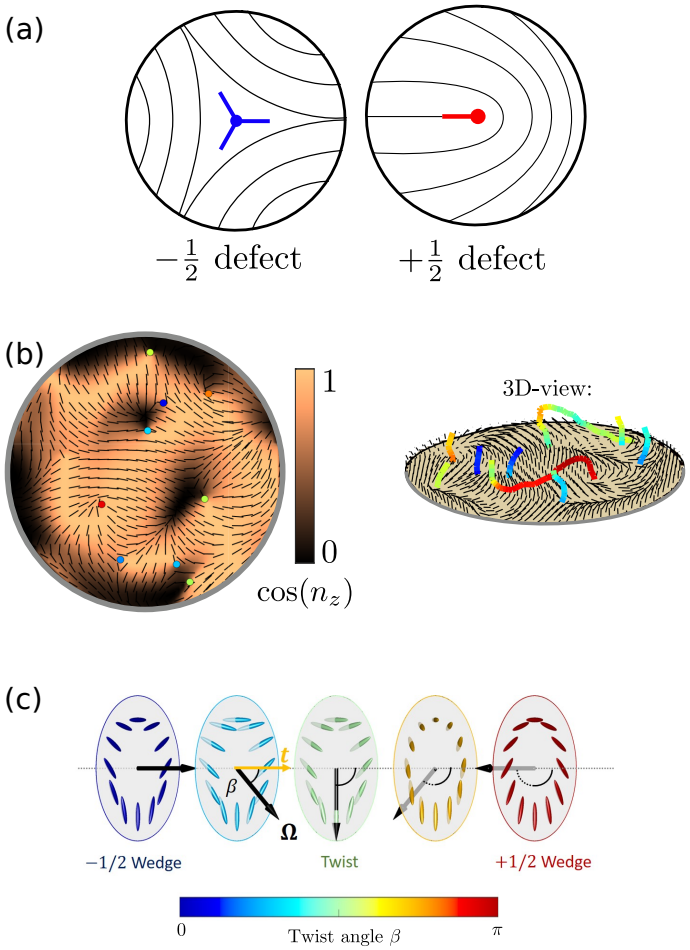


Figure 2.4: **(a)** $\pm 1/2$ defects are the dominant singularities in 2D systems. Comet-shaped $+1/2$ defects have a unique orientation axis (red line) while $-1/2$ defects show a three-fold symmetry (blue lines). **(b)** Two-dimensional cross-sections of a 3D director field. Discontinuities in a three-dimensional director field can be classified as wedge-type or twist-type. If the director field in the plane perpendicular to a disclination line has no out-of-plane component, $n_z = 0$, it is called a wedge-type disclination which resembles a $\pm 1/2$ defect in 2D systems. If the out-of-plane component n_z significantly varies around a disclination it is called a twist-type. The disclination type can continuously vary along disclination lines. **(c)** Disclination lines can continuously transform from a local $-1/2$ configuration (in the plane perpendicular to the line) into a $+1/2$ configuration through an intermediate twist defect. Disclination lines can be locally classified by the *twist-angle* β, which is the angle between the local line tangent $\mathbf{t}$ (yellow arrow) and the axis $\mathbf{\Omega}$ around which the director field winds. Twist disclinations correspond to $\beta \approx \pi/2$ and $-1/2$ and $+1/2$ wedge disclinations to $\beta \approx 0$ and $\beta \approx \pi$, respectively.

segment in 3D is not topologically protected. A disclination line can continuously transform from a local $-1/2$ configuration in the plane perpendicular to the line tangent into a $+1/2$ configuration through an intermediate twist defect. Closed disclination loops, however, can be characterized by a total topological charge which can take full integer values [38, 65].

2.2.4 Nematohydrodynamics

The Beris-Edwards equation

In section 2.2.1 we introduced the coarse-grained tensorial order parameter $\mathbf{Q}$ which describes the magnitude S and direction $\mathbf{n}$ of rotational order. Unlike the phase-field φ, the local nematic order is not a conserved quantity so its time evolution follows Model A dynamics [66]. Since cells adhere to each other, cells not only get advected by flow but their orientation also responds to the cellular flows around them. This gives rise to additional terms in the evolution equation of $\mathbf{Q}$, which is often termed the Beris-Edwards equation [66],

$$D_t\mathbf{Q} - \mathcal{W} = \Gamma\mathbf{H}\,, \tag{2.18}$$

where $D_t = (\partial_t + \mathbf{u}\cdot\nabla)$ is the material derivative. The rotational diffusivity Γ on the right-hand side controls the relaxation of $\mathbf{Q}$ towards the minimum of the free energy $\mathcal{F}$ through the molecular field

$$\mathbf{H} = -\left(\frac{\delta\mathcal{F}}{\delta\mathbf{Q}} - \frac{\mathbf{I}}{3}\mathrm{Tr}\left(\frac{\delta\mathcal{F}}{\delta\mathbf{Q}}\right)\right)\,. \tag{2.19}$$

This definition ensures that the time evolution of $\mathbf{Q}$ keeps the tensor symmetric and traceless. The tensor $\mathcal{W}$ is called the co-rotational term and quantifies the ways cell orientation changes in response to gradients in the flow field $\mathbf{u}$ [66–68],

$$\mathcal{W}_{ij} = (\xi E_{ik} + \Omega_{ik})\,\tilde{Q}_{kj} + \tilde{Q}_{ik}\,(\xi E_{kj} - \Omega_{kj}) - 2\xi\tilde{Q}_{ij}Q_{kl}W_{lk}\,, \tag{2.20}$$

where $E_{ij} = (\partial_j u_i + \partial_i u_j)/2$ is the strain rate tensor, $\Omega_{ij} = (\partial_j u_i - \partial_i u_j)/2$ is the vorticity tensor, $W_{ij} = \partial_i u_j$ is the velocity gradient tensor and $\tilde{Q}_{ij} = (Q_{ij} + \delta_{ij}/3)$. The coupling of particle orientations to flows includes two contributions: flow

rotation and shear alignment (Fig. 2.5). The flow-alignment parameter ξ quantifies the coupling strength to shear-flows, where the sign of ξ determines whether particles align along the extensional or compressive flow axis of a pure shear flows.

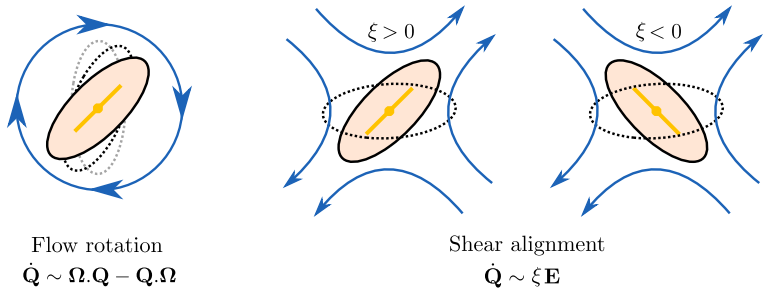


Figure 2.5: The ways cells rotate in flows has two contributions: solid body rotation driven by vorticity $\mathbf{\Omega}$ and orientational alignment along the flow axes of a pure shear flow described by the strain rate $\mathbf{E}$. The shear-alignment behaviour of cells depends on the flow-alignment parameter ξ, which is a fixed tissue parameter.

For systems in which the magnitude of order S does not vary significant, it is sometimes more convenient to define the time evolution equations in terms of the director field $\mathbf{n}$. Deep in the nematic state, $S = S_0$, the Beris-Edwards equation 2.18 can be mapped into the Ericksen-Leslie equation for the director field [66, 67]. In two dimensional systems, where $\mathbf{n} = [\cos\theta, \sin\theta]$, the evolution equation for the director angle is [69–71]

$$D_t\theta = \omega + \lambda\left[\cos(2\theta)E_{xy} - \sin(2\theta)E_{xx}\right] - \Gamma\frac{\delta\mathcal{F}}{\delta\theta}\,, \tag{2.21}$$

where $\omega = \partial_x u_y - \partial_y u_x$ is the vorticity of flow field $\mathbf{u} = [u_x, u_y]$ and E_{ij} is the strain rate tensor. The flow-alignment parameter λ in the Ericksen-Leslie model is related to ξ in the Beris-Edwards model by $\lambda = \frac{3S_0+4}{9S_0}\xi$.

The flow-alignment parameter in tissues

In passive liquid crystals, the flow-alignment parameter is a coarse-grained model parameter emerging from internal friction and torques between the constituents. The value of λ can be related to the geometry and aspect ratio of particles, where the orientational dynamics of rigid particles in dilute systems follows $\lambda > 0$ for rod-shaped particles and $\lambda < 0$ for oblate-shaped particles [71, 72]. Living cells,

however, can react to forces in their environment that allow them to actively align in a given direction as a response to shear flows [73, 74]. This renders it challenging to derive the expressions for λ in living tissues.

Different formalisms have been developed to geometrically decompose large-scale tissue shear into cellular contributions, which include cell shape changes and topological changes in the cellular network. In the absence of topological changes induced by cell divisions, cell deaths or T1 transitions, it was predicted that cell shape dynamics follows $\lambda = +1$ [75]. Studies of cellular flows in the wing epithelium of Drosophila have revealed that topological T1 transitions greatly contribute to macroscopic tissue shear [76], raising the question whether $\lambda = 1$ is a reasonable approximation.

There are only few studies that have attempted to directly measure the flow-alignment parameter in living tissues. The analysis of cell orientations and flows in confluent layers of spindle-shaped cells under confinement indicated that tissue dynamics in this particular system follows $\lambda > 0$ [63]. Nevertheless, since the flow-alignment of most cell types is still unknown and may depend on biochemical signals or mechanical properties of the environment, in this thesis we assume that λ is an intrinsic tissue property of arbitrary value.

2.3 Adding activity: Active nematics

In this section, we introduce the concept of active hydrodynamic stress. We start by considering anisotropic, apolar cells, which exert dipolar forces on their environment. By coarse-graining active forces, we derive an expression for the active hydrodynamic stress in tissues. Subsequently we show that active stress creates a hydrodynamic instability, resulting in a dynamical steady-state termed active turbulence which is characterised by chaotic flows and motile topological defects (2D) or disclination lines (3D). This will provide us with the necessary framework to study flows and defect dynamics inside tissues.

2.3.1 The origin of active stress

Microscopic particles, such as biological cells or microswimmers, operate at very small Reynolds number where flow is dominated by viscous forces rather than inertia. In this Stokes limit, the motion of an individual particles is governed by the flow which is generated by the sum of all the active forces around it. We can therefore derive an active stress tensor Π^{act} for the flow field $\mathbf{u}$ by coarse-graining over active, dipolar forces generated by individual particles.

Because cells are on average apolar on the time scale of tissue flows, to first order, we can approximate the forces they exert along their interface on their environment by a dipolar force along the cell orientation axis. This is described by two equal and opposite forces F_ζ directed along the cell orientation $\mathbf{b}$ at a distance a from the cell's centre of mass (Fig. 2.6). A collection of cells with centre of mass positions $\mathbf{x}^{(\alpha)}$ and orientations $\mathbf{b}^{(\alpha)}$ yield the following force density:

$$\nabla \cdot \mathbf{\Pi}^{act}(\mathbf{x}) = \mathbf{F}^{act(\mathbf{x})} = F_\zeta \sum_\alpha \mathbf{b}^{(\alpha)} \left[\delta(\mathbf{x} - \mathbf{x}^{(\alpha)} + a\mathbf{b}^{(\alpha)}) - \delta(\mathbf{x} - \mathbf{x}^{(\alpha)} - a\mathbf{b}^{(\alpha)})\right] . \tag{2.22}$$

If we expand the delta functions around the centre of mass positions $\mathbf{x}^{(\alpha)}$, we can approximate the active force density eqn. 2.22 by [77]

$$\mathbf{F}^{act}(\mathbf{x}) \approx F_\zeta a \nabla \sum_\alpha \mathbf{b}^{(\alpha)}\mathbf{b}^{(\alpha)}\delta(\mathbf{x} - \mathbf{x}^{(\alpha)} + \mathcal{O}(\nabla^2) . \tag{2.23}$$

The active force density can be rewritten as an active stress in terms of coarse-grained quantities,

$$\mathbf{\Pi}^{act}_{ij}(\mathbf{x}) = -c(\mathbf{x})F_\zeta a \left(n_i n_j - \delta_{ij}/3\right) + \mathcal{O}(\nabla) . \tag{2.24}$$

where $c(\mathbf{x})$ quantifies the local number density and nematic order of cells. If we assume the cell density is constant across systems and use eqn. 2.9 to identify the $\mathbf{Q}$-tensor, we arrive at

$$\mathbf{\Pi}^{act} = -\zeta\mathbf{Q} , \tag{2.25}$$

where we have condensed all prefactors into a single activity constant ζ, which controls the magnitude of active stress. The sign of ζ describes different types

of activity: $\zeta > 0$ corresponds to extensile force dipoles which push outwards along their long axis, while $\zeta < 0$ corresponds to contractile dipoles where the force direction is reversed. It should be noted that the active stress cannot be derived from a free energy, thus this term violates detailed balance and drives the system out of equilibrium.

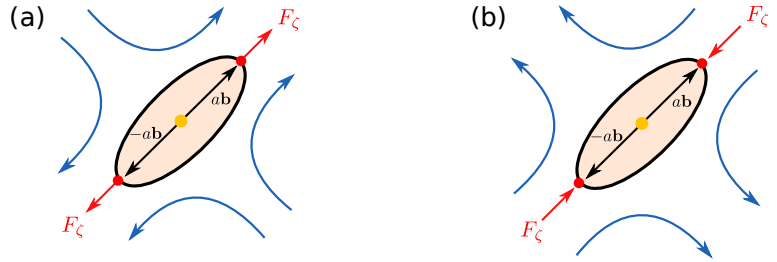


Figure 2.6: The active force cells exert on their environment can be approximated to leading order as **(a)** extensile or **(b)** contractile force dipoles. The blue lines indicate cell flows generated by these forces.

Now we finally have all the terms we need to define the stress tensor of active nematics,

$$\mathbf{\Pi} = \mathbf{\Pi}^{visc} + \mathbf{\Pi}^{cap} + \mathbf{\Pi}^{el} + \mathbf{\Pi}^{act} \tag{2.26}$$

where $\mathbf{\Pi}^{visc}$ (eqn. 2.3), $\mathbf{\Pi}^{cap}$ (eqn. 2.6), $\mathbf{\Pi}^{el}$ (eqn. 2.16), $\mathbf{\Pi}^{act}$ (eqn. 2.25) are the viscous, capillary, elastic and active stress, respectively.

2.3.2 Active turbulence

We now argue that the ground-state of liquid crystals is unstable in the presence of active stress, eqn. 2.25, where a hydrodynamic instability destroys long-range nematic order and leads to the nucleation of defects.

Hydrodynamic instabilities

From eqn. (2.25) it is apparent that active forces are induced by either gradients in ζ or distortions in $\mathbf{Q}$. It has been shown that small distortions in nematic order can set up active flows, which further amplify the distortion via the co-rotation term in the Beris-Edwards equation 2.18, thereby further increasing the magnitude of active forces. This is a well-known hydrodynamic instability [77],

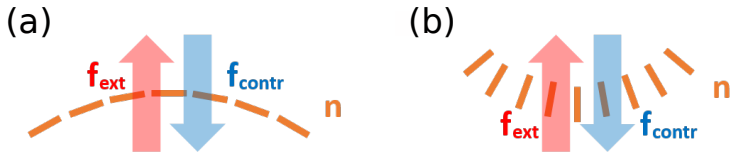


Figure 2.7: **(a)** Bend and **(b)** splay perturbations of the director field **n** set up active flows which further enhance or stabilise the respective perturbation. Forces in extensile or contractile systems are shown by red or blue arrows, respectively. It is apparent that extensile (contractile) systems are unstable to bend (splay) deformations.

where bend/splay distortions are unstable in extensile/contractile bulk systems, respectively (Fig. 2.7). The bend/splay deformations eventually grow and begin to form wall-like regions of high director distortion [78]. The distortion pattern emerges at a characteristic *active length-scale* $\ell_\zeta = \sqrt{K_{LC}/\zeta}$, which can be derived by considering the balance between active flows and passive restoring forces due to the elastic energy of nematic distortions [79].

Defect nucleation

As the hydrodynamic instability grows, walls of strong bend or splay distortions eventually become nucleation sites for $\pm 1/2$ defects in 2D systems [80] or disclination loops in 3D systems [37, 38]. Since active stress renders the quiescent ground state unstable, the system is constantly pushed out of equilibrium and defects do not annihilate immediately. This leads to a steady-state termed active turbulence [80], which is associated chaotic flow patterns and a finite number of topological defects. The spatial and temporal variations of flows in active turbulence can be characterized by the active length-scale $\ell_\zeta = \sqrt{K_{LC}/\zeta}$ and time-scale $\tau_a = \eta/\zeta$, where η is the viscosity of the fluid and K_{LC} is the elastic constant of the liquid crystal.

Two-dimensional active turbulence is characterised $\pm 1/2$ defects which are continually created and destroyed. In three-dimensional systems, on the other hand, disclination lines undergo complicated transformation events such as breakup, recombination, nucleation and annihilation [38]. Disclination lines typically form closed, charge-neutral loops in bulk systems [37] or, in the presence of a confining interface, can terminate at the boundary.

Self-propelled defects

In 2D systems, distortions of the director field around $\pm 1/2$ defects create active forces which drive strong flows around the core of defects (Fig. 2.8). The symmetry of $+1/2$ defects creates a directional flows which make them self-propel along the tail-to-head direction in extensile systems and in the opposite direction in contractile systems. $-1/2$ defects, on the other hand, have no self-propulsion since the active forces around them balance.

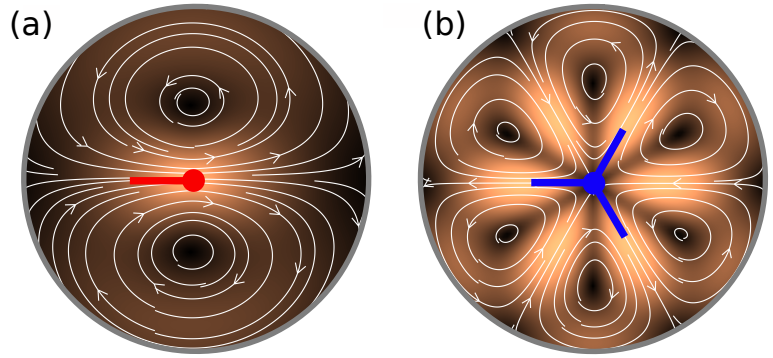


Figure 2.8: (a) Active stress around $+1/2$ defects drives directional flows which makes them self-propel along the tail-to-head direction in extensile systems. **(b)** The active flow around $-1/2$ defects has a three-fold symmetry and thus does not generate self-propulsion. Flow fields are shown for extensile activity - the flow direction reverses in contractile systems. Flow lines are shown in white, where the background colour indicates the magnitude of flows.

In 3D systems, disclination lines act as self-propelled entities moving through the fluid. Based on a simplified model neglecting elastic interactions, each disclination line segment can be associated with a local self-propulsion velocity which depends on the local director profile [36]. The self-propulsion velocity $v_\perp^{SP}$ perpendicular to the local line tangent depends on the twist angle β,

$$v_\perp^{SP} \propto (1 - \cos\beta)^2 \,. \tag{2.27}$$

Thus, unlike in two-dimensional active turbulence where the dynamics is dominated by two species of quasi-particles ($\pm 1/2$ defects), disclination lines act as quasi-particles with an intrinsic degree of freedom, the twist angle $0 \leq \beta \leq \pi$. Line segments with $\beta = 0$ are passive while $\beta = \pi$ line segments have the strongest self-propulsion.

2.4 Conclusion

In this chapter, we have introduced the theoretical framework necessary to understand active nematics. We have introduced a phase-field φ to describe phase-separation in fluids and a coarse-grained order parameter $\mathbf{Q}$ describing the orientation of anisotropic particles. We have summarised the basic properties of topological defects in 2D and disinclination lines in 3D. We have presented the continuum equations of motion for the fluid velocity $\mathbf{u}$ (eqns. 2.2, 2.1), the phase-field φ (eqn. 2.4) and the nematic order parameter $\mathbf{Q}$ (eqn. 2.18).

Finally, we derived an expression for the coarse-grained active stress which arises from active force generation on the micro-scale. This active stress causes a hydrodynamic instability, which results in a dynamical steady-state termed active turbulence. This state is characterised by chaotic flows and motile topological defects (2D) or disclination lines (3D). The concept of active turbulence and self-propelling defects will accompany us throughout this thesis.

3

Active matter under soft confinement

In this chapter we explore the behaviour of three-dimensional active nematic fluids which are confined by a soft interface. We numerically investigate how disclination line dynamics and active flows are affected by three-dimensional confinement and, on the other hand, how activity-driven flows can drive deformations of the confining interface. Although our model only incorporates the simplest possible form of achiral active stress, active nematic droplets display an unprecedented range of complex morphologies. We explain this diversity of behaviours in terms of an interplay between active anchoring, active flows and the dynamics of the motile disclination lines. We discuss our findings in the light of biological processes such as morphogenesis, collective cancer invasion and the shape control of biomembranes, suggesting that some biological systems may share the same underlying mechanisms as active nematic droplets.

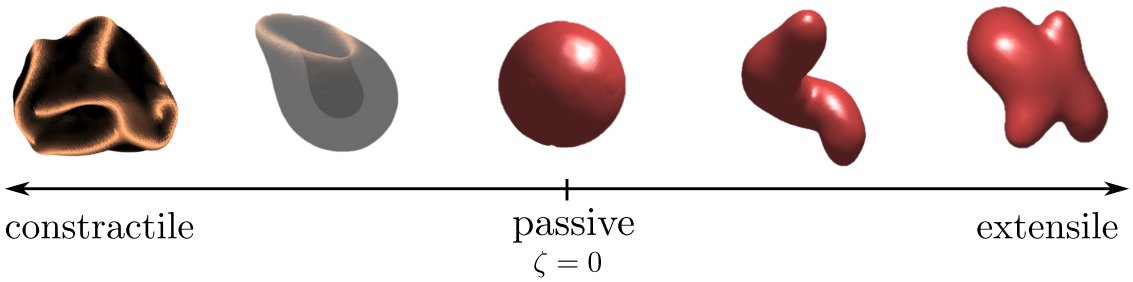


Figure 3.1: Illustration of different droplet morphologies. In this chapter we will explore the ways extensile and contractile active stress drive flows which deform the interface of three-dimensional active droplets.

3.1 Introduction

Considerable experimental and theoretical work has been devoted to understanding the properties of active turbulence, and the motion of associated topological defects. Recently it has proved possible to design active materials that allow imaging of three-dimensional active nematics and, in particular, the associated motile disclination loops and lines [37]. This was achieved by dispersing force-generating microtubule bundles in a passive colloidal liquid crystal based on filamentous viruses. Numerical simulations of three dimensional (3D) bulk systems such as this have revealed that flows and the morphological dynamics of disclination lines are governed by the local director profile surrounding the disclination line and that defect loops in extensile systems are generally formed via the well-known bend instability [36].

3D active turbulence and disclination line dynamics has also been investigated for spherical confinement using numerical modelling in both achiral [38] and chiral systems [81, 82]. Enforcing strong in-plane surface alignment allowed the formation of 2D defects on the surface and was used to highlight the coupling of surface and bulk topological defect dynamics. In all of those studies, however, the active nematic was confined to a fixed geometry which did not allow the investigation of activity-induced shape changes of the boundary. A potential way to study these systems experimentally would be to confine 3D active nematics by using synthetic vesicles or biomembranes, similarly to what has been done for quasi-2D nematic films [25].

The theory of active nematics is not only able to describe the dynamics of active materials, but is also increasingly being used to model biological matter, with examples including biofilm initiation [29], topological defects in cell monolayers [30, 32, 33] and epithelial expansion [83]. This suggests that the study of 3D active matter may be of relevance to the collective motion of groups of cells inside cell aggregates during embryonic development or to the growth and spread of tumours. In vivo, both of these processes typically happen in crowded environments where cells compete for space. The tissue or extracellular matrix which surrounds cell aggregates therefore effectively acts as a soft confinement.

Therefore, to underpin extension of active nematic theories to describe 3D living matter, we investigate self-deforming active nematic droplets in three dimensions, describing the interplay between disclination dynamics and droplet morphology. We find that extensile droplets form finger-like protrusions at points where disclination lines reach the surface. In contractile droplets, however, disclinations lead to a wrinkled drop surface. Moreover for small, contractile droplets, we find that invagination, to form a cup-like configuration, can be driven by nematic activity alone. We present evidence explaining the reasons behind the different behaviours stressing, in particular, the role of active anchoring, an effective surface alignment resulting from active flows.

We start by introducing the simulation method used to model active droplets confined by a membrane and how simulation parameters can be mapped to experimental values in section 3.2. This is followed by presenting the main results which are divided into three sections: First we investigate the nematic structure on the surface of an active droplet (section 3.3) and how this affects the dynamics of disclination lines in the bulk of spherical droplets (section 3.4). We then move on to show how active forces can deform the interface by highlighting mechanisms causing droplet deformations triggered by both extensile and contractile activity in section 3.4. The last section 3.5 summarises the key results and points out possible connections to biological systems.

3.2 Simulation method

We use a continuous phase-field φ to describe the position of the confining interface which separates the inside of active nematic droplets ($\varphi = +1$) from the surrounding passive, isotropic environment ($\varphi = -1$). The liquid crystal bulk free energy eqn. 2.13 is used to couple the nematic $\mathbf{Q}$-tensor to the phase-field φ. We define $\bar{\eta}(\varphi) := \eta_c + \eta_1\varphi$, and choose a value of $\bar{\eta}_1$ that ensures that the system forms a nematic droplet ($\varphi = +1$) which is surrounded by isotropic fluid ($\varphi = -1$). Alternative expressions for $\bar{\eta}(\varphi)$ or the liquid crystal bulk energy have been used in other work [84, 85] resulting in qualitatively the same dynamics, as long as the droplet is in the nematic phase ($\bar{\eta}(\varphi = 1) > \eta_c$) and the surroundings are isotropic ($\bar{\eta}(\varphi = -1) < \eta_c$).

We solve the equations of motion for the phase-field φ, the nematic tensor $\mathbf{Q}$ and the velocity field $\mathbf{u}$ using a hybrid lattice Boltzmann-finite difference method which is outlined in the appendix A. This involves solving the Beris-Edwards equation 2.18 for the nematic order parameter $\mathbf{Q}$ where we use the free energy $f_{LC} = f_{bulk} + f_{dist}$ presented in section 2.2.2. The time evolution of the phase-field φ is obtained by solving the Cahn-Hillard equation 2.4 using a specific membrane free energy f_{mem}, which we will introduce in the next section. Finally, we obtain the velocity field $\mathbf{u}$ by solving eqns. 2.1, 2.2 with the stress tensor $\mathbf{\Pi} = \mathbf{\Pi}^{visc} + \mathbf{\Pi}^{el} + \mathbf{\Pi}^{act}$ consisting of both passive and active contributions. The numerical detection of disclination lines is outlined in appendix B.

Simulations were performed on a three-dimensional lattice of size $100 \times 100 \times 100$ and discrete space and time steps were chosen as unity. We used periodic boundary conditions for the simulation box and the system initially consisted of a spherical, nematic drop of radius $R = 30$ ($\varphi = +1$) embedded in an isotropic fluid ($\varphi = -1$), unless otherwise stated. Initially we let the system relax for $t = 500$ time-steps such that the droplet interface and the nematic tensor $\mathbf{Q}$ reached their equilibrium profile before we switched on activity. Throughout this chapter, we used the following parameter set for all simulations: fluid density $\rho = 1$, shear viscosity $\eta = 2/3$, $\Gamma_{LC} = 0.1$, $\Gamma_\varphi = 0.2$, $\kappa^* = 0.1$, $\epsilon = 1.4$, $A_\varphi = 0.1$, $\eta_1 = 0.3$ and

$\xi = 0.1$ in lattice-Boltzmann units. For spherical droplets in sections 3.3 and 3.4, we used $K_{LC} = 0.1$, $K_\varphi = 0.4$, $A_{LC} = 0.75$ and $|\zeta| = 0.01$. For soft droplets in section 3.5, we used the following parameters, unless otherwise stated: $K_{LC} = 0.2$, $K_\varphi = 0.2$, $A_{LC} = 1.5$,and $|\zeta| = 0.02$.

3.2.1 Membrane free energy

We assume that the active nematic droplets is confined by a rigid membrane, which is described by the following free energy:

$$\mathcal{F}_{mem} = \frac{\kappa}{2}\int (C - C_0)^2\, dA + \kappa_G \int G\, dA + \gamma \int dA\,, \tag{3.1}$$

where C and G are the total and Gaussian curvatures of the membrane, C_0 is the spontaneous curvature caused by any asymmetry in the membrane structure, κ and κ_G are the bending rigidity and saddle-splay modulus and γ is the surface tension. As outlined in appendix C.1, the membrane free energy $\mathcal{F}_{mem} = \int f_{mem} dV$ can be rewritten in terms of a free energy density

$$f_{mem} = \frac{\kappa^*}{2}\left(-\varphi + \varphi^3 - \epsilon^2\nabla^2\varphi\right)^2 + \frac{K_\varphi}{2}\left(\nabla\varphi\right)^2\,. \tag{3.2}$$

This describes phase separation into two stable phases $\varphi = \pm 1$ with an interface of width ϵ separating the two phases [49, 86]. The bending rigidity κ of the interface is related to κ^* by $\kappa = (2\epsilon^3/3\sqrt{2})\kappa^*$. The final term in eqn. 3.2 penalises phase gradients and introduces a surface tension γ.

3.2.2 Mapping of simulation parameters to experimental values

In order to map dimensionless simulation parameters to physical units, one requires a physical reference scale for three independent simulation parameters, such as lattice spacing Δx, time step Δt and viscosity. For modelling the organisation of three-dimensional cell aggregates, we choose the lattice spacing to correspond to the size of individual cells, $\Delta x \approx 10\,\mu m$. Assuming disclinations in 3D move with similar velocities as $+1/2$ defects in 2D cell monolayers, we can compare the velocity of motile $+1/2$ disclination lines in our simulation $v_{SP}^{sim} = 0.002\Delta x/\Delta t$

with typical flow velocities around +1/2 defects in experiments $v_{SP}^{exp} \approx 20\mu m/h$ [31], which yields $\Delta t = 4s$. We run most simulations for up to 250000 time steps, corresponding to an observation window of $T \approx 12\,d$. Using the shear viscosity of tissues $\eta \approx 14\,kPa\,s$ [87, 88] as a viscous reference scale, we can map all simulation parameters to physical units, which are listed in Table 3.1.

Parameters	**Simulation units**	**Physical units**
Lattice spacing Δx	1	$10\,\mu m$
Time step Δt	1	$4\,s$
Viscosity η	1/3	$14\,kPa\,s$
Droplet radius R	15-30	$150 - 300\,\mu m$
Interface width ϵ	1.4	$14\,\mu m$
Surface tension $\gamma \approx \frac{2}{3\epsilon} K_\varphi$	0.05 - 0.19	$0.5 - 2 \cdot 10^{-2}\,N/m$
Bending rigidity $\kappa \approx \frac{\sqrt{2}\epsilon^3}{3}\kappa^*$	0.13	$1.4 \cdot 10^{-13}\,N\,m$
Elastic constant K_{LC}	0.1 - 0.2	$1 - 2 \cdot 10^{-7}\,N$
Active stress ζ	0.01-0.02	$100 - 200\,Pa$
Rotational diffusivity Γ_Q	0.1	$2 \cdot 10^{-6}\,(Pa\,s)^{-1}$
Mobility Γ_φ	0.2	$2 \cdot 10^{-15}\,m^2/Pa\,s$
Nematic bulk energy A_{LC}	0.75-1.5	$7.5 - 15\,kPa$
Droplet bulk energy A_φ	0.1	$1\,kPa$

Table 3.1: Mapping of Lattice-Boltzmann parameters to physical units using the lattice spacing Δx, the time step Δt and the tissue viscosity η as physical reference scales.

These parameters are in good agreement with mechanical properties of cell aggregates measured in experiments, with typical tissue interfacial tensions $\gamma \sim 10^{-2}\,N/m$ [87, 89–91]. and bending rigidity $\kappa \sim 10^{-13}\,Nm$ [92, 93]. Living cells embedded in a 3D matrix typically generate long-ranged contractile stress of the order of $\zeta \approx 200Pa$ close to the cell [94]. To estimate K_{LC} in experiments, we need to relate this effective constant of the nematic description to mechanical properties of individual cells. If we assume that cells in a dense aggregate must physically deform when the nematic order is distorted, the elastic energy associated with cell shape deformations is related to the cells' Young's modulus E and cell size Δx. From dimensional arguments, it follows $K_{LC} \sim E \cdot \Delta x^2$ [31]. The typical Young's modulus of fibroblasts, astrocytes and some endothelial cells is of the order $E \sim kPa$ [95, 96], which yields $K_{LC} \sim 10^{-7}N$.

It should be noted, however, that the mechanical properties of cell aggregates may vary greatly as the Young's modulus varies over several orders of magnitude, $E \sim 0.1 - 10 kPa$ for different cell types [96, 97]. Similar variations have been observed for the effective viscosity of tissues and cell aggregates, $\eta \sim 10 - 100\, kPa\, s$ [89, 90, 98].

3.3 Active surface anchoring

It is well known that in 2D active nematics the flows induced by active stresses at the interface with a passive isotropic fluid lead to an alignment of the director field at the interface [84]. This *active anchoring* of the director field is parallel to the interface for extensile stress and perpendicular for contractile stress. For 2D systems, the active alignment can be significant, but it is not immediately obvious whether the effect will persist in a 3D geometry, or how it will be affected by any defects present on the surface. Therefore, to investigate the effects of active anchoring in 3D, we measure the angle θ between the director field $\mathbf{n}$ and the surface normal at the interface of spherical droplets. Since there are more possible configurations for in-plane alignment ($\theta = \pi/2$) than for perpendicular alignment ($\theta = 0$), we use the distribution of $\cos\theta$ to quantify alignment effects. A randomly aligned director field results in a uniformly distributed $\cos\theta \sim \mathcal{U}[0, 1]$, while preferred perpendicular or in-plane alignment leads to bias of the distribution towards 1 or 0, respectively. The results in Fig. 3.2 show clear evidence that both extensile and contractile activity lead to strong active anchoring on the surface.

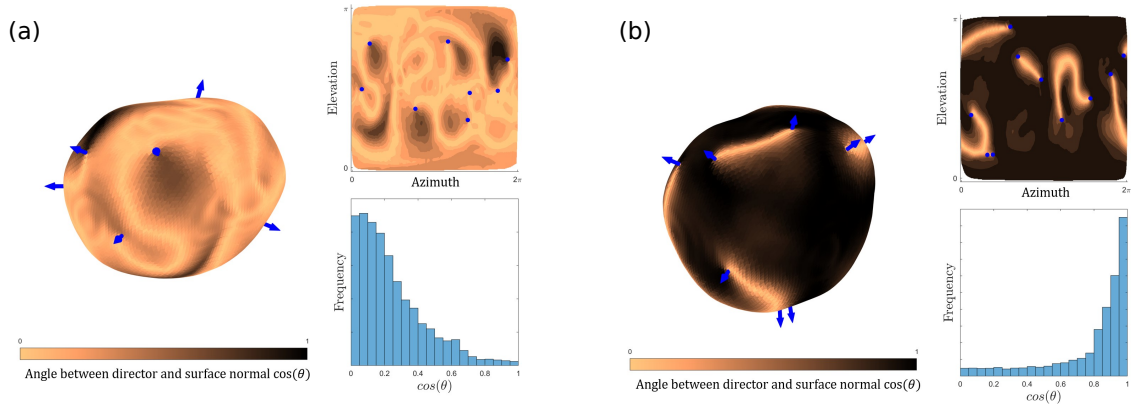


Figure 3.2: Surface alignment of the director field for **(a)** extensile and **(b)** contractile activity. Surface defects, shown as blue arrows, are connected via disclination lines running through the bulk. The surface alignment is indicated by colour bar, where orange (black) indicates in-plane (perpendicular) director alignment with respect to the interface. Upper right panels: surface alignment in projection. Lower right panels: distribution of surface angle $\cos(\theta)$ over the total surface area

The director orientation also shows signatures of the places where disclination lines end at the surface. Consider first the case of extensile activity. The director lies in plane over most of the surface, although there are localised regions with perpendicular alignment (see Fig. 3.2 a). The disclination lines present in the bulk of the droplet create quasi two-dimensional defects at the positions where they terminate at the interface which we shall term surface defects. The distribution of the twist angle β of surface defects has distinct peaks at $\beta = 0$ and $\beta = \pi$, showing that most defects on the surface are of wedge type (Fig. 3.3), corresponding approximately to 2D +1/2 and -1/2 configurations. There are less twist-type surface defects with $\beta \approx \pi/2$ as these defects introduce a perpendicularly aligned region in the vicinity of the defect, which is suppressed by active anchoring.

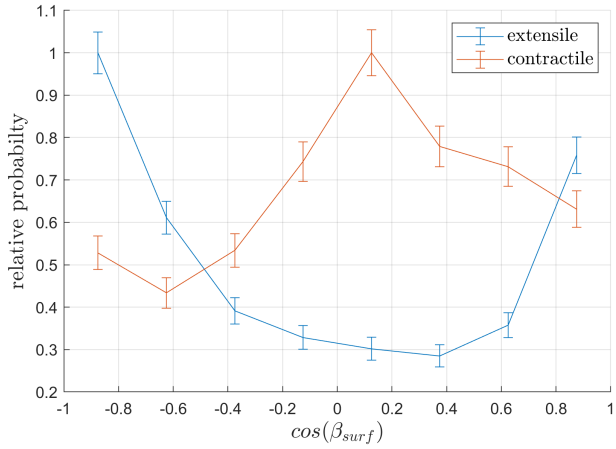


Figure 3.3: Distribution of twist angles of surface defects β_{surf}, i.e. at positions where disclination lines intersect the droplet interface, obtained from a time average in the active turbulent regime. Surface defects are preferentially wedge-like (twist-like) in extensile (contractile) systems where active anchoring favours in-plane (normal) director alignment. The relative probability is given by $N_i/max(\{N_i\})$, where N_i is the number of observations in bins of range $X_i \pm h/2$, and error bars denote the bin error $\sqrt{N_i}/max(\{N_i\})$. The averaging was performed over $T = 250000$ time steps, which is much longer than the average time it takes for a disclination line to move across the droplet $\tau_{SP} \approx 15000$.

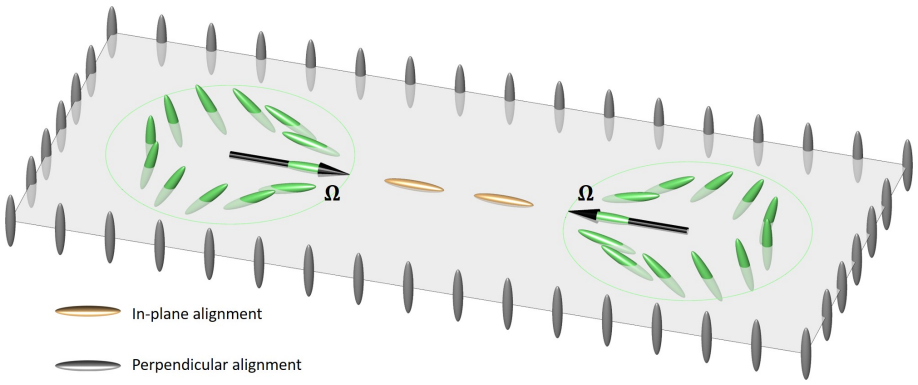


Figure 3.4: Adjacent twist-type surface defects (green) tend to align anti-parallel to each other in contractile systems to minimise the region of in-plane alignment. This results in lines of planar surface anchoring between the defects (orange directors).

A two-dimensional nematic sheet confined to the surface of a sphere always has at least four $+1/2$ defects present as the total topological charge is conserved and must add up to two, the Euler-characteristic χ of a sphere. It should be noted that active anchoring does not strongly confine the director field to the surface everywhere so the topological charge is not strictly conserved. By contrast, contractile activity leads to a remarkable stripe pattern in the director alignment on the surface. While most parts of the surface show strong perpendicular (homeotropic) active alignment,

this is interspersed with thin stripes of clear in-plane ordering (see Fig. 3.2 b). The stripes start and terminate at surface defects which are mostly twist-type with $\beta \approx \pi/2$ (Fig. 3.3). Wedge-type surface disclinations with $\beta = 0, \pi$ are suppressed as they would create a region of unfavourable in-plane alignment in the vicinity of the defect. Twist-type disclinations, on the other hand, only introduce a small region of in-plane alignment along a specific direction and are therefore favoured. Adjacent twist-type disclinations tend to align with their rotation vectors antiparallel, in a way that minimises the area of unfavourable in-plane alignment, thereby creating the observed stripe pattern (Fig. 3.4).

Perfect perpendicular alignment at the surface would prevent disclination lines in the bulk terminating there as all disclination lines introduce some degree of in-plane alignment at the surface. Indeed, because topological charge is conserved, a sphere with perfect homeotropic alignment at the interface would force the system to form a +1 hedgehog defect in the bulk. Like in two dimensions where a +1 disclination splits into two +1/2 defects, in three dimension the hedgehog defect forms a small +1 defect loop in the bulk [36, 38]. However, +1 defect loops are associated with large elastic energy of the liquid crystal which usually cannot be overcome by active anchoring.

3.4 Disclination line dynamics in spherical droplets

First we focus on the disclination line dynamics and active turbulence inside droplets with large surface tension which are essentially undeformed by active forces.

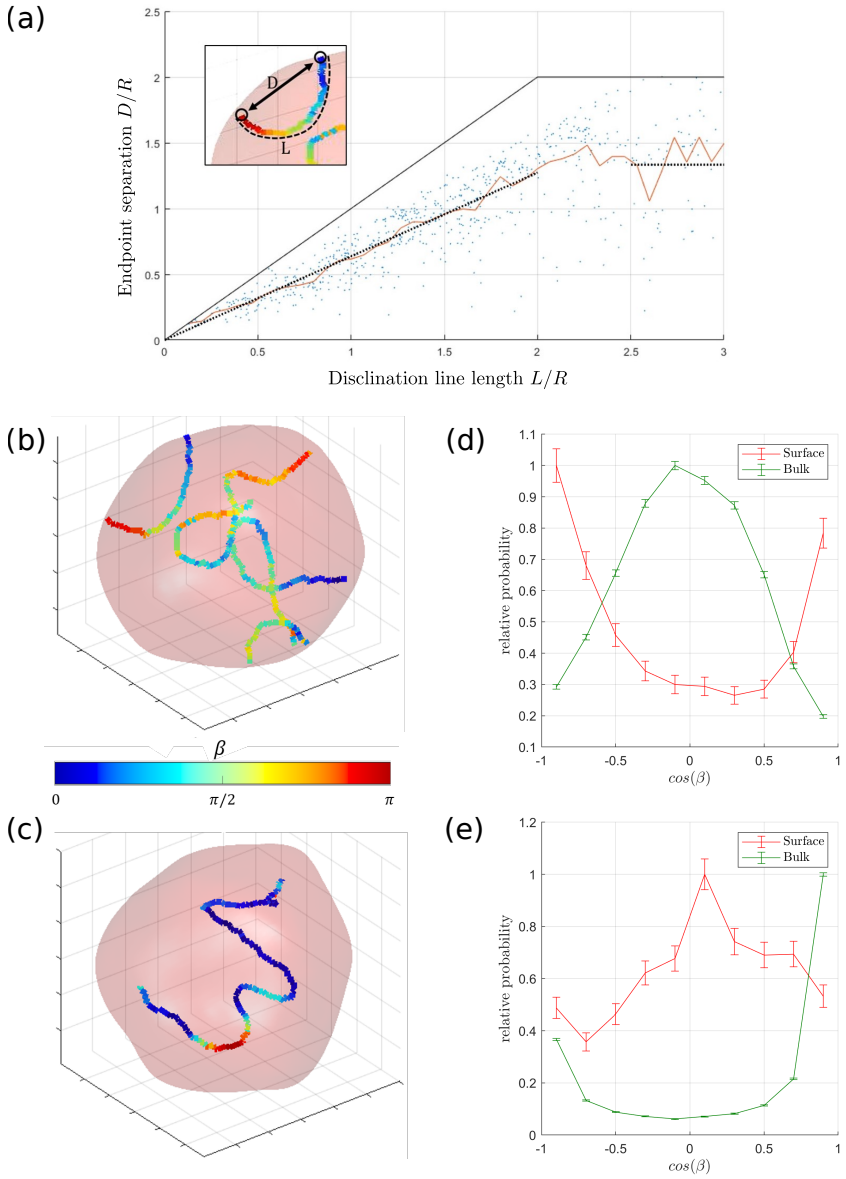


Figure 3.5: **(a)** The distance between endpoints of disclination lines D first scales linearly with the disclination line length L before plateauing at a finite value. For disclination lines which are small compared to the droplet radios ($L < R$), the mean endpoint separation (orange line) scales as $D \approx 2/\pi L$ (black, dotted line). This shows that disclination lines mainly nucleate/annihilate at the droplet's surface and grow/shrink as half-circles. The endpoints of very long disclination lines ($L \gg R$) are randomly distributed over the droplet's surface so the mean separation of endpoints converges towards $D/R \approx 4/3$ (dashed, horizontal line). Individual observations shown as blue dots. **(b,c)** Snapshots of disclination lines in an extensile (b) and contractile (c) droplet. The colour bar shows the twist angle β which characterises the director configuration which varies continuously along the line. **(d)** As a consequence of active anchoring, for extensile systems disclinations close to the surface tend to be wedge-type whereas those in the bulk tend to be twist disclinations as is evident from the distribution of β. **(e)** For contractile systems disclinations close to the surface slightly tend to be twist-type whereas those in the bulk tend to be wedge disclinations. The averaging over disclination lines was performed over $T = 250000$ time steps.

3.4.1 Defect nucleation and twist-angles in the presence of a surface

In the regime of active turbulence, disclination lines constantly form and annihilate. Previous investigations of active turbulence in bulk systems found that the dominant excitations of three-dimensional active nematics are charge-neutral disclination loops which undergo complex dynamics and recombination events [37]. In droplets however disclination lines do not need to form loops as they can also exist as growing or shrinking half circles or lines which terminate at the surface at positions $[\mathbf{x}_1, \mathbf{x}_2]$. The distance between endpoints (surface defects) of disclination lines $D = |\mathbf{x}_1 - \mathbf{x}_2|$ first scales linearly with the total length L of lines before plateauing at a finite value as the lines increase in length. For disclination lines which are short compared to the droplet radius ($L < R$), the mean endpoint separation scales as $D \approx (2/\pi)L$, showing that the lines mainly nucleate or annihilate at the droplet's surface as half-circles. The endpoints of very long disclination lines ($L \gg R$) are randomly distributed over the droplet's surface so the mean separation of endpoints converges towards $D/R \approx 4/3$ (Fig. 3.5 a).

The local properties of disclination lines can be classified by the twist angle β which varies continuously along the line. We find that the director profiles of disclination lines close to the surface are strongly influenced by active anchoring which favours wedge-type (twist-type) disclination lines for extensile (contractile) activity (Fig. 3.5). This is in contrast to the bulk of the drop where extensile (contractile) activity favours twist- (wedge)-type disclinations. The distributions of β at the surface and in the bulk are compared for extensile and contractile droplets in Fig. 3.5 d and Fig. 3.5 e, respectively. The excess of twist disclinations in extensile bulk systems has been recently confirmed by both experiments and simulations [36, 37].

3.4.2 Characteristic length-scales in 3D active turbulence

Behind the apparent disorder of three-dimensional active turbulence we identify an *active length-scale* $\ell_\zeta \propto \sqrt{K_{LC}/\zeta}$ which controls the average disclination line

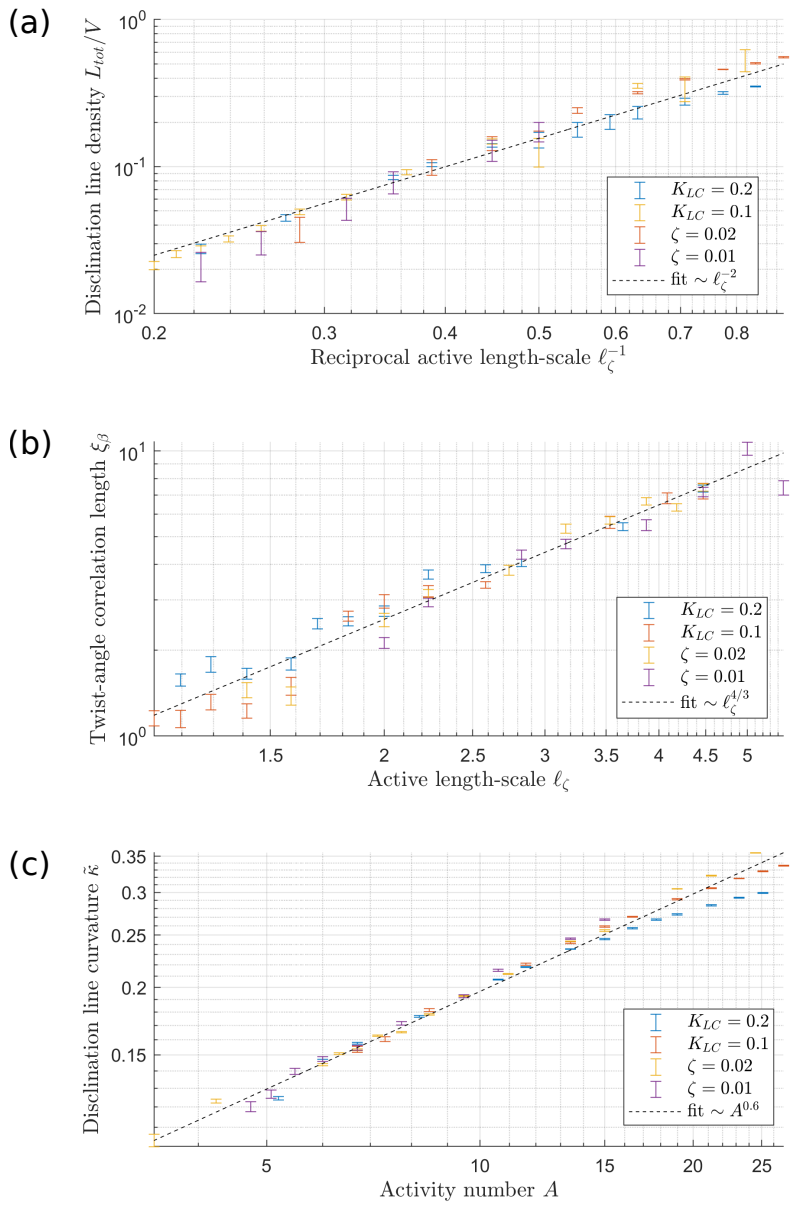


Figure 3.6: **(a)** Mean area density of disclination lines, defined as the total length L_{tot} of all disclination lines divided by the volume V, as a function of the inverse active length-scale $1/\ell_\zeta = \sqrt{\zeta/K_{LC}}$. Either K_{LC} or ζ were varied while the other parameter was set to a fixed value, which is indicated by the legend entries. **(b)** Persistence length ξ_β of the twist angle β as a function of the active length-scale. **(c)** Mean curvature $\tilde{\kappa}$ of disclination lines as a function of activity number $A = R/\ell_\zeta$. Averaging performed over $T = 20000$ time steps.

density and plays the same role as the active length-scale governing the decay of the vorticity correlations in two-dimensional active turbulence [23]. Fig. 3.6 shows the area density of disclination lines, defined as the total length L_{tot} of all disclination lines divided by the droplet volume V, as a function of K_{LC} and ζ, confirming that

it scales with the active length-scale as ℓ_ζ^{-2}. Moreover, by measuring the variation of twist angle β along individual disclination lines we obtain a characteristic length-scale ξ_β over which β decorrelates along disclination liens. We find that in the turbulent regime, the correlation length ξ_β of twist angle β scales with the active length-scale as $\xi_\beta \propto \ell_\zeta^{4/3}$. The exponent $4/3 > 1$ reflects that disclination lines are curved structures in three-dimensional space, hence correlations do not decay linearly along lines. Based on these observations, we define the dimensionless *activity number* $A = R\sqrt{\zeta/K_{LC}}$ as the ratio of droplet size R to active length-scale ℓ_ζ. The mean curvature $\tilde{\kappa}$ of disclination lines increases with activity number roughly as $\tilde{\kappa} \sim A^{0.6}$. Deviations at large activity A, equivalent to small active length-scale ℓ_ζ, are caused by the finite grid size of the simulation as ℓ_ζ approaches the grid resolution limit Δx.

3.4.3 Self-propulsion of line segments

Due to activity disclination lines move through the fluid with an associated transverse self-propulsion velocity $v_\perp^{SP}$ (eqn. 2.27). In addition, they are passively advected by the surrounding flow and thus the mean transverse velocity of disclination line segments is expected to follow $\langle v_\perp \rangle \approx u_{rms} + v_\perp^{SP}$, where u_{rms} denotes the root-mean-square velocity of the fluid inside the droplet. Surprisingly this simplified model of uncoupled, self-propelled line segments closely matches the velocity profile we observe in turbulent droplets for large β (Fig. 3.7 a). As disclination lines consist of line segments with varying self-propulsion velocities, more active line segments are elastically coupled with more passive segments. Passive line segments are thus pulled around by elastic interactions in addition to passive advection by the flow, which is the reason for the deviation of $\langle v_\perp \rangle$ from the theoretical prediction for small β.

We have argued that, as a consequence of active anchoring, the distribution of β varies between disclination lines near the surface and those deep into the bulk (Fig. 3.7 b, solid lines). This is mirrored in the average self-propulsion velocity (Fig. 3.7 b, diamonds). In extensile systems the wedge-type defects close to the surface on average move faster than the twist-type line segments in the bulk.

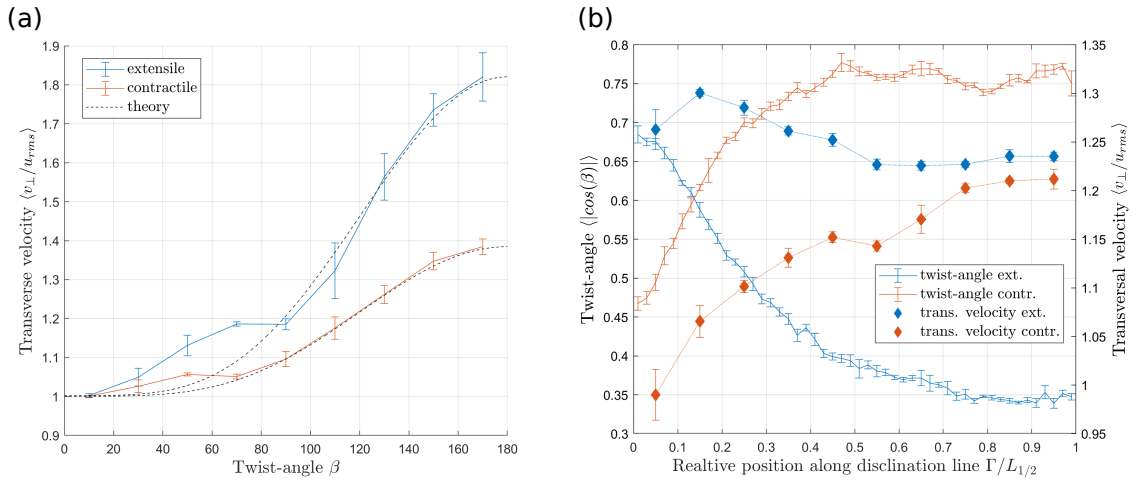


Figure 3.7: **(a)** Mean transverse velocity $\langle v_\perp \rangle$ of disclination line segments as a function of local twist angle β. The transverse velocity is normalised by the average root mean square velocity u_{rms} of the fluid. The fit is to the theoretical prediction eqn. (2.27), with the constant of proportionality obtained from a least-square fit. **(b)** Mean twist angle $\langle|\cos(\beta)|\rangle$ and mean transverse velocity $\langle v_\perp \rangle$ as a function of the relative position along disclination lines, where values 0 and 1 denote positions close to the surface and in the bulk, respectively. The relative position is measured as the ratio of Γ, which is the path length between each point and the nearest end-point of the disclination line, and $L_{1/2}$, which is half the total line length. Averaging performed over $T = 250000$ time steps.

Similarly, contractile activity causes line segments in the bulk, which are mostly wedge-type, to move faster than surface defects.

3.5 Activity-induced droplet deformations

After having analysed the disclination line dynamics and flows inside spherical droplets, we now consider lower values of the surfaces tension such that the active flows are strong enough to deform the droplet. In this section we show that extensile and contractile activity create qualitatively different force patterns acting on the interface, which leads to distinct morphologies of extensile and contractile droplets.

3.5.1 Extensile droplets

Finger-like protrusions

Extensile active stress leads to the formation of defect-mediated, finger-like protrusions. Unlike in stiff droplets, the active flow field around disclination lines close to the surface can push the interface outwards creating a bulge along the self-propulsion

direction of a disclination line (Fig. 3.8 a). As the disclination line continues to move outwards towards the interface, the local bulge extends and forms a thin protrusion.

Due to the reduced separation of interfaces compared to the spherical droplet, the properties of disclination lines inside protrusions are dominated by active anchoring which favours in-plane surface alignment. This causes disclination lines to span the width of the protrusion as a straight line with most line segments resembling wedge-type $+1/2$ defect profiles ($\beta \approx \pi$), thereby enhancing the directed self-propulsion of the disclination line even further. The $+1/2$ defect profile aligns along the protrusion axis as this configuration satisfies the in-plane anchoring condition everywhere at the surface (Fig. 3.8 b,d). This quasi-two dimensional motion of $+1/2$ defect lines has also been observed in active nematic films confined to a channel below a critical wall separation [99]. Wedge-type $-1/2$ defect profiles ($\beta \approx 0$) are not observed in protrusions as they are passive and lack the self-propulsion necessary to form a bulge in the first place.

The $+1/2$ defect line eventually reaches the tip of the growing protrusion and moves out of the nematic droplet, leaving behind a homogeneous director field which is aligned along the protrusion axis (Fig. 3.8 c,e). Thereby an area of perpendicular surface alignment is introduced at the end of protrusions, which are points of large negative mean curvature. The surface alignment $\cos(\theta)$ is therefore correlated to the local mean curvature of the interface. In the absence of disclination lines mediating active forces, the aligned protrusions slowly retract due to surface tension and bending energy.

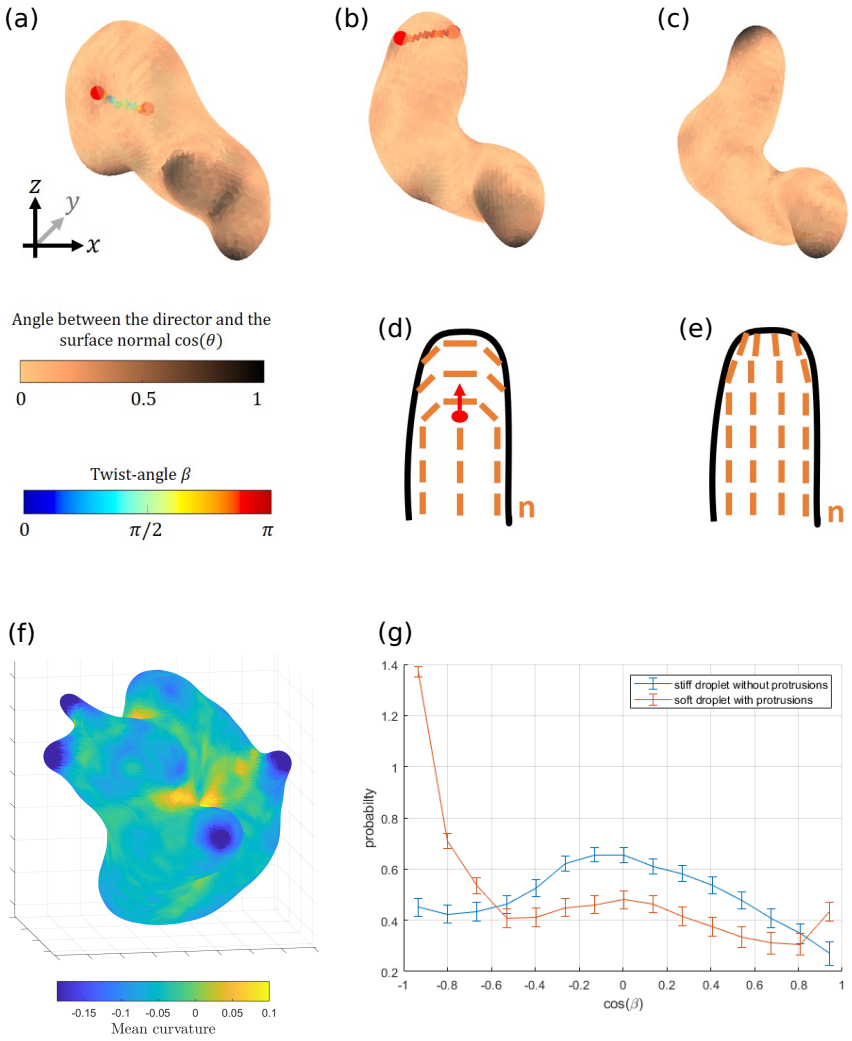


Figure 3.8: **(a-e)** Formation of finger-like protrusions by motile disclination lines shown by three snapshots from simulations with droplet size $R = 15$ at times $t_1 = 71500$ $t_2 = 72500$ $t_3 = 73500$. **(a-c)** show the three-dimensional droplet shape with colour coding showing the local surface alignment of the director field. **(a)** Disclination line with varying twist angle β moves towards the interface. Active flow pushes the interface outwards creating a bulge along the self-propulsion direction of the disclination line. **(b)** The small protrusion width combined with in-plane alignment at the surface stabilises the disclination line into an almost straight configuration with $\beta \approx \pi$. **(c)** Disclination line moves out of the droplet leaving behind a defect-free protrusion with an aligned director field. Disclination lines exit protrusions as nearly straight lines and violate in-plane alignment within a small area as active anchoring is not strong enough to force the creation of a surface point-defect. **(d,e)** Schematic diagram of the director field and active forces. The red arrow in (d) denotes the self-propulsion direction of the $\beta \approx \pi$ disclination lines. As shown in panel (c), disclinations leave behind an area of perpendicular surface alignment (dark regions) at the end of protrusions which slowly retract due to surface tension and bending rigidity. **(f)** Larger droplets of size $R = 30$ form many protrusions extending into the surrounding medium. Colour coding shows the local mean curvature of the droplet surface. **(g)** Protrusion formation relies on the presence of motile $+1/2$ disclination lines pushing the interface outwards. This is reflected by a sharp peak at $\beta \approx \pi$ in the probability distribution of twist angle β for disclination lines in soft droplets with many protrusions compared to stiff droplets which stay spherical.

To further quantify the mechanism of protrusion formation we measured several properties of disclination lines as a function of radial position x_r, with the droplet's centre of mass being the reference point of a spherical coordinate system. For approximately ellipsoidal droplet shapes, x_r can be used as a proxy to divide the initially spherical droplet of radius R into a bulk domain ($x_r < R$) and a protrusion domain ($x_r > R$). Disclination lines in the bulk ($x_r < R$) of soft droplets undergo chaotic motion ($\langle \mathbf{v_r} \rangle \approx 0$) and are mostly twist type. By contrast, in protrusions ($x_r > R$) disclination lines mostly consist of $+1/2$ line segments ($\approx 70\%$) and show persistent self-propulsion along the radial protrusion axis ($\langle \mathbf{v_r} \rangle \gg 0$, see Fig. 3.9 a). Disclination lines in protrusions are nearly straight and their total length L is limited by the width of the protrusion ($L(x_r) \approx$ const for $x_r > R$, see Fig. 3.9 b).

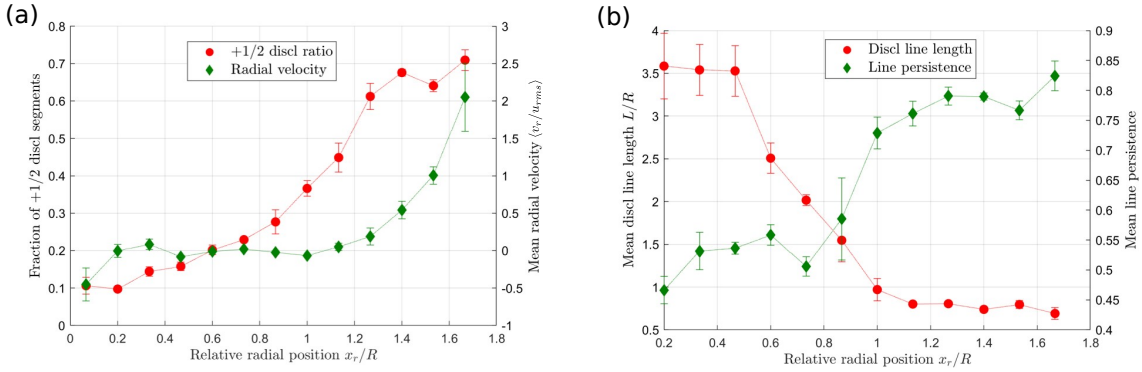


Figure 3.9: Disclination line properties for extensile activity as a function of radial position x_r in an initially spherical droplet of radius R. **(a)** Most of the disclination lines in protrusions ($x_r > R$) show a $+1/2$ director configuration for which the self-propulsion velocity v_r points radially outwards. **(b)** Disclination lines in protrusions ($x_r > R$) are nearly straight lines whose length is limited by the diameter of the protrusion. The radial component of the self-propulsion velocity v_r was obtained by taking the droplet's centre of mass as the reference point of a spherical coordinate system. The fraction of $+1/2$ disclination lines was defined as the fraction of disclination line segments with twist angle $3/4\pi \leq \beta \leq \pi$ and the persistence of disclination lines as the ratio of endpoint distance over total line length. The averaging was performed over $T = 100000$ time steps, which is much longer than the morphological time scale on which protrusions formation happens (approximately 2000 time steps, see Fig. 3.8).

Droplets of sizes much larger than the active length-scale $R \gg \ell_\zeta$ are strongly deformed and protrusions do not always grow along the radial axis (Fig. 3.8 f), thereby rendering the spherical approximation unsuitable. Still it can be observed

that +1/2 defect lines are much more frequent in soft droplets with protrusions than in spherical droplets without protrusions (Fig. 3.8 g).

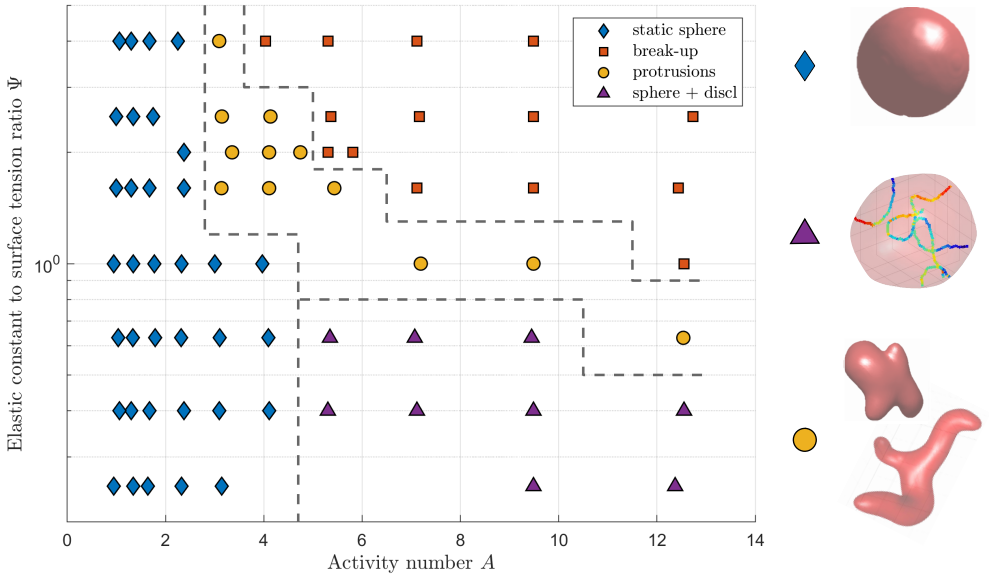


Figure 3.10: Morphology diagram of extensile droplets ($\zeta > 0$) as a function of the activity number $A = R\sqrt{\zeta/K_{LC}}$ and the elastic constant to surface tension ratio K_{LC}/K_φ. Parameters ζ and K_{LC} were varied while the surface tension and droplet size were fixed to one of the following values: $K_\varphi \in \{0.1, 0.2\}$ $R \in \{15, 30\}$.

Phase diagram

The morphology of extensile droplets is determined by two control parameters: The activity number $A = R\sqrt{\zeta/K_{LC}}$ controls the density of disclination lines inside the bulk of droplets while the ratio of elastic constant to surface tension $\Psi = K_{LC}/K_\varphi$ quantifies the energetic cost associated with nematic deformations in the bulk compared to deformations of the interface (assuming surface tension dominates the bending stiffness). The morphology of droplets as a function of A and Ψ is shown in Fig. 3.10. For very stiff interfaces ($\Psi \ll 1$), droplets are nearly spherical and host disclination lines if the activity A is sufficiently large (blue diamonds, purple triangles). Soft interfaces ($\Psi \geq 1$) however allow the formation of finger-like protrusions as soon as disclination lines are formed inside droplets (yellow circles). If active forces become much larger than the passive restoring force of the interface, active flows tear apart the droplet which breaks up into smaller parts (orange squares).

3.5.2 Contractile droplets

Droplet invagination

We now consider contractile activity which causes droplet invagination or the formation of comb-shaped droplet deformations creating wrinkle patterns on the surface. Unlike protrusion formation in extensile systems, droplet deformations in contractile systems originate from smooth director field deformations and are not mediated via disclination lines.

In contractile systems active anchoring favours normal surface alignment. Every spherical or topologically equivalent surface with normal surface alignment everywhere enforces the formation of at least one +1 disclination-loop in the bulk due to topological constraints. These loops are usually associated with a large elastic energy cost due to strong deformations of the director field and thus are only observed in drops if strong normal anchoring is enforced by additional terms in the free energy. Otherwise, in the absence of disclination lines, the director field forms a ring with in-plane surface alignment encircling the droplet (Fig. 3.11 a) to maximize the area of perpendicular surface alignment favoured by active anchoring while avoiding the formation of a +1 defect-loop in the bulk. The ring of in-plane surface alignment is associated with nematic bend deformations in the bulk; thus we will refer to this structure as a *bend-ring* from now on (Fig. 3.11 d). Contractile activity causes the bend-ring to push outwards, thereby deforming the droplet to an oblate ellipsoid until passive forces arising from surface tension and membrane rigidity counterbalance the active force.

If active forces are small compared to the passive restoring forces arising from membrane and director field deformations, the oblate bend-ring configuration is stable. Perturbations of ring shape and position are associated with increasing elastic deformations of the membrane and the director field, thereby creating an energy barrier which stabilises the configuration (Fig. 3.11 g). The exact free energy profile depends on model parameters such as the surface tension K_ϕ, membrane rigidity κ, nematic elastic constant K_{LC} and bulk properties.

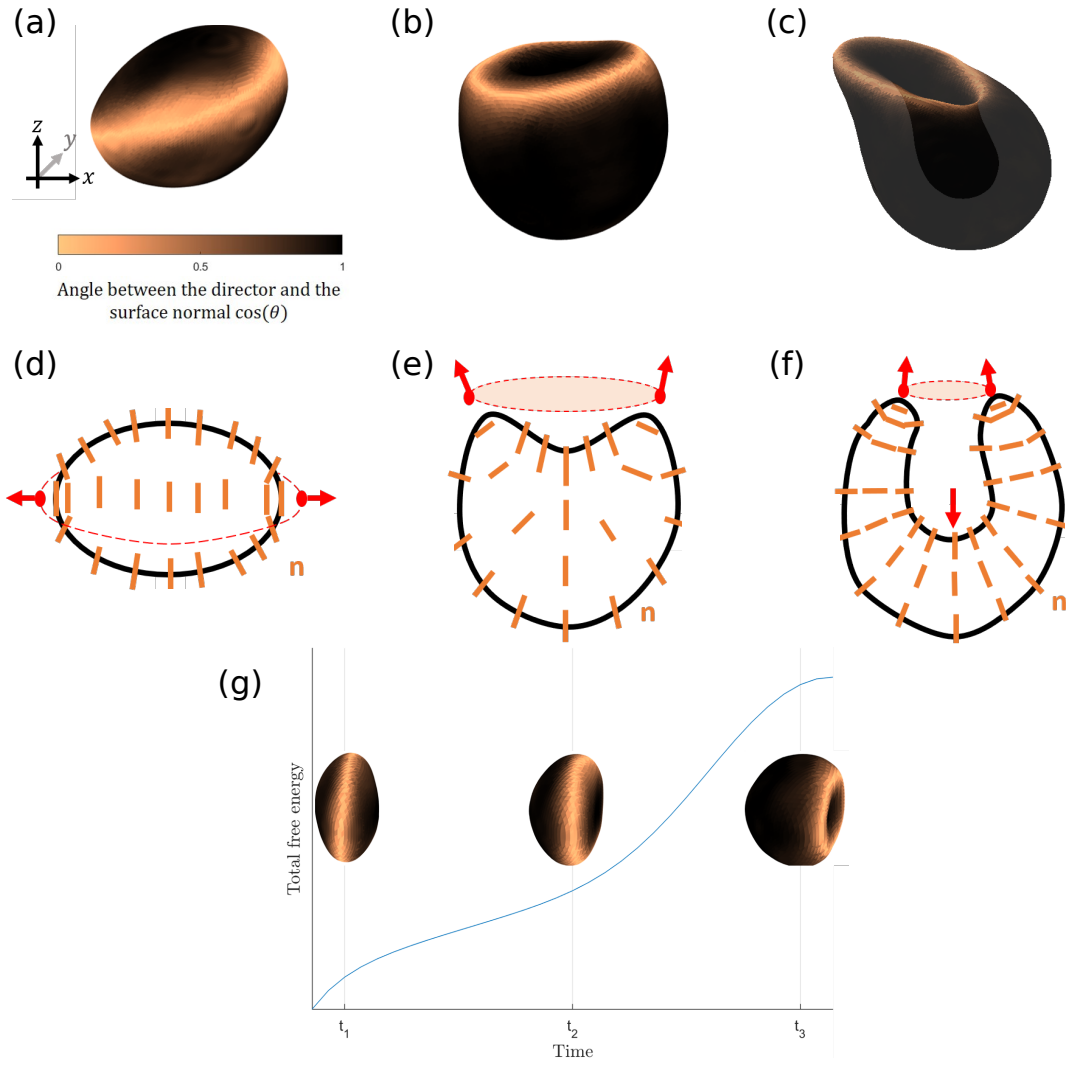


Figure 3.11: Initiation of droplet invagination by contractile activity. **(a-c)** show the three-dimensional droplet shape with colour coding indicating the local surface alignment of the director field. **(d-f)** are schematic diagrams of the director field **n**, showing the active forces (red arrows) and the position of the bend-ring (red, dotted circle). **(d)** The ring of in-plane alignment at the equator causes nematic bend deformations in the bulk. Contractile activity causes these bend deformations to push outwards (red arrows), thus deforming the droplet to an oblate shape. **(e)** While the ring of in-plane alignment moves towards one of the poles, the bend deformations in the bulk point perpendicular to the surface which causes the active forces to develop a component pointing towards the pole. This creates a dent in the centre of the ring. **(f)** Due to the perpendicular surface alignment caused by active anchoring, the dent in the centre of the ring leads to a director splay deformation in the bulk. Contractile activity causes this splay deformation to push inwards, thus increasing the depth of the dent. **(g)** Total free energy $\mathcal{F}$ as a function of time at different invagination stages $t_1 < t_2 < t_3$. Activity initially causes the formation of a bend-ring at the equator which contracts and moves towards one of the poles if active forces are sufficiently large to overcome the energy barrier associated with the contracting bend-ring. The exact droplet shapes and free energy profiles depend on model parameters such as the surface tensions, membrane rigidity, nematic elastic constant and bulk properties. Snapshots created from simulation with elastic constant $K_{LC} = 0.4$ at times $t_1 = 15000$ $t_2 = 30000$ $t_3 = 50000$.

If active forces are sufficiently strong to overcome the passive restoring force, however, the bend-ring at the equator is unstable. It contracts while moving towards one of the poles and its motion results in invagination leading to a cup-shaped configuration of the droplet. This instability arises from contractile active forces generated by the director field of the bend-ring which pushes outwards against the bend deformation (Fig. 2.7 a). Any small deviations from a perfect ellipsoidal droplet shape cause a component of the active flow to point towards one of the poles. The resulting droplet deformation rotates the axis of the bend-ring further towards the pole thereby in turn further increasing the active force component in the direction of the pole (Fig. 3.11 b,e).

As the contracting bend-ring approaches the pole, it creates an area of splay deformation in its centre due to active anchoring enforcing perpendicular surface alignment (Fig. 3.11 e). This splay deformation sets up an active flow pointing inwards (Fig. 2.7 b). The outward pointing forces of the bend-ring together with the inward pointing forces in its centre combine to drive droplet invagination (Fig. 3.11 c,f). If the magnitude of active stress ζ is not significantly reduced after complete invagination, this process eventually causes the cavity that is driven into the drop to break off (cup closure) as the passive restoring forces resulting from membrane rigidity and surface tension are not sufficient to compensate the active forces. However, if the system is active only for a certain amount of time and $\zeta(t)$ is reduced after the initial invagination, the cup-shaped drop can be stabilised, analogous to the natural course of morphogenetic events, which are controlled by biochemical signals and begin and end at a predefined time [100].

Run-and-tumble motion

Alternatively, if the interface is too stiff for active forces to initiate drop invagination, droplets perform an active *run-and-tumble* motion (Fig. 3.12). Instead of a large cavity, only a small dip is formed at the centre of the bend-ring where the interface resists further deformations and the splay configuration of the director field leads to flows which push the droplet forwards (run phase). Eventually, the director

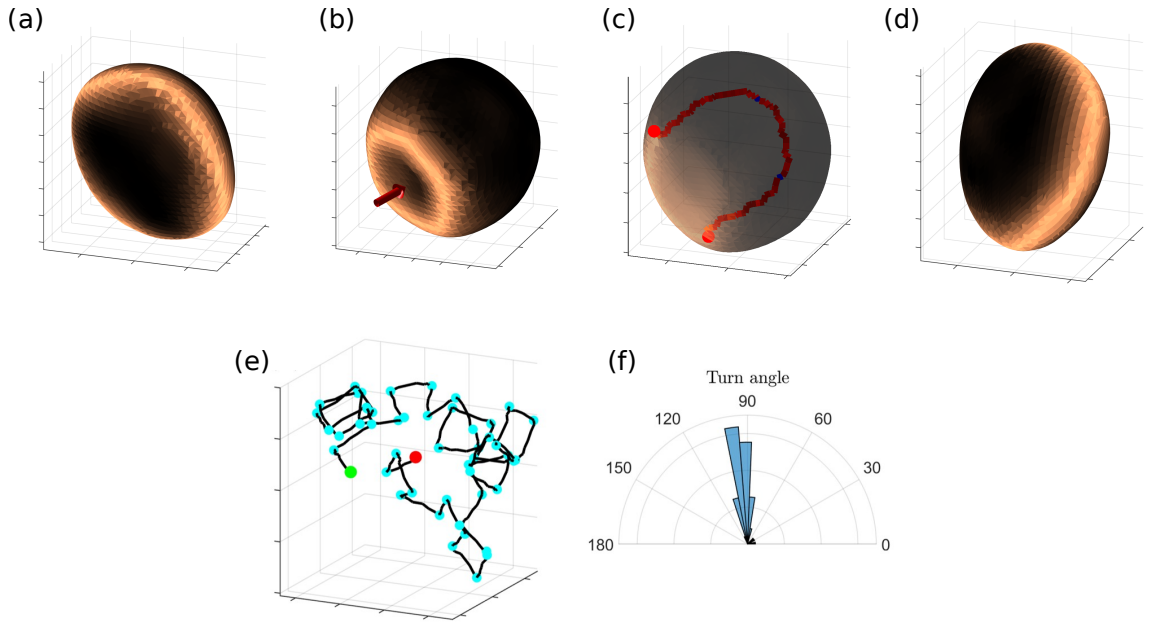


Figure 3.12: Droplets perform a *run-and-tumble* motion if the interface is too stiff for active forces to cause complete droplet invagination. **(a-d)** A bend-ring at the equator deforms the droplet to an oblate shape (a), which then shrinks, forming a dip at the centre of the bend-ring where a splay deformation in the bulk pushes the droplet forward (b). Then the elastic deformations relax via the nucleation of a $\beta = \pi$ half-loop (c). The self-propulsive disclination line moves through the droplet and eventually reaches the interface. This event, which we will refer to as a tumbling event, re-orientates the bend-ring along a random direction perpendicular to the axis of the dip and the process repeats (d). **(e,f)** The long time dynamics of the droplet's motion is diffusive and resembles a three-dimensional random walk which is known in in polymer physics as a freely-rotating chain with a turn angle $\theta = 90°$. Tumbling events are shown as cyan dots and the start and end points are shown as red and green dots, respectively. Snapshots and random walk created from simulations with droplet size $R = 15$

.

deformations relax via the nucleation of a $\beta = \pi$ half-loop and the self-propulsive disclination line travels from the position of the dip to the opposing interface. This re-orientates the bend-ring along a random direction perpendicular to the axis of the dip (tumble phase) and the process repeats along the new direction (Fig. 3.12 a-d). During the run phase the droplet approximately moves on straight lines, after which it makes a 90° turn into a random direction. The long time dynamics of the droplet's motion is diffusive and resembles a three-dimensional random walk known as a freely-rotating chain in polymer physics with a turn angle $\theta = 90°$ (Fig. 3.12 e,f).

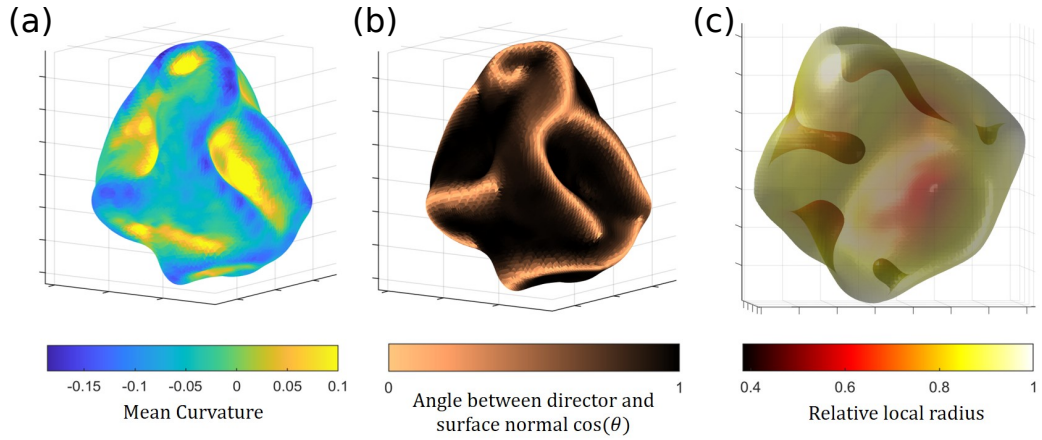


Figure 3.13: Snapshots of a contractile drop showing **(a)** the mean curvature and **(b)** the orientation of the director field on the surface. Contractile droplets which contain disclination lines show stripes of in-plane director alignment on the surface which connect endpoints of the disclination lines in the bulk. Bend and splay deformations of the director field near the surface create comb-shaped deformations along the stripes of in-plane alignment, resulting in a wrinkle pattern. **(c)** In between stripes of in-plane alignment, dimples and valleys are driven into the drop as shown by a semi-transparent surface plot.

Active surface wrinkling

In contractile droplets which are larger than the active length-scale $R \gg \ell_\zeta$, many disclination lines are present in the bulk and the surface shows characteristic stripes of in-plane director alignment connecting the endpoints of disclination lines (Fig. 3.2 b). The stripes on the surface are associated with nematic bend deformations in the bulk which induce active forces pushing outwards. This creates comb-shaped deformations along the stripes of in-plane alignment, resulting in a surface wrinkle pattern which we will term *active wrinkling* (Fig. 3.13). In addition, the droplet deformation causes the perpendicularly aligned surface areas between in-plane stripes to form splay deformations in the bulk, which cause inward pushing, active forces that create dimples and valleys, further enhancing the wrinkle pattern. Along the in-plane ridges the mean curvature is negative while in the centre of holes it is positive. Surface alignment $\cos(\theta)$ is therefore correlated to the local mean curvature of the interface with in-plane surface alignment ($\cos(\theta) \approx 0$) associated with points of negative mean curvature and perpendicular surface alignment ($\cos(\theta) \approx 1$) predominating at points of positive mean curvature.

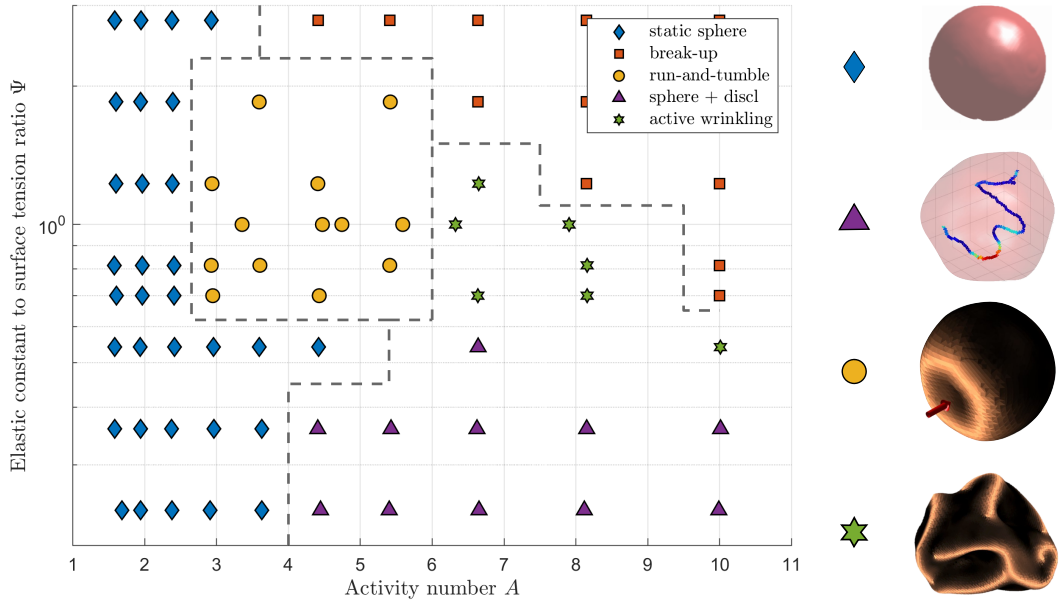


Figure 3.14: Morphology diagram of contractile droplets ($\zeta < 0$) as a function of the activity number $A = R\sqrt{\zeta/K_{LC}}$ and elastic constant to surface tension ratio K_{LC}/K_φ. There is a smooth transition between spherical droplets with disclination lines and active wrinkling. Parameters ζ and K_{LC} were varied while the surface tension and droplet size were fixed to one of the following values: $K_\varphi \in \{0.1, 0.2\}$ $R \in \{15, 30\}$.

Phase diagram

As for the extensile case, the morphology of contractile droplets is determined by the activity number $A = R\sqrt{\zeta/K_{LC}}$ and ratio of elastic constant to surface tension $\Psi = K_{LC}/K_\varphi$ (Fig. 3.14). Very stiff interfaces ($\Psi \ll 1$) cause droplets to be nearly spherical and host disclination lines if activity A is sufficiently large (blue diamonds, purple triangles). If interfaces are sufficiently soft ($\Psi \approx 1$), droplets can be either be static, oblate ellipsoids without disclination lines (blue diamonds), perform an run-and-tumble motion (yellow circles) or form active surface wrinkles (green stars). For very soft interfaces ($\Psi \gg 1$), droplets are static ellipsoids at low activity and full droplet invagination takes place at larger activity, leading the droplet to eventually break-up (orange squares).

3.6 Summary and Discussion

In this chapter we have investigated the morphology and defect dynamics in active deformable droplets in three dimensions, considering both extensile activity, as present in experimental systems such as MT–kinesin mixtures [101], human bronchial epithelial cells [102] and Madine–Darby canine kidney (MDCK) cells [30], as well as contractile activity, which is found in systems such as mouse fibroblast cells [33] or actomyosin gels [103]. We have shown that active stresses cause in-plane (extensile) or perpendicular (contractile) surface alignment of the director field at the interface of droplets. Unlike thermodynamic surface anchoring, which involves an anchoring free energy, *active anchoring* is a hydrodynamic effect due to the flows driven by gradients of the nematic ordering $\mathbf{Q}$ at the interface. Active anchoring has important consequences for the dynamics of disclination lines close to the interface, such as the preferential formation of wedge-like surface disclinations in extensile systems or the creation of in-plane aligned stripes connecting twist-like surface disclination in contractile systems. This in turn triggers the formation of finger-like protrusions in soft, extensile droplets or the creation of surface wrinkles and droplet invagination in contractile systems. Furthermore, we applied the ideas of 2D active turbulence, such as defect velocities and the existence of an active length-scale, to three dimensions. We identified an active length-scale ℓ_ζ of three-dimensional active turbulence, which controls both the density of disclination lines and the correlation length of the twist angle β along disclination lines in the bulk of nematic droplets.

Recent work has interpreted several 2D biological systems including bacterial biofilms [29, 64], epithelial tissue [30], spindle-shaped cell monolayers [33] and actin fibres in regenerating Hydra [104] in terms of the theories of active nematics. It is interesting to ask whether similar ideas may prove useful in 3D to describe biological systems in which nematic constituents, such as protein filaments, eukaryotic cells or bacteria, are organised as nematic, 3D structures with a confining interface. There are several examples where cells migrate collectively as a cohesive group, thereby maintaining supracellular properties such as collective force generation and tissue-scale hydrodynamic flow [19, 105, 106]. For example, in some modes

of collective cell movement implicated in cancer invasion, a blunt bud-like tip consisting of multiple cells that variably change position and lack well-defined leader cells protrudes from the tumour [107, 108]. Hence, the natural appearance of finger-like protrusions in active nematic droplets could serve as a new approach to explain collective cell invasion of tumours.

In eukaryotic cells, membrane shapes are predominantly controlled by the cortical actin cytoskeleton underlying the cell membrane, which produces contractile stresses. It has been observed that membrane shapes mainly depend on the actin thickness, where thin shells show a cup-shaped deformation and thick shells produce membrane wrinkles [109]. Our work provides a possible link between contractile activity and the emergence of cell-surface ruffles, circular dorsal ruffles (CDRs) and caveolae [110–112] at the surface of cells. Surface invagination which plays a role in active transport through cell membranes might also be related to local contractile forces. During macropinocytosis (fluid endocytosis), extracellular fluid is brought into the cell through an invagination of the cell membrane forming a small vesicle inside the cell. Vesicles form from cell-surface ruffles that close first into open cups (ruffle closure) and then into intracellular vesicles (cup closure) [113, 114], which is reminiscent of the dimples that are driven into contractile drops. Some morphologies observed in contractile drops, such as partial invagination and run-and-tumble motion, are known to also occur in active polar droplets [115, 116].

Previous investigations of two-dimensional active nematics confined to the surface of 3D shells explored the connection between 2D topological defects and shell morphology [117]. Up to now, most of the research on three-dimensional active nematics has been focused on the topology and dynamics of closed disclination loops in the bulk or disclination lines in fixed geometries [36–38, 81, 82]. With the work highlighted in this chapter we expanded the current understanding of three-dimensional active nematics by investigating the interplay between active anchoring, motile disclination lines and droplet deformations.

Take-home message:

Extensile and contractile active stress create active anchoring of the director at the surface and drive distinct droplet deformations.

4

Concerning activity gradients

In the previous chapter we investigated the dynamics of systems in which the magnitude of the active stress was uniform. However, both synthetic systems and living matter are rarely homogeneous and often feature chemical concentration gradients, heterogeneous distribution of cell types or other forms of spatial heterogeneity, leading to variations of activity levels across systems. In this chapter we numerically investigate how spatial variations of active stress affect bulk active nematic systems in two and three dimensions. We find that in the absence of defects, activity gradients drive flows which re-orient the nematic director field and thus function as an effective anchoring force. At high activity, defects are created and the system transitions into active turbulence. In 2D systems active torques robustly align +1/2 defects parallel to activity gradients, with defect heads pointing towards contractile regions. In 3D active nematics disclination lines preferentially lie in the plane perpendicular to activity gradients due to active torques acting on line segments. The average orientation of the defect structures in the plane perpendicular to the line tangent depends on the defect type: wedge-like +1/2 defects align parallel to activity gradients, while twist defects are aligned anti-parallel.

4.1 Introduction

A major research theme in active matter has been to investigate how to control the chaotic flows and defect motion in active materials. Guiding active flow and defects along selected paths is likely to be a prerequisite to using active matter for powering micro-machines or targeting the delivery of drugs. It has been proposed that this control can be achieved in 2D systems by patterns of activity on a substrate. This causes the orientation of $+1/2$ defects to align along activity gradients and hence the defects to move along paths defined by activity patterns [118, 119]. Further work has investigated the alignment of individual topological defects by activity gradients in 2D using theoretical arguments and numerical simulations [120, 121]. More recently it has also proved possible to design active materials that allow imaging of a three-dimensional (3D) active nematic and, in particular, the associated motile disclination loops and lines [37]. These articles have focused primarily on how activity patterns affect flows and the alignment of individual topological defects, and it is still poorly understood how activity gradients affect systems in the absence of topological defects or how well the concept of 2D topological defects as effective oriented particles translates to disclination line segments in 3D materials.

In this chapter we aim to close this gap by numerically investigating how activity gradients affect 2D and 3D active nematics. We start in section 4.2 by outlining simulation methods we used to solve the equations of motion. In section 4.3 we show how non-uniform activity creates active forces which, in the absence of defects, set up flows which rotate the nematic director field. This effectively creates an active force which favours either normal or tangential alignment of the nematic director with respect to activity gradients for contractile or extensile active stress, respectively. In the following section in section 4.4, we show that activity gradients in 2D active turbulence induce polar order of $+1/2$ defects, which is consistent with previous theoretical predictions considering active torques on isolated defects [120]. In section 4.5 we investigate how activity gradients in 3D systems affect nematic alignment and the polarization of disclination lines. We find that disclination lines which locally resemble $+1/2$ or twist defects are polarized in opposite directions,

aligning parallel or anti-parallel to activity gradients, respectively. The last section 4.6 summarises the key results, highlights similarities between activity gradients and active-passive interfaces and points out connections to experiments.

4.2 Simulation method

We solve the continuum equations of active nematohydrodynamics (eqn. 2.18, eqn. 2.1 and eqn. 2.2) using the hybrid lattice Boltzmann-finite difference method introduced in the previous chapter. For the liquid crystal we use the bulk free energy eqn. 2.12 and choose coefficients $\mathcal{A} = 0.08$, $\mathcal{B} = -4.3$, $\mathcal{C} = 4.3$ such that nematic ordering $S_0 > 0$ is favoured in equilibrium. Simulations were performed on 2D and 3D lattices of sizes 180×90 and $60 \times 60 \times 60$, respectively, and discrete space and time steps were chosen as unity. We used periodic boundary conditions for the simulation box and the system was initialized as $\mathbf{u} = \mathbf{0}$, $S = 0.3$ and random director field $\mathbf{n}$. The detection of topological defects and disclination lines is outlined in appendix B.

To investigate the role of activity gradients, we consider periodic variations of activity along one coordinate axis with alternating extensile ($\zeta > 0$) and contractile activity ($\zeta < 0$) in two and three-dimensions,

$$\zeta(\mathbf{x}) = \zeta_{max} \cdot \cos(\mathbf{k} \cdot \mathbf{x}) \,, \tag{4.1}$$

with wave-vector $\mathbf{k}$ indicating the direction $\mathbf{k}/|\mathbf{k}|$ and wavelength $\lambda = 2\pi/|\mathbf{k}|$ of activity patterns (Fig. 4.1 a,f). In the following we will denote the coordinate axes parallel and perpendicular to the plane of constant activity as the tangential and normal direction, respectively. We define a dimensionless activity number $\mathcal{A} = \lambda\sqrt{|\zeta_{max}|/K_{LC}}$ as the ratio of the wavelength λ to the active nematic length-scale $\ell_\zeta = \sqrt{K_{LC}/|\zeta_{max}|}$. For more complex, aperiodic activity patterns $\mathcal{A}$ can be defined as the ratio of a characteristic domain size L to the active length-scale ℓ_ζ.

We used the following parameter values unless otherwise stated: $\lambda = 30$, $\zeta_{max} = 0.08$, $K_{LC} = 0.12$, $\Gamma_{LC} = 0.34$, fluid density $\rho = 1$, bulk pressure $p = 0.25$ and viscosity $\eta = 2/3$ in lattice-Boltzmann units.

4.3 Active forces in the absence of defects

We start by presenting results for systems with heterogeneous activity in which the magnitude of active stress is too small to create active defects. Assuming variations in the order parameter $\mathbf{Q}$ are small compared to variations in active stress ζ, the active force density $F_i = -\partial_j(\zeta Q_{ij})$ can be approximated by

$$\mathbf{F}_{act} \propto S\left(\nabla\zeta - 2\left(\nabla\zeta \cdot \mathbf{n}\right)\mathbf{n}\right) , \tag{4.2}$$

where activity gradients $\nabla\zeta$ are the main driving force of flows. This approximation is justified as long as $|\nabla\zeta| \gg |\zeta\ \mathbf{n}(\nabla \cdot \mathbf{n})|$, which is satisfied in the transition area between extensile and contractile domains ($\zeta \approx 0$) or in the absence of topological defects which create strong distortions in the order parameter in active regions. The force component along the tangential direction, perpendicular to the activity gradient, is [122]

$$F^{||}_{act} = -2|\nabla\zeta| \cdot S \cos\theta \sin\theta , \tag{4.3}$$

where $\theta \in [-\pi/2, \pi/2]$ denotes the angle of the director field $\mathbf{n}$ with respect to the activity gradient vector $\nabla\zeta$. Whenever $\mathbf{n}$ is not aligned parallel or perpendicular to a finite activity gradient, active forces will generate flows along the tangential direction, which scale with the magnitude of the activity gradient, $u^{||} \propto F^{||}_{act} \propto |\nabla\zeta|$ (Fig. 4.1 b,d). As a consequence of the co-rotation term $\mathcal{W}$ in eqn. 2.18, the resulting shear flows rotate the director field $\mathbf{n}$ until a stable equilibrium is reached where the elastic energy associated with director deformations balances co-rotation by the flow. Since director rotations are driven by gradients in the velocity field, where $u^{||}$ varies along the normal coordinate, the magnitude of flow-driven alignment of the director field depends on the sign of $\nabla^2\zeta$.

In the case of $0 < \theta < \pi/2$ and considering $\nabla\zeta > 0$, the resulting shear flow rotates the director clockwise left of the maximum of $|\nabla\zeta|$, where $\nabla^2\zeta > 0$, and anti-clockwise to its right where $\nabla^2\zeta < 0$. Hence the director in the contractile domain points along the normal, parallel to the activity gradient $\mathbf{k}$, while in the extensile domain the director aligns tangentially, perpendicular to the activity gradient

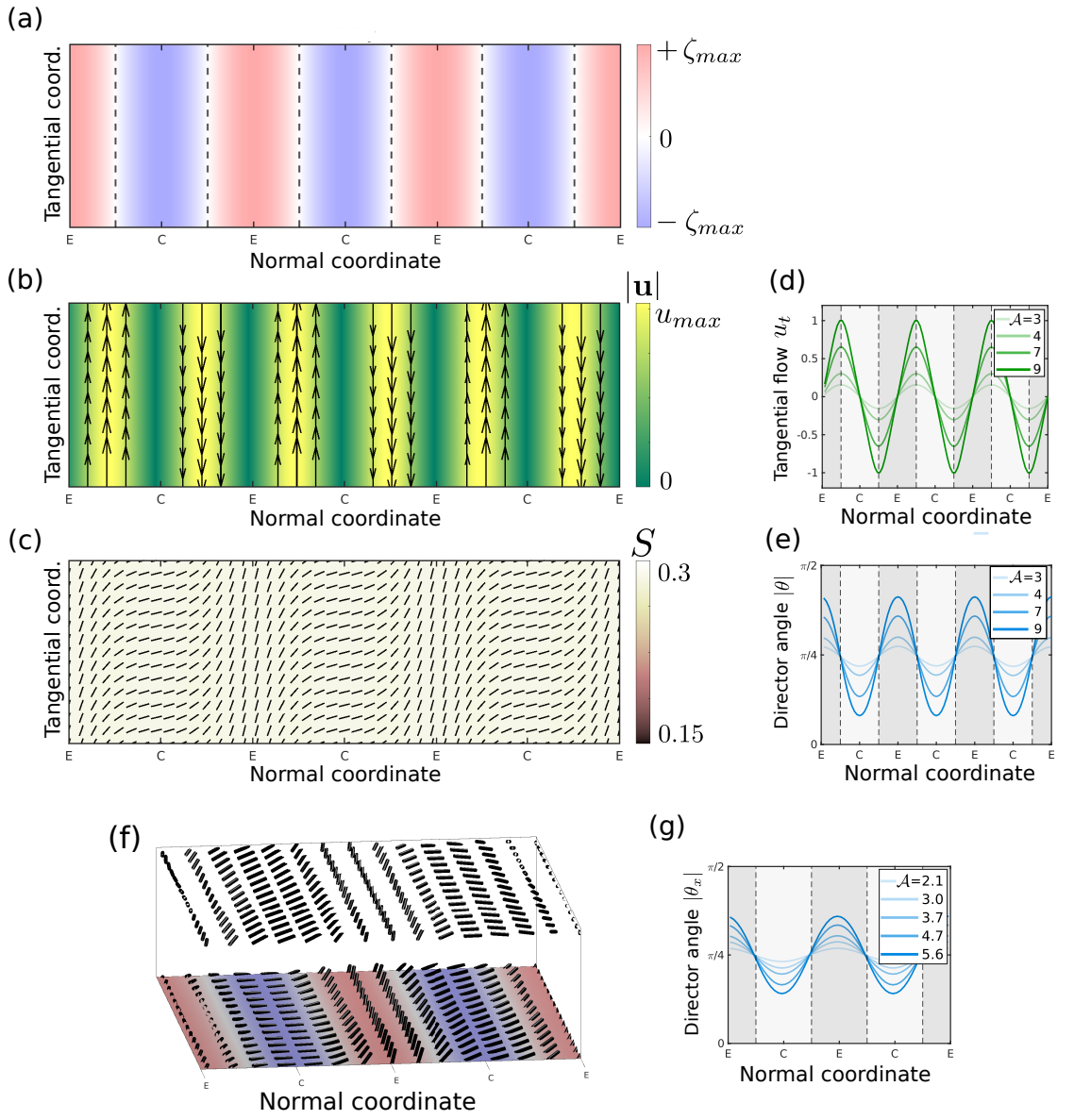


Figure 4.1: **(a)** Cosinusoidal variation of active stress along the normal direction. Extensile and contractile regions are labelled as E and C respectively. **(b)** Active flows form along the tangential direction in the transition regions where $\zeta \approx 0$. **(c)** Director field aligns tangential (normal) to the gradient direction $\mathbf{k}$ in extensile (contractile) regions. **(d,e)** Before the onset of active turbulence, the magnitude of flows and the degree of tangential (normal) alignment increases with activity number $\mathcal{A} = \lambda\sqrt{|\zeta_{max}|/K_{LC}}$. **(f,g)** Three-dimensional systems in which activity varies along one coordinate axis show the same quasi-two-dimensional behaviour. However, the director alignment in extensile regions is degenerate within the two-dimensional tangential plane.

(Fig. 4.1 c). The magnitude of nematic alignment depends on the relative strengths of the flow-induced rotation of the director field through the co-rotational term $\mathcal{W}$

and the relaxation of nematic distortions through the molecular field $\mathbf{H}$. Thus spatial variations of $|\theta|$ along the normal coordinate become larger for increasing activity ζ_{max} (faster flow) and decreasing elastic constant K_{LC} (slower relaxation) (Fig. 4.1 e).

The nematic alignment induced by active flows at points of large activity gradients therefore acts as an effective anchoring force, favouring normal anchoring on the contractile side ($\nabla^2\zeta > 0$) and tangential anchoring on the extensile side ($\nabla^2\zeta < 0$) of transition regions. We find that activity profiles which feature sharper interfaces between extensile and contractile domains do not qualitatively change the dynamics in the laminar regime and only slightly modify the shape of flow and director profiles (Fig. 4.4 a,b).

In 3D systems where activity varies along one of the coordinate axes, the director alignment with respect to the gradient direction $\mathbf{k}$ is quantified by the director angle $|\theta_x| = \cos^{-1}(\mathbf{k}\cdot\mathbf{n}/|\mathbf{k}|)$. As for the 2D case, the director field follows variations in activity and aligns normal to the activity gradient in contractile domains. In extensile domains, however, the tangential director orientation is degenerate and points along a random direction within the two-dimensional plane perpendicular to $\mathbf{k}$ (Fig. 4.1 f,g).

4.4 Active turbulence in 2D systems

4.4.1 Cross-over to active turbulence

We will now consider systems with large active stress ζ_{max}, where the soft confinement introduced by passive boundaries between extensile and contractile regions is too weak to prevent the system transitioning to active turbulence (Fig. 4.2 a,b). In 2D systems the transition occurs at a critical activity number $\mathcal{A} \gtrsim 10$, thus depending on the magnitude of active stress ζ_{max}, the elastic constant K_{LC} and the wavelength of the activity patterns (Fig. 4.2 c). Although topological defects and chaotic flow fields tend to destroy any nematic ordering, the time-averaged director field still shows some finite normal (tangential) alignment in contractile (extensile) domains in the turbulent state as shown by the time-averaged director angle $\langle|\theta|\rangle$ between director $\mathbf{n}$ and gradient axis (Fig. 4.2 d). The magnitude of alignment A_θ,

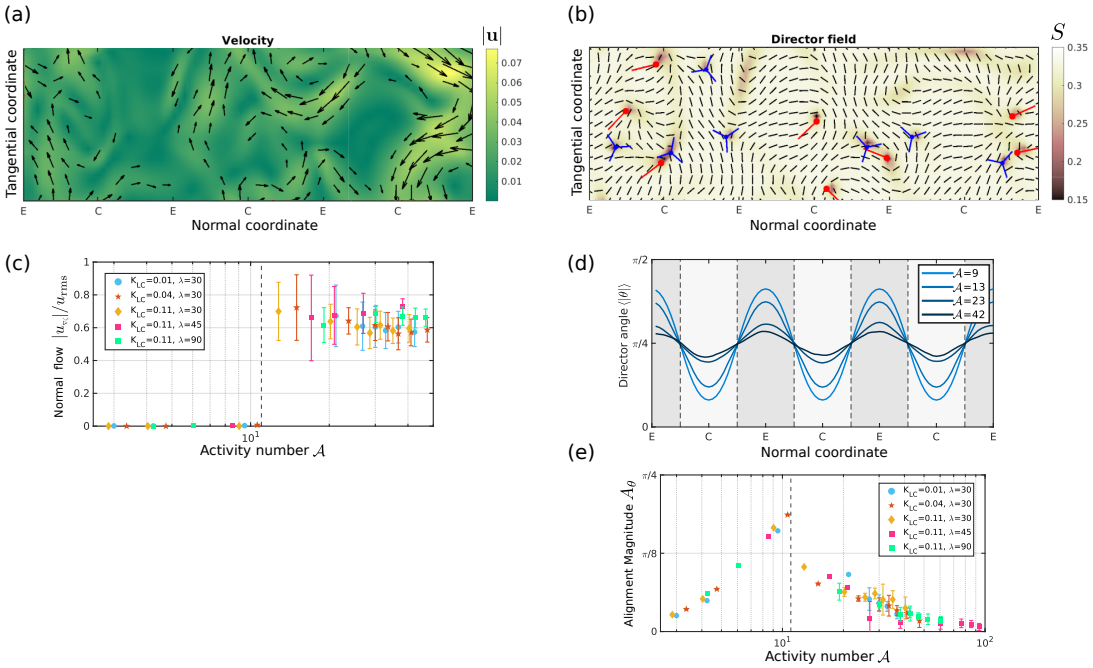


Figure 4.2: For sufficiently large activity, the system transitions into an active turbulent state, which is characterised by **(a)** chaotic flow fields and **(b)** motile topological defects. Comet-like $+1/2$ defects are self-propelled and are shown in red; trefoil-like $-1/2$ defects are only passively advected and are highlighted in blue. **(c)** The onset of active turbulence is characterised by chaotic flows with components along the normal coordinate, as indicated by a sharp increase of the average flow component along the normal coordinate $|u_{\nabla\zeta}|$ relative to the root-mean-squared velocity u_{rms} in the system. The critical activity ζ_{max} at which this transition occurs depends on the dimensionless activity number $\mathcal{A} = \lambda\sqrt{|\zeta_{max}|/K_{LC}} \sim 10$. **(d)** The average alignment of the director field in the turbulent regime decreases with $\mathcal{A}$ as shown by the time-averaged director angle $\langle|\theta|\rangle = \langle|\cos^{-1}(\mathbf{k}/|\mathbf{k}|\cdot\mathbf{n})|\rangle$. **(e)** The magnitude of alignment A_θ, which is defined as the amplitude of variations of $\langle|\theta|\rangle$ along the normal direction, increases monotonically with $\mathcal{A}$ in the laminar regime and decays with increasing activity in the turbulent regime. The mean director angle and normal flow component were calculated by averaging quantities over the tangential coordinate and over time $t = [0, 80000]$ (80 snapshots).

which is defined as the amplitude of variations of $\langle|\theta|\rangle$ along the normal direction, reaches a maximum at the onset of active turbulence and decays with increasing activity (Fig. 4.2 e). The director $\mathbf{n}$ eventually approaches a random distribution, $\theta \sim \mathcal{U}(-\pi/2, \pi/2)$, which yields $\langle|\theta|\rangle \to \pi/4$ throughout the system.

4.4.2 Polarization of $+1/2$ defects

In the active turbulent regime, both $\pm 1/2$ defects move in the background flow, but comet-shaped $+1/2$ defects are also self-motile, with their propulsion speed

being proportional to activity $|\zeta|$ [123]. Their propulsion direction $\mathbf{v}$ is parallel (anti-parallel) to the defect orientation vector $\mathbf{p} = \nabla \cdot \mathbf{Q}/|\nabla \cdot \mathbf{Q}|$ (which points from head to tail), in contractile (extensile) systems. Activity gradients across $+1/2$ defects give rise an active torque Γ_{act} which acts to align $+1/2$ defects parallel to activity gradients, $\mathbf{p} \propto \nabla\zeta$ (see Fig. C.1 a,b). On the other hand, the flow-driven normal (tangential) director field alignment in contractile (extensile) domains acts as a soft boundary condition on the director field $\mathbf{n}$. $+1/2$ defects which align anti-parallel to the activity gradient, $\mathbf{p} \propto -\nabla\zeta$, minimize distortions in $\mathbf{n}$, thus elastic forces create an elastic torque Γ_{el} which minimize the elastic energy of the system (Fig. C.1 c,d). The elastic torque Γ_{el} on $+1/2$ defects thus opposes the active torque Γ_{act} (Fig. 4.3 a). While the magnitude of active and elastic torques can be easily measured for single $+1/2$ defects subject to external activity gradients or nematic boundary conditions, it is not immediately clear which contribution dominates in the regime of active turbulence, where a finite alignment magnitude A_θ of the average director field $\langle|\theta|\rangle$ gives rise to soft boundary conditions and interactions between defects become important.

To investigate the behaviour of defects in the regime of active turbulence, we track the position and orientation $\mathbf{p}$ of $+1/2$ defects in the system. By considering active and elastic forces in the vicinity of defects, we can calculate the average elastic and active torques acting on $+1/2$ defects as a function of defect orientation (see appendix C.2 for further information and supplementary figures Fig. C.1 and Fig. C.2). By averaging over defects and time, we confirm that elastic torques indeed oppose active torques (Fig. 4.3 b). However, active torques remain the dominant contribution to the total torque $\Gamma = \Gamma_{el} + \Gamma_{act}$ in the regime of active turbulence (Fig. 4.3 c).

In order to quantify to which extent defects are locally polarized by active torques, we measure the angular distribution of defect orientations $\mathbf{p}$, averaging over time (Fig. 4.3 d). To quantify the orientational order of defects, we define the defect polarization $\mathcal{P} = \sqrt{\langle p_x\rangle^2 + \langle p_y\rangle^2}$, which is is zero if $+1/2$ defects are oriented randomly and equals one if the defects perfectly align along one direction. The polarization direction, $\langle\mathbf{p}\rangle$, is calculated as the circular mean of the distribution of

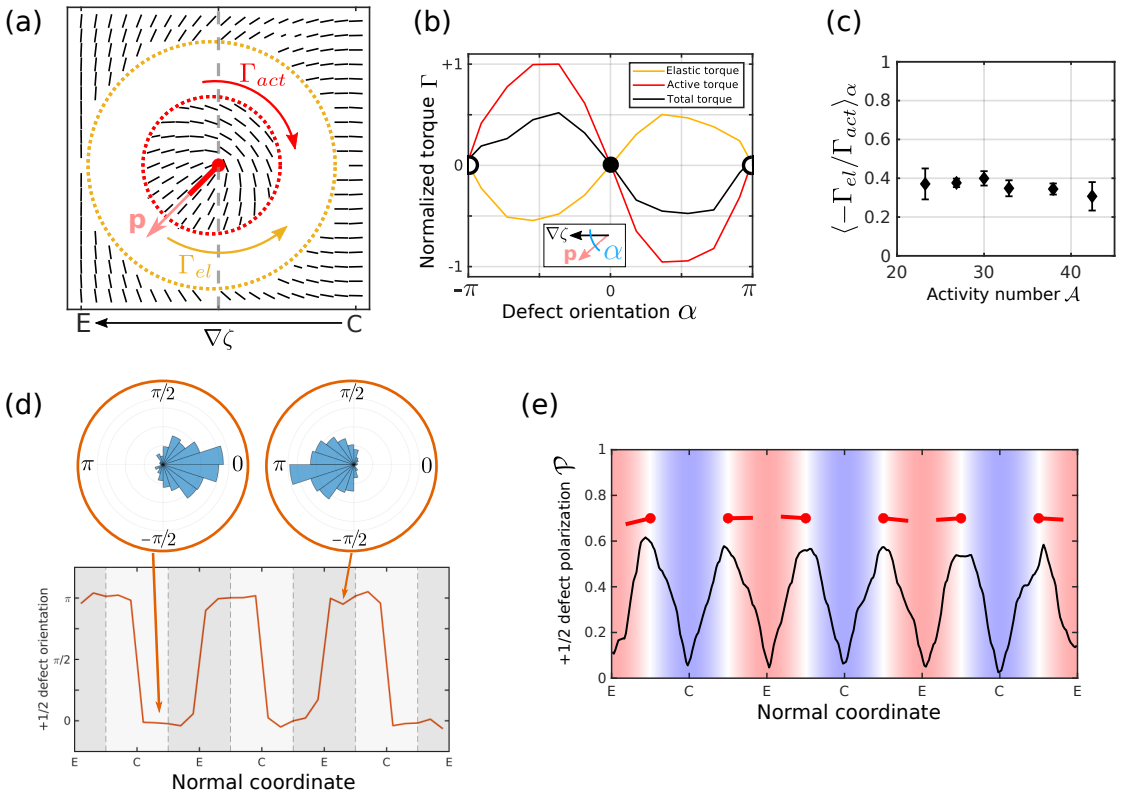


Figure 4.3: **(a)** $+1/2$ defects are subject to an elastic torque Γ_{el}, which tries to minimize the elastic energy of the system (orange), and an active torque Γ_{act}, which is caused by differential self-propulsion $\mathbf{v}$ across the defect (red). **(b)** Activity gradients create an active torque on $+1/2$ defects, which is strongest if the defect orientation $\mathbf{p}$ is perpendicular to the activity gradient $\nabla\zeta$ ($\alpha = \pm\pi/2$) and vanishes at $\alpha = 0, \pi$. Active torques align $+1/2$ defects parallel to activity gradients, which is evident from the stable fixed-point at $\alpha = 0$. Elastic torques, on the other hand, oppose active torques and favour $+1/2$ defects to align anti-parallel to activity gradients (see Fig. C.1 c,d). We find that the average torque on defects $\Gamma = \Gamma_{el} + \Gamma_{act}$ is dominated by active contributions in the regime of active turbulence. Average torques Γ_{act} and Γ_{el} were obtained by averaging over defects within an orientation window $[\alpha - \pi/12, \alpha + \pi/12]$. **(c)** The relative magnitude of active and elastic torques does not significantly change as function of activity number $\mathcal{A}$. Error bars show the mean and standard deviation of Γ_{el}/Γ_{act} when averaged over defect orientations α. **(d)** Defect polarization magnitude and direction are calculated based on the time-averaged distribution of defect orientations $\mathbf{p}$. **(e)** $+1/2$ defects are polarized at positions of large activity gradients between contractile and extensile domains with their tail pointing towards extensile domains. The fluctuations in polarization $\mathcal{P}$ are caused by the finite sample size of defect orientations. The defect polarization $\mathcal{P}$ as a function of normal coordinate x was obtained by averaging over defect orientations $\mathbf{p}$ in intervals $[x - \lambda/20, x + \lambda/20]$ along x and averaging over time $t = [0, 400000]$ (200 snapshots).

$\mathbf{p}$. Even though the motion of individual defects is highly chaotic in the regime of active turbulence, we find that $+1/2$ defects are strongly polarized at the boundaries between extensile and contractile domains (Fig. 4.3 e). The average defect orientation

aligns with and is proportional to the activity gradient, $\langle \mathbf{p} \rangle \propto \nabla\zeta$, in agreement with previous theoretical predictions which considered active torques on individual defects [118, 119]. A strong polarization of defects along activity gradients thus confirms once more that active torques on $+1/2$ defects are dominating elastic torques, $\Gamma_{act} > \Gamma_{el}$. It should be emphasised, however, that both torques originate from activity gradients since the nematic boundary condition giving rise to Γ_{el} is driven by active tangential flows.

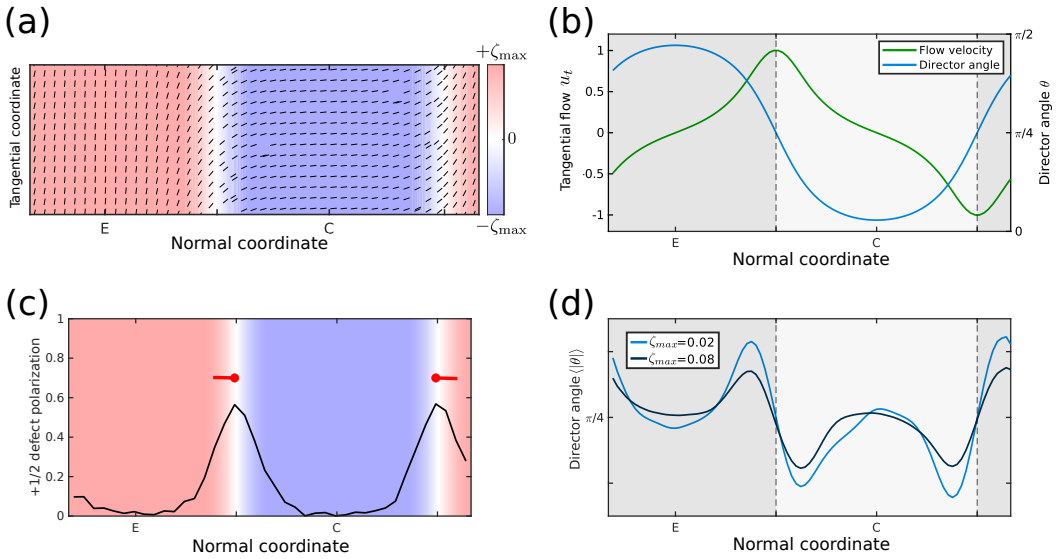


Figure 4.4: **(a)** Sharp activity interfaces in 2D systems give rise to qualitatively similar dynamics in the laminar regime as sinusoidal activity variations. **(b)** Tangential flows are more strongly confined to the interface giving rise to a slightly different director profile. **(c)** In the turbulent state $+1/2$ defects show strong polarization at interfaces, which vanishes in contractile and extensile bulk regions. **(d)** As expected for isotropic active turbulence, in bulk regions there is no average alignment of the director field , $\langle|\theta|\rangle = \pi/4$. Close to activity interfaces there is a finite average alignment, which decreases with increasing active stress ζ_{max}. For sharp activity interfaces active stress follows $\zeta(x) = \zeta_{max}$ for $0 \leq x \leq L/3$, $\zeta(x) = -\zeta_{max}$ for $L/2 \leq x \leq 5/6L$ and $\zeta(x) = \zeta_{max} \cdot \cos\left(\frac{6\pi}{L}x\right)$ otherwise.

In systems with sharp activity interfaces, non-zero defect polarization $\langle \mathbf{p} \rangle$ and average director alignment $\langle|\theta|\rangle$ are limited to boundaries and vanish in contractile and extensile bulk regions as expected for isotropic active turbulence (Fig. 4.4 c,d).

4.5 Active turbulence in 3D systems

4.5.1 Average director field alignment

We next consider 3D bulk systems in which activity varies along one direction (Fig. 4.5 a). The point defects of 2D nematics are replaced by disclination lines which can continuously transform from a local $-1/2$ configuration, in the plane perpendicular to the line tangent, into a $+1/2$ configuration through an intermediate twist defect, which is inherently three-dimensional. In 3D nematics both twist and $+1/2$ defects have a unique polar direction $\mathbf{p}$ in the plane perpendicular to the line tangent (Fig. 4.5 b). The flows and morphological dynamics of disclination lines in 3D active nematics are governed by the local director profile [36, 38]. As already pointed out in the previous chapter, disclination lines in purely extensile systems are predominantly twist-like, while contractile activity favours the creation of the wedge-like line segments with cross-sections that resemble $\pm 1/2$ defects. This behaviour is reflected by variations in the spatial density of $\pm 1/2$ and twist line segments across a system with extensile and contractile domains (Fig. 4.5 c).

In 3D active turbulence with homogeneous activity the average orientation of the director field $\mathbf{n}$ is, by symmetry, randomly distributed, $\cos\theta_x \sim \mathcal{U}(0,1)$, where θ_x is the angle between the director field and a random reference vector. Deviations from the average director angle $\langle\cos(\theta_x)\rangle = 1/2$ thus indicate that the time-averaged director field is either biased towards parallel ($\langle\cos\theta_x\rangle > 1/2$) or perpendicular alignment ($\langle\cos\theta_x\rangle < 1/2$) with respect to the reference vector. For 3D active turbulence with heterogeneous activity we find that the time-averaged director field is aligned normal (tangential) with respect to the activity gradient in contractile (extensile) domains, as for 2D systems (Fig. 4.5 d). The nematic alignment in 3D systems can be quantified by A_θ, the amplitude of variations of $\langle\cos(\theta_x)\rangle$ along the normal direction. To compare the variation of the alignment magnitude with activity in 2D ($A_\theta \in [0, \pi/4]$) and 3D systems ($A_\theta \in [0, 0.5]$), we normalize A_θ with respect to A_θ^{max}, the maximum alignment realized just before the onset of active turbulence. We find that with increasing activity, the average

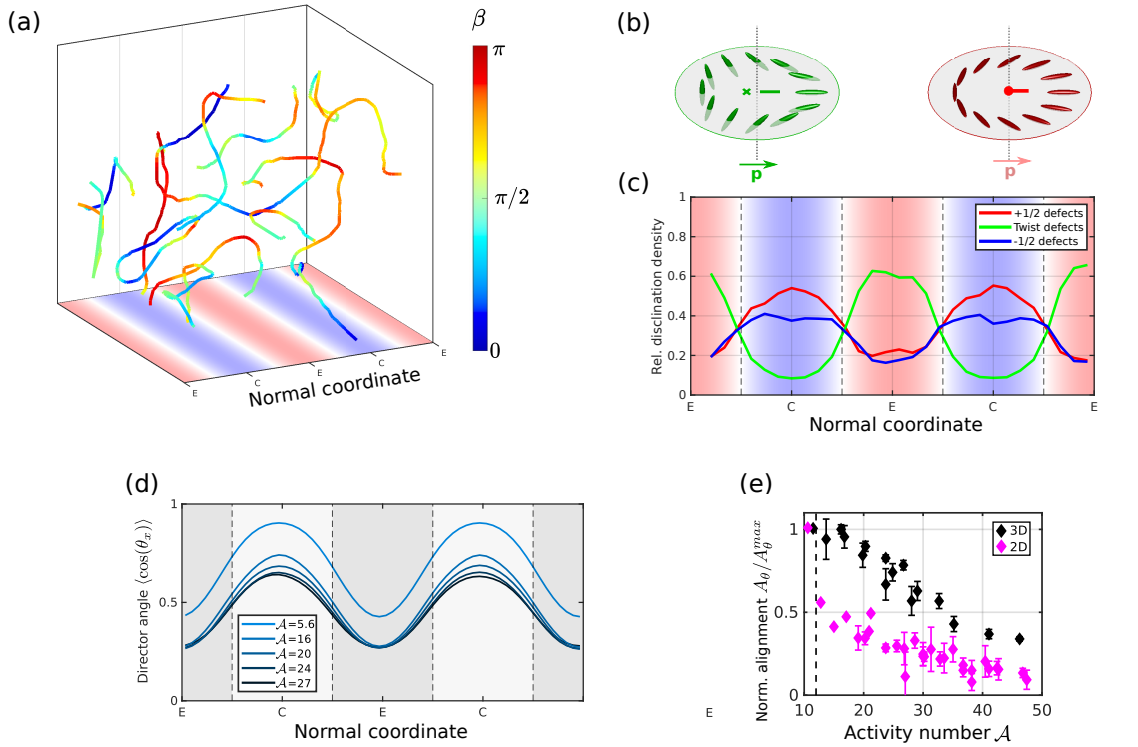


Figure 4.5: **(a)** Three-dimensional active turbulence is characterised by motile disclination lines which form closed loops or span the entire system as open lines. **(b)** Disclination lines can be locally classified by a continuous twist-angle $0 < \beta < \pi$ (see chapter 2.2.3). Both $+1/2$ defects ($\beta \approx \pi$) and twist defects ($\beta \approx \pi/2$) have a unique polar direction $\mathbf{p}$ in the plane perpendicular to the disclination line tangent. **(c)** The relative density of $\pm 1/2$ and twist segments depends on the type of activity (extensile/contractile) and follows spatial variations in active stress (fluctuations are caused by finite sample size). **(d)** The director field alignment in 3D systems in the turbulent regime decays with $\mathcal{A} = \lambda\sqrt{|\zeta_{max}|/K_{LC}}$, as shown by the time-averaged director angle $\langle\cos(\theta_x)\rangle$. **(e)** As for 2D systems, the magnitude of alignment A_θ, which in 3D is defined as the amplitude of variations of $\langle\cos(\theta_x)\rangle$ along the normal direction, decays with increasing activity number $\mathcal{A}$. Black diamonds show A_θ/A_θ^{max} as a function of ζ_{max} for different parameters $K_{LC} = [0.04, 0.08, 0.12, 0.2]$, where A_θ^{max} is the maximum alignment realized just before the onset of active turbulence (dashed line). Pink diamonds show normalized data taken from Fig. 4.2 e. The mean director angle and disclination line densities were calculated by averaging quantities over both tangential coordinates and time $t = [0, 500000]$ (250 snapshots).

alignment of the director field in 3D decays much more slowly compared to 2D systems, where A_θ sharply drops at the onset of active turbulence (Fig. 4.5 e).

4.5.2 Polarization of disclination lines

To gain further insight into the dynamics of disclination lines in the presence of activity gradients, we measure the angle γ_x between disclination line segments and the gradient direction $\mathbf{k}$. We find that disclination lines are preferentially oriented perpendicular to activity gradients, $\gamma_x \approx \pi/2$ (Fig. 4.6 a). This preferred alignment is caused by active torques Γ_γ on line segments when they lie along activity gradients (Fig. 4.6 b). This implies that the orientation of the defect structures in the plane perpendicular to line segments can be either parallel ($\mathbf{p} \propto \nabla\zeta$), anti-parallel ($\mathbf{p} \propto -\nabla\zeta$) or perpendicular ($\mathbf{p} \cdot \nabla\zeta = 0$) to the activity gradient.

We define the polarization order parameter for disclination lines as $\mathcal{P} = \sqrt{\langle p_x\rangle^2 + \langle p_y\rangle^2 + \langle p_z\rangle^2}$, which is is zero if defects are oriented randomly and equals one if the defects perfectly align along one direction. The polarization order parameter $\mathcal{P}$ and direction of $+1/2$ and twist segments are shown in Fig. 4.6 c and Fig. 4.6 d, respectively. While $+1/2$ disclination are polarized parallel to activity gradients, $\langle\mathbf{p}\rangle \propto \nabla\zeta$, like in 2D systems, twist disclinations are polarized anti-parallel to the activity gradient $\langle\mathbf{p}\rangle \propto -\nabla\zeta$.

We argue that this is caused by a different balance between elastic torques Γ_{el} and active torques Γ_{act} on different defect types. While active torques Γ_{act} dominate elastic torques Γ_{el} for $+1/2$ disclinations (see Fig. 4.3 b), active forces around twist disclinations feature out-of-plane components, yielding an active torque which does not align with the line tangent (see Fig. C.2). Thus the orientation $\mathbf{p}$ of twist defects is less affected by active torques than the orientation of $+1/2$ defects (Fig. C.2 c), causing twist defects to align in a way which minimizes the elastic energy of the system. Indeed, since active torque is generated by differential velocities across defects, we would expect a smaller active torque on twist defects because they have a lower self-propulsion speed than $+1/2$ defects [36].

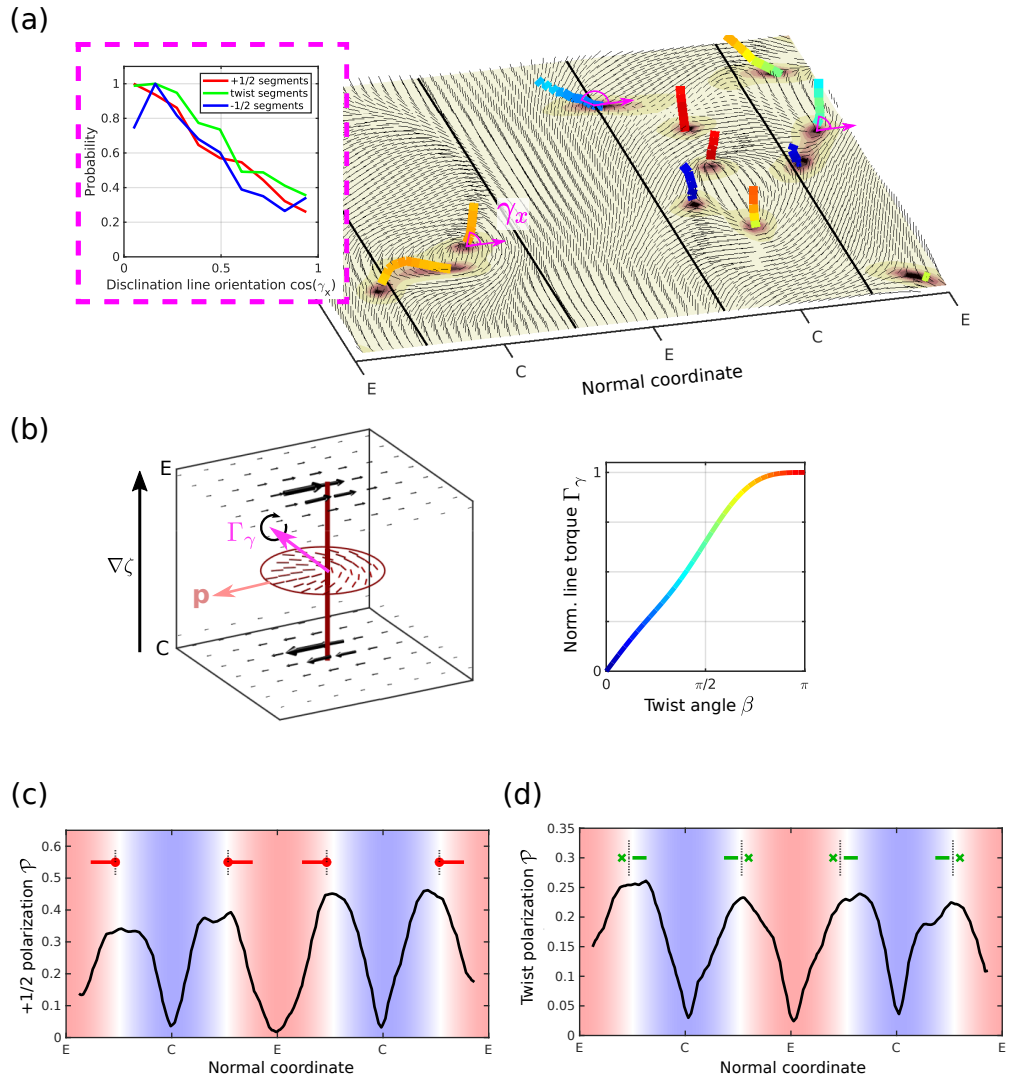


Figure 4.6: **(a)** The angle γ_x between disclination line segments and the normal axis along which activity varies is measured for all disclination lines in the system. The time-averaged distribution of $|\cos(\gamma_x)|$ shows that disclination line segments preferentially point perpendicular to activity gradients ($\gamma_x = \pi/2$), independent of twist-angle β. The distribution of orientation γ_x was obtained by averaging over all disclination line segments and time $t = [0, 500000]$. **(b)** When a $+1/2$ disclination line points along an activity gradients $\nabla\zeta$ ($\gamma_x = 0$), active forces (black arrows) create a torque Γ_γ (pink arrow), which re-orients the disclination line perpendicular the gradient direction ($\gamma_x = \pi/2$). The magnitude of the line torque Γ_γ depends on the self-propulsion speed of the disclination type, thus it is strongest for $+1/2$ line segments and vanishes for $-1/2$ segments. Since disclination line segments of different types β are connected with each other, line torques Γ_γ acting on $+1/2$ and twist segments also align passive $-1/2$ segments. **(c)** As in 2D systems, active torques align the orientation $\mathbf{p}$ of $+1/2$ defects parallel to activity gradients $\nabla\zeta$, causing a large polarization of $+1/2$ disclinations ($\beta \in [7\pi/8, \pi]$) at points of large activity gradients. **(d)** Twist disclinations ($\beta \in [3\pi/8, 5\pi/8]$) are dominated by elastic torque rather than active torque, thus they are polarized anti-parallel to activity gradients. The fluctuations in polarization $\mathcal{P}$ are caused by the finite sample size of $+1/2$ and twist defect orientations. The polarization $\mathcal{P}$ of disclination lines was calculated by averaging over defect orientations $\mathbf{p}$ in intervals $[x - \lambda/20, x + \lambda/20]$ along the normal coordinate x and averaging over time $t = [0, 500000]$ (250 snapshots).

4.6 Summary and Discussion

In this chapter we have investigated how two- and three-dimensional active nematic bulk systems respond to one-dimensional spatial variations of active stress. We have shown that, in the absence of defects, activity gradients induce an effective anchoring force which aligns the director field along the normal direction in contractile domains and tangentially in extensile domains. In line with recent analytical work [119, 120], we found that the orientation of motile $+1/2$ defects in 2D active turbulence are dominated by active torques and polarized parallel to activity gradients, $\mathbf{p} \propto \nabla\zeta$. Since the director field in the vicinity of polarized $+1/2$ defects opposes the director alignment set up by active flows perpendicular to activity gradients, the average alignment of the director field in 2D active turbulence remains weak.

In 3D systems we find that disclination line segments are oriented perpendicular to activity gradients, thereby allowing the orientation of the defect structures in the plane perpendicular to line segments to point parallel, anti-parallel or perpendicular to activity gradients. Like in 2D systems, active torque robustly aligns $+1/2$ disclination lines parallel to activity gradients, even in the turbulent regime. In contrast, the alignment of twist disclinations is dominated by elastic interactions rather than active torques, causing them to be polarized anti-parallel to activity gradients. Thereby the director field in the vicinity of twist defects matches with the alignment set up by active flows in the plane perpendicular to activity gradients and the average alignment of the director field decays more slowly with activity number $\mathcal{A}$ than in 2D systems. Deriving exact expressions for the elastic torque on disclination line segments in the turbulent regime remains challenging since the local torque on line segments depends not only on the nematic boundary conditions in the plane perpendicular to the line segment, but also on elastic forces acting along disclination lines and their local curvature.

We note that the alignment of the director field and defects due to active force gradients is not unique to bulk systems. As demonstrated chapter 3, isotropic-nematic interfaces ($\nabla S > 0$) can also generate active flows which align the director field perpendicular or planar to the interface in contractile and extensile systems,

respectively [84]. This polarizes the orientation of $+1/2$ defects close to interfaces, which has also been observed in growing bacterial biofilms [29, 64].

Experiments with spatially structured activity have been realised by combining actin filaments with light-activated gear-shifting myosin motors, where light locally induces extensile active stress in an otherwise passive fluid [118]. Extending the concept of light-modulated activity to contractile systems, it might be possible to create artificial systems with distinct extensile and contractile domains in the future by selectively activating molecular motors mediating either extensile or contractile stress. Spatial variations of active stress are also ubiquitous in biological systems, ranging from structure formation during embryonic development driven by a heterogeneous distribution of myosin motors [106, 124, 125] to flows and deformations of cell aggregates, such as tumours, caused by differential cell growth and death as a consequence of limited access to nutrients in the core of the aggregate [16, 43, 126, 127]. The latter is, in fact, the subject of the next chapter.

Take-home message:

Gradients in active stress ζ can polarize the orientation of defects and create either parallel or perpendicular director alignment with respect to the gradient direction, depending on the sign of $\nabla^2\zeta$.

5

Application I: Proliferating multicellular spheroids

In the previous chapter, we focused on exploring the generic implications of activity gradients in bulk active nematic systems. Now we are shifting our attention towards how active nematic theory can be applied to biological systems in more detail. In this chapter we will study cell flows and tissue dynamics inside multicellular spheroids, spherical, self-assembled aggregates of cells that are widely used as model systems to study tumour dynamics. Cells near the surface of spheroids have better access to nutrients and therefore proliferate more rapidly than those in the resource-depleted core. Using both analytical arguments and three-dimensional simulations, we find that the proliferation gradients result in flows and activity gradients, both of which can align the orientation axis of cells inside the aggregates. Depending on intrinsic tissue parameters, we identify three distinct alignment regimes: (i) Radial or (ii) angular cell alignment throughout the aggregate and (iii) angular cell alignment close to the surface and radial alignment in the core. The continuum description of tissue dynamics inside spheroids not only allows us to infer dynamic cell parameters from experimentally measured cell alignment profiles, but more generally motivates novel mechanisms for controlling the alignment of cells within aggregates which has been shown to influence the mechanical properties and invasive capabilities of tumours.

5.1 Introduction

Many biological systems such as epithelial tissues, bacterial colonies or three-dimensional organoids are active systems; they continuously consume chemical energy from their environment to perform tasks such as growth or migration, both of which involve the generation of mechanical stresses by the cells through a variety of biochemical processes [128–130]. A prominent 3D example of an active tissue is multicellular spheroids. These are spherical, self-assembled aggregates of cells which provide important model systems for investigating the behaviour of 3D cell aggregates, for example, the effects of mechanical stress, or for screening of anti-cancer drugs.

Multicellular spheroids are typically studied in a suitable environment which provides cells with all the needed metabolites such as oxygen and nutrients. The metabolite concentration within cellular aggregates therefore normally decreases towards the core since the supply of metabolites in spheroids and avascular tumours is limited by diffusive transport from the surface. While cells close to the surface show a high rate of cell division, cells located close to the core do not have sufficient access to metabolites and die, thereby forming a necrotic core [126, 131]. Hence the outer shell of spheroids is dominated by cell growth while the core is dominated by cell death. This has two consequences. The first is that a radial flow of cells is set up from the surface to the centre of the spheroid. The second is a gradient of activity which is a consequence of the gradient in the number of cell divisions which locally generate active, extensile, dipolar forces along their division axes.

In this chapter we study the competition between these effects to describe the flow and orientation of cells in dense multicellular aggregates. We start in section 5.2 by presenting the equations of motion for the metabolite concentration inside spheroids and describe how cell proliferation is incorporated into a continuum model. In section 5.3 we outline the simulation methods and present a parameter mapping between simulation parameters and experimental values.

The main results are presented in sections 5.4-5.7. In the first part 5.4, we show that radial cell flows created by gradients in the isotropic cell growth rate give

rise to radial cell elongation profiles inside multicellular spheroids, where cells are aligned either radially or circumferentially (tangentially) throughout the aggregate. In the second part 5.5, we investigate how anisotropic active forces produced by cell division and death affect the cell orientation and flows inside spheroids. We highlight that gradients in active stress give rise to an effective cell anchoring at the surface and in the bulk, and the emergence of chaotic cell flows in the aggregate if active stress is sufficiently large. We then show, in part 5.6, that the interplay between growth driven flow and anisotropic stress can give rise to a variety of cell alignment profiles in proliferating spheroids. We subsequently demonstrate in section 5.7, that our theory allows us to estimate mechanical and dynamical tissue parameters directly from experimental measurements of the distribution of cell orientations inside freely grown spheroids. Finally, in section 5.8, we summarise the key results.

5.2 Governing equations

We consider a multicellular spheroid embedded in an environment with a fixed concentration m_0 of metabolites, such as oxygen, glucose or growth factors, which are necessary for cell proliferation. We assume that metabolites freely diffuse throughout tissue with diffusion constant D_m and are consumed by cells at a rate proportional to $\alpha^\star$. In the diffusive limit (Péclet number $Pe \ll 1$), the time evolution of metabolite concentration $m(\mathbf{x}, t)$ across tissues is governed by the reaction–diffusion equation

$$\partial_t m = D_m \nabla^2 m - \alpha^\star \varphi \, m \,, \tag{5.1}$$

where $\varphi(\mathbf{x}, t)$ is the cell-number density and ∇^2 is the Laplace operator. After an initial growth phase, multicellular spheroids reach a steady state at a finite radius R_c in which cell division near the outer shell exactly balances cell death close to the core. At steady-state, the cell density inside multicellular spheroids is homogeneous [43–45], so we may write $\varphi(\mathbf{x}, t) = \varphi_0$ and define $\alpha = \alpha^\star \varphi_0$ as a constant metabolite consumption rate throughout the aggregate. Since metabolites diffuse much faster

than the time scale of cellular rearrangements in tissues or aggregate deformations, the metabolite concentration is always at steady-state and eqn. 5.1 simplifies to

$$\nabla^2 m = (\alpha/D_m)m \,. \tag{5.2}$$

Thus $m(\mathbf{x})$ decreases towards the core of spheroids with a characteristic penetration length $\ell_m = \sqrt{D_m/\alpha}$.

As before, we describe the motion of cells inside spheroids in a continuum limit, where tissue is characterised by a cell-velocity field $\mathbf{u}$ and the $\mathbf{Q}$-tensor, which describes the magnitude and direction of cell alignment. Since the cell density stays constant throughout steady-state spheroids, every cell on average has the same volume. Whenever a cell in the tissue is dividing, it is replaced by two daughter cells which take up twice the volume of the mother cell. The additional volume is created by pushing neighbouring cells outwards, which gives rise to a divergence in the cell velocity field. Thus the cell flow $\mathbf{u}$ follows the continuity equation of an incompressible fluid but with an additional source term

$$\nabla \cdot \mathbf{u} = k_p^\star \,, \tag{5.3}$$

where the net cell production rate $k_p^\star(\mathbf{x}, t) = k_+ - k_-$ depends on the local reproduction rate k_+ or death rate k_- of individual cells. When cells have access to sufficient metabolites, cell division dominates, $k_p^\star > 0$, which acts as a mass source causing diverging local flow. On the other hand, when the metabolite concentration falls below a certain threshold, $m < m_c$, cells die faster than they divide, $k_p^\star < 0$, thus creating a mass sink and locally converging flow. In the vicinity of the homeostatic equilibrium, $m = m_c$, we expand the cell production rate $k_p^\star$ rate around the homeostatic metabolite concentration to linear order,

$$k_p^\star = k_p \, (m - m_c) \;, \tag{5.4}$$

where the parameter k_p is a proportionality constant. In addition to the continuity equation 5.3, the cell flow $\mathbf{u}$ in tissues follows the Navier-Stokes-equations 2.2. Unlike for 2D cell-monolayers, where friction between cells and the underlying

substrate gives rise to a friction term in eqn. 2.2, for 3D spheroids we assume that cell-cell friction is dominating and that friction forces at the boundary of freely grown aggregates are negligible. Every division and death event in a tissue generates anisotropic dipolar forces. Assuming that active stresses due to cell division and death are on average aligned with the local tissue anisotropy $\mathbf{Q}$, the active stress due to cell division and cell death is [77, 132]

$$\Pi_{act} = -\zeta^\star \mathbf{Q} \,, \tag{5.5}$$

where $\zeta^\star(\mathbf{x}, t)$ is the magnitude of active stress. Each cell division produces extensile anisotropic stress, $\zeta_+ > 0$, where forces are directed outwards along cell axis $\mathbf{n}$ and inwards along the two perpendicular axes. The force direction is reversed for cell death events, which produce contractile stress, $\zeta_- < 0$. For simplicity we assume $\zeta_+ = |\zeta_-|$, hence the magnitude of active stress follows variations in cell production rate,

$$\zeta^\star = \zeta \left(m - m_c\right) \,, \tag{5.6}$$

where ζ quantifies the local, time-averaged magnitude of active stress induced by cell division or death. Note that, for simplicity, we have neglected the intrinsic active stress produced by cells even in the absence of cell division or death, which can be either extensile or contractile, depending on cell type [30, 33, 102].

5.3 Simulation method

Like in chapter 3, we describe spheroids by using a continuous field φ with a free energy eqn. 2.5 which drives phase separation into two stable phases $\varphi = 0, 1$. The inside ($\varphi = 1$) and outside ($\varphi = 0$) of spheroids are separated by an interface of width $L \sim \sqrt{K_\varphi / A_\varphi}$ which introduces a surface tension $\gamma \sim \sqrt{A_\varphi K_\varphi}$. Parameters A_φ and K_φ are chosen to match the surface tension γ measured in experiments, while ensuring that the interface width is much smaller than any other length-scale in the system, $L \ll \min[\ell_a, \ell_m]$. In this chapter we will neglect the bending rigidity of the interface since in many experimental conditions surface tension dominates

and spheroids stay nearly spherical. Since spheroids are embedded in a passive and isotropic fluid, both the net cell production rate and active stress in simulations follow $k_p^{LB} = \varphi\, k_p$ and $\zeta^{LB} = \varphi\, \zeta$, respectively. To couple the nematic order $\mathbf{Q}$ to φ, again we use the liquid crystal bulk free energy eqn. 2.13.

We simulate growing spheroids by numerically solving the continuum equations of motion eqn. 5.2 for the metabolite concentration and eqns. 5.3, 2.2, 2.18 for the tissue dynamics, on a three-dimensional grid of size $84 \times 84 \times 84$ using the hybrid lattice Boltzmann-finite difference method. Analytical solutions for the flow field $\mathbf{u}$ and metabolite concentration m in spherical aggregates are presented in section 5.4. Throughout this chapter we use the following simulation parameters, in lattice-units, unless otherwise stated: $\rho = 1$, $\eta = 2/3$, $A_\varphi = 0.2$, $K_\varphi = 0.4$, $\Gamma_\varphi = 0.2$, $A_{LC} = 1.5$, $K_{LC} = 0.03$, $\Gamma_{LC} = 0.1$. To highlight the effects of flow-induced elongation of isotropic cells in section 5.4, we chose $\bar{\eta} = 2.55 + 0.1\varphi$ which yields an isotropic tissue $S_0 = 0$ inside spheroids unless flows drive nematic order for $\xi \neq 0$. In sections 5.5-5.7, we chose $\bar{\eta} = 2.7 + 0.3(\varphi - 0.5)$ which creates nematic order $S_0 = 0.3$ of constant magnitude inside aggregates.

5.3.1 Mapping of simulation parameters to experimental values

Like in chapter 3, we use three independent physical reference scales to map the dimensionless simulation parameters to physical units. To model multicellular spheroids, we use the aggregate size R, elastic constant K_{LC} and tissue viscosity η as reference scales (see Table 5.1). We chose the lattice spacing such that the diameter of spheroids is about 60 lattice sites, $\Delta x \approx 0.03\, R \approx 300 \mu m$. As before, we can obtain the elastic constant by using $K_{LC} \sim E \cdot L^2$, where E is the cells' Young's modulus and L is the cell size. The typical size and Young's modulus of colon and breast cancer cell lines, which are often used in spheroid experiments, are on the order of $L \sim 10\, \mu m$ and $E \sim 100\, Pa$ [133–135], respectively, which yields $K_{LC} \sim 10^{-8} N$. Finally we use $\eta \approx 60\, kPa\, s$ as the apparent viscosity of cell aggregates [87, 88].

Parameter	Simulation units	Physical units
Aggregate size R	30	$300\,\mu m$
Elastic constant K_{LC}	0.03	$5 \cdot 10^{-8}\,N$
Viscosity η	2/3	$60\,kPa\,s$
Lattice spacing Δx	1	$10\,\mu m$
Time step Δt	1	$15\,s$
Critical concentration m_c	0.8	0.8
Penetration length ℓ_M	12	$150\,\mu m$
Growth rate k_p	$8 \cdot 10^{-4}$	$5 \cdot 10^{-5}\,s^{-1}$
Active stress ζ	$0.005 - 0.04$	$30 - 240\,Pa$
Surface tension γ	0.3	$4 \cdot 10^{-2}\,N/m$
Spheroid bulk energy A_φ	0.2	$2.4\,kPa$
Nematic bulk energy A_{LC}	1.5	$18\,kPa$
Rotational diffusivity Γ_{LC}	0.1	$6 \cdot 10^{-7}\,(Pa\,s)^{-1}$
Mobility Γ_φ	0.2	$8 \cdot 10^{-16}\,m^2/Pa\,s$

Table 5.1: Mapping of Lattice-Boltzmann parameters to physical units using the spheroid radius R, the bending rigidity of cells K_{LC} and the tissue viscosity η as physical reference scales.

5.4 Growth-induced converging cell flows

We start by analytically solving the equations of motion eqns. 5.2, 5.3, 2.18 for the metabolite concentration m, cell flow $\mathbf{u}$ and nematic tensor $\mathbf{Q}$ for spherical aggregates in which active dipolar stress produced by cell division and cell death is negligible, $\zeta = 0$. In this case, the cell flows are caused solely by mass sources and sinks which arise as a consequence of the cell production rate $k_p^\star$. Solving eqn. 5.2 for the boundary condition $m = m_0 = 1$ at the surface yields a metabolite concentration $m(r)$ which is a function of the radial coordinate only,

$$m(r) = \frac{R}{r}\frac{\sinh(r/\ell_m)}{\sinh(R/\ell_m)}\,, \tag{5.7}$$

where R is the radius of the spheroid and ℓ_m is the characteristic penetration length of metabolites from the surface (Fig. 5.1 a,b). If the initial spheroid size is small, $R \lesssim \ell_m$, the total cell production rate is positive and the aggregate grows at a rate

$$\dot{R} = k_p \ell_m \left[\coth(R/\ell_m) - \frac{\ell_m}{R} - \frac{m_c R}{3\ell_m}\right]\,. \tag{5.8}$$

As less metabolites reach the core of larger aggregates, spheroids eventually reach a steady state $\dot{R} \to 0$ at a finite size $R = R_c$. At steady-state, the dimensionless

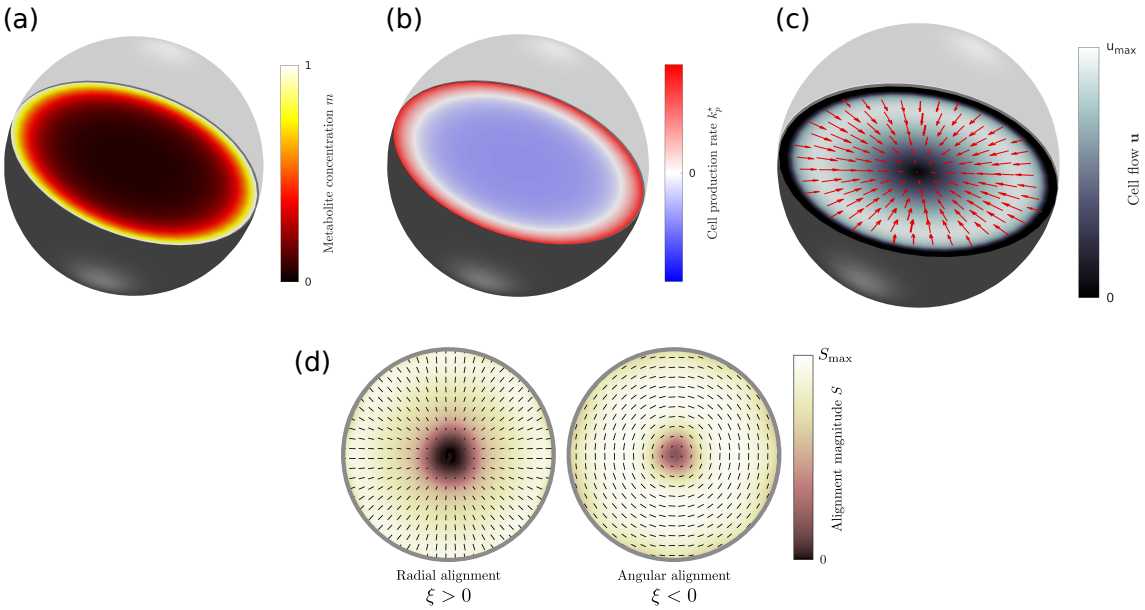


Figure 5.1: **(a)** Diffusion limited transport of metabolites give rise to radial concentration profiles $m(r)$ which decrease towards the core of spheroids. **(b)** Assuming the cell proliferation and cell death rates are proportional to the local metabolite concentration, the cell production rate $k_p^\star$ at steady-state is positive close to the surface and negative in the core, where the transition point $k_p^\star = 0$ depends on the critical metabolite concentration m_c. **(c)** In the absence of active dipolar stress spatial variations in the cell production rate create converging flow profiles given by eqn. 5.9. **(d)** Isotropic cells inside proliferating spheroids are radially elongated by converging flows for alignment parameter $\xi > 0$ and align tangential to the surface for $\xi < 0$. Since the magnitude of flow-induced elongation increases along the radial direction, cells close to the surface are more elongated than cells in the centre.

radius $\tilde{R}_c = R_c/\ell_m$ is a function of the critical metabolite concentration only, $\tilde{R}_c = f^{-1}(m_c)$, where $f(x) = 3(x \coth x - 1)/x^2$ (Fig. 5.2 a). Fig. 5.2 b,c shows how m_c affects the shape of the metabolite profile $m(r)$ which determines the cell production rate $k_p^\star$ inside aggregates of size $R = R_c$.

The cell flow $\mathbf{u} = u_r(r)\hat{\mathbf{r}}$ can be obtained by solving the continuity equation 5.3 in the domain $r \in [0, R]$ using the boundary condition $\mathbf{u}(R) = \dot{R}$,

$$u_r = k_p R \left[\frac{1}{\tilde{r}} \frac{\cosh \tilde{r}}{\sinh \tilde{R}} - \frac{1}{\tilde{r}^2} \frac{\sinh \tilde{r}}{\sinh \tilde{R}} - \frac{m_c r}{3R} \right] , \tag{5.9}$$

where $\tilde{R} = R/\ell_m$ and $\tilde{r} = r/\ell_m$. Since $\dot{R} > 0$ in growing spheroids, there is a transition between a diverging cell flow close to the surface, $u_r > 0$, and a converging cell flow $u_r < 0$ in the core of aggregates (Fig. 5.2 e). At steady-state, cell flows are facing inwards everywhere and vanish at the surface, $u_r(R_c) = 0$ (Fig. 5.1 c),

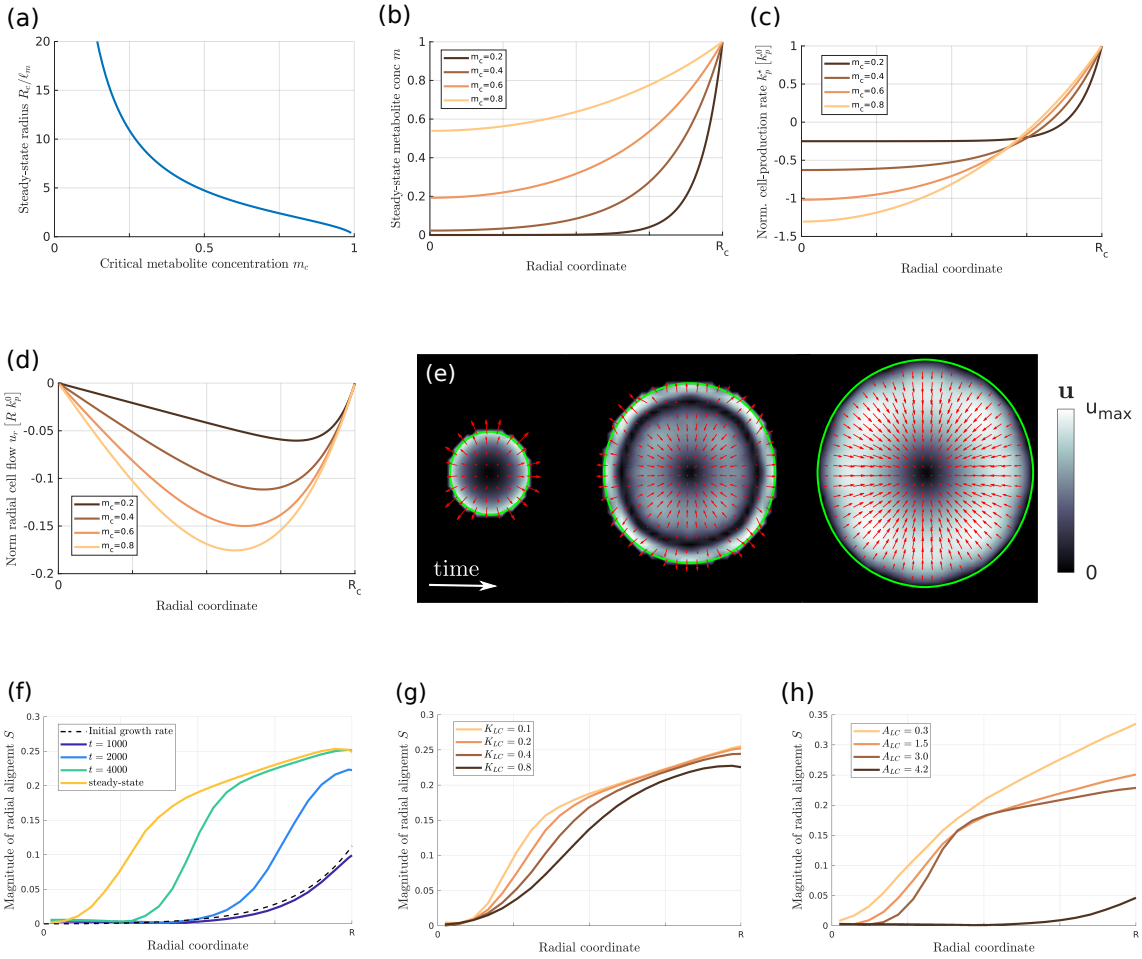


Figure 5.2: **(a)** Steady-state radius R_c/ℓ_m as a function of critical metabolite concentration m_c. **(b-d)** In steady-state spheroids the critical concentration m_c controls the shape of the radial metabolite profile m (panel b), cell production profile $k_p^\star$ (panel c) and flow profile u_r (panel d). **(e)** Snapshots showing the time evolution of the velocity field $\mathbf{u}$ inside a growing cell aggregate ($\zeta = 0$). At early times the spheroid is in a growing state $\dot{R} > 0$ because sufficient metabolites are available throughout the aggregate, $m(r) > m_c$, creating diverging cell flows $u_r > 0$. As the aggregate size increases, cells in the core will eventually have insufficient access to metabolites, $m(r = 0) < m_c$, resulting in converging cell flows $u_r < 0$ towards the centre. Spheroids will finally reach a steady state in which cell division and death exactly balance, $\dot{R} = 0$, leading to $u_r < 0$ throughout the aggregate. Snapshots show the cross-section at the equator of a growing spheroid defined by a concentration field φ, where the boundary of the aggregate is marked by the contour $\varphi = 0.5$ (green line). **(f)** Time-evolution of the radial cell alignment $Q_{rr} \sim S$ in numerical simulations initialized as $S = 0$ with $\xi > 0$. Initially, S follows the linear growth rate shown by eqn. 5.11 (black, dashed line). At late times, however, non-linear contributions arising from advection and the molecular field $\mathbf{H}$ balance the growth rate and S reaches a steady-state profile (yellow line). **(g,h)** Numerical cell alignment profiles at steady-state for different values of cell parameters A_{LC} and K_{LC}. Simulations were performed with spheroids of size $R = 30$ using isotropic cells ($S_0 = 0$) and $k_p = 0.001$, $\xi = 0.3$.

and the shape of flow profiles depends on the critical metabolite concentration m_c (Fig. 5.2 d). Recently it has been reported that shear stresses created by cell flow u_r can create a viscocapillary instability that perturbs the spherical symmetry of aggregates for sufficiently small surface tension [136]. In this work, however, we consider the limit in which cell-generated stress is small compared to the surface tension of spheroids and the shape of cell aggregates remains spherical.

We now describe how the radial flows u_r, given by eqn. 5.9, affect the elongation and alignment of cells as quantified by the nematic order parameter $\mathbf{Q}$. To this end, we consider an aggregate of initially isotropic cells, $\mathbf{Q}(\mathbf{x}, t) = 0$. As outlined in appendix C.3, the stability of the isotropic state is governed by

$$\dot{Q}_{ij} = \frac{2}{3}\xi \tilde{E}_{ij} \,, \tag{5.10}$$

where $\tilde{E}_{ij} = E_{ij} - \delta_{ij}E_{kk}/3$ is the traceless part of the strain rate tensor $E_{ij} = (\partial_j u_i + \partial_i u_j)/2$. The *flow-alignment parameter* ξ describes how pure shear flows affect the orientation of cells, where the sign of ξ determines whether cells align parallel or perpendicular to the shear axis.

Using spherical coordinates, the initial growth rates of the radial component Q_{rr} and angular components $Q_{\phi\phi}$, $Q_{\theta\theta}$ are (see appendix C.3)

$$\dot{Q}_{rr} = \frac{4}{9}\xi \left(\partial_r u_r - \frac{u_r}{r}\right) \,, \tag{5.11}$$

$$\dot{Q}_{\theta\theta} = \dot{Q}_{\phi\phi} = -\frac{1}{2}\dot{Q}_{rr} \,. \tag{5.12}$$

From eqn. 5.9 it follows that $(\partial_r u_r - u_r/r) \sim \tilde{r}^{-1}\sinh\tilde{r} + 3\,\tilde{r}^{-2}(\tilde{r}^{-1}\sinh\tilde{r} - \cosh\tilde{r}) > 0$, thus isotropic cells inside spheroids become radially elongated for $\xi > 0$ and radially compressed for $\xi < 0$ (Fig. 5.1 d). Since the strength of the alignment depends on the magnitude of the strain rate, the growth rate of radial alignment scales as $\dot{Q}_{rr} \sim \xi k_p$ and increases along the radial direction, reaching a maximum at the surface $r = R$. Although the magnitude of alignment S initially follows eqn. 5.11, at later times the director field is subject to higher-order effects such as advection, and flow-induced cell elongation through the co-rotational term $\mathcal{W}$ is eventually balanced by passive restoring forces arising from the molecular field $\mathbf{H}$ (Fig. 5.2 f). The cell

alignment profile at steady state depends on mechanical cell parameters, however, alignment profiles retain the main features seen at early times with cell alignment being maximal near the surface and decreasing towards the core (Fig. 5.2 g,h).

5.5 Growth-induced activity gradients

We now consider the limit where cell flows are dominated by dipolar active stress ζ produced by cell division and death and growth-induced radial flows are negligible, $\nabla \cdot \mathbf{u} \approx 0$. Active nematic stress creates a well-known hydrodynamic instability which constantly pushes the system out of equilibrium, leading to a state termed active turbulence. 3D active turbulence is characterised by spatiotemporally chaotic flows (Fig. 5.3 a) and the presence of self-propelled disclination lines (Fig. 5.4 c). In this section we will focus on how activity gradients affect the time-averaged alignment of the director at certain distances from spheroid centre, which is a quantity that can be easily measured in experiments [43, 137].

To investigate how activity gradients affect cell alignment inside spheroids, we measure the distribution of the angle θ between the director $\mathbf{n}$ and the radial vector $\hat{\mathbf{r}}$ at different distances from the centre of aggregates. Since there are more possible configurations for angular alignment ($\theta = \pi/2$) than for radial alignment ($\theta = 0$), a randomly aligned director field results in a uniform distribution of $\cos\theta \sim \mathcal{U}[0, 1]$. Preferred angular or radial alignment leads to a biased distribution towards 0 or 1, respectively.

Fig. 5.3 c shows a typical alignment profile across the spheroid. In the core cells are preferentially extended radially while close to the surface cells are extended along angular directions. In the transition region $r = r_{\text{trans}}$ between the shell and the core the director field has a random orientation.

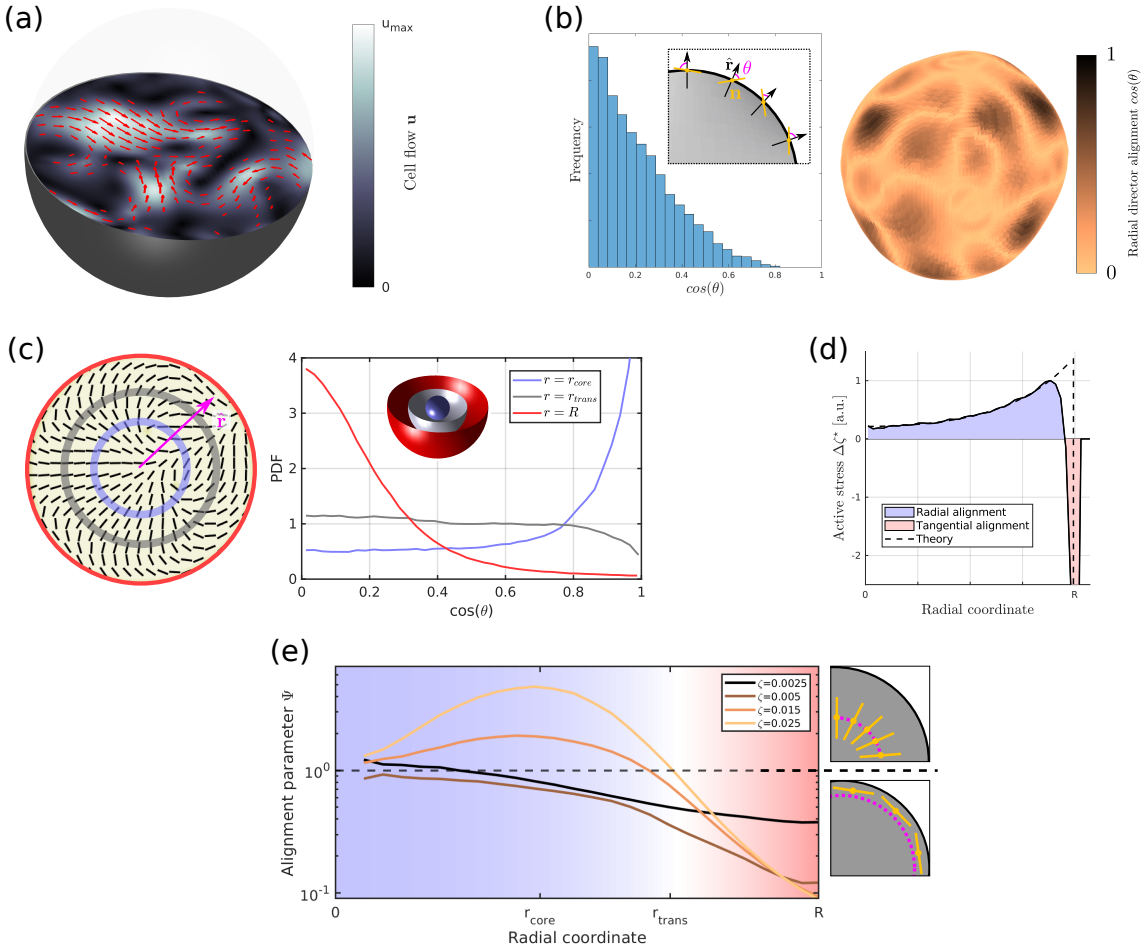


Figure 5.3: **(a)** Two-dimensional cross-section of the velocity field inside an active spheroid showing spatiotemporally chaotic flows caused by self-propelled disclination lines. Arrows and colour bar refer to the in-plane component of the flow field. **(b)** Histogram (left) and spatial distribution (right) of the angle θ between the director $\mathbf{n}$ and the radial vector $\hat{\mathbf{r}}$ at the surface of spheroids shows strong tangential director alignment caused by a hydrodynamic anchoring force termed active anchoring. **(c)** Two-dimensional cross-section of the in-plane component of the director field (left) and the probability distribution of $\cos\theta$ (right) obtained by spatial averages at a given radius $[r, r+\delta r]$ and over time. The distributions at radii $r_{\text{core}} < r_{\text{trans}} < R$ are shown as blue, grey, and red, respectively. **(d)** $\nabla^2\zeta^\star$ obtained from simulations of quasi-spherical droplets. Activity gradients set up flows which create radial cell alignment inside the aggregate ($\nabla^2\zeta^\star > 0$, blue area) and tangential alignment close to the surface ($\nabla^2\zeta^\star < 0$, red area). The black, dashed line shows the analytical prediction eqn. 5.13 for spherical aggregates with a sharp interface at $r = R$. **(e)** Cell alignment parameter Ψ as a function of radial coordinate for different magnitudes of active stress ζ. Simulations were performed using the following parameters, unless stated otherwise in the legend: spheroid radius $R = 30$, $\ell_m = 4$, $m_c = 0.3$, $K_{LC} = 0.04$, $\zeta = 0.025$, $\xi = 0$, $k_p = 0$.

Recalling that the active stress is $\Pi_{act} = -\zeta^\star\mathbf{Q}$, (eqn. 5.5), we can identify two competing mechanisms that lead to cell alignment. Firstly, radial alignment

in the bulk of spheroids is driven by gradients in active stress resulting from metabolite gradients. As was shown in the previous chapter 4, hydrodynamic forces set up by activity gradients align the director field parallel to the gradient direction in regions where $\nabla^2\zeta^\star > 0$ and perpendicular where $\nabla^2\zeta^\star < 0$. Inside spherical aggregates eqns. 5.6, 5.7 yield

$$\nabla^2\zeta^\star = \frac{\zeta}{\ell_m^2}\left[\frac{R\ \sinh\tilde{r}}{r\ \sinh\tilde{R}}\right] , \tag{5.13}$$

which is positive throughout the cell aggregate, thus driving radial cell alignment.

Secondly, since the nematic droplet is surrounded by a passive isotropic fluid, the magnitude of extensile stress $\zeta^\star$ drops rapidly to zero across the surface of the aggregate, thus active anchoring aligns the director field tangential to the surface (Fig. 5.3 b). This effect is restricted to the outer shell of spheroids, with a thickness given by the length-scale over which cell density φ drops to zero, which is typically of the order of a single cell size (Fig. 5.3 d).

Thus the cell alignment profile in Fig. 5.3 c results from a competition between radial alignment due to activity gradients in the bulk, tangential alignment resulting from active anchoring at the aggregate surface and elastic forces which tend to smooth out distortions in the director profile. To describe how the average cell alignment varies across aggregates with different magnitudes of active stress ζ, we define the cell alignment parameter

$$\Psi = \frac{p(\cos\theta > 0.5)}{p(\cos\theta < 0.5)} , \tag{5.14}$$

which quantifies the degree of radial ($\Psi > 1$) or angular ($\Psi < 1$) cell alignment as a function of distance r from the centre of spheroids (Fig. 5.3 e). Alternative methods to quantify cell alignment, e.g. $\langle\cos\theta\rangle$ as a function of r, lead to qualitatively similar results (Fig. 5.4 a).

If activity is sufficiently large ($\zeta \geq 0.015$) the director field shows strong radial alignment close to the core $r = r_{\text{core}}$ and tangential alignment close to the surface $r = R$, with weak or no alignment in the transition region $r = r_{\text{trans}}$. Note that, because of symmetry, there is no radial alignment at the centre of aggregates

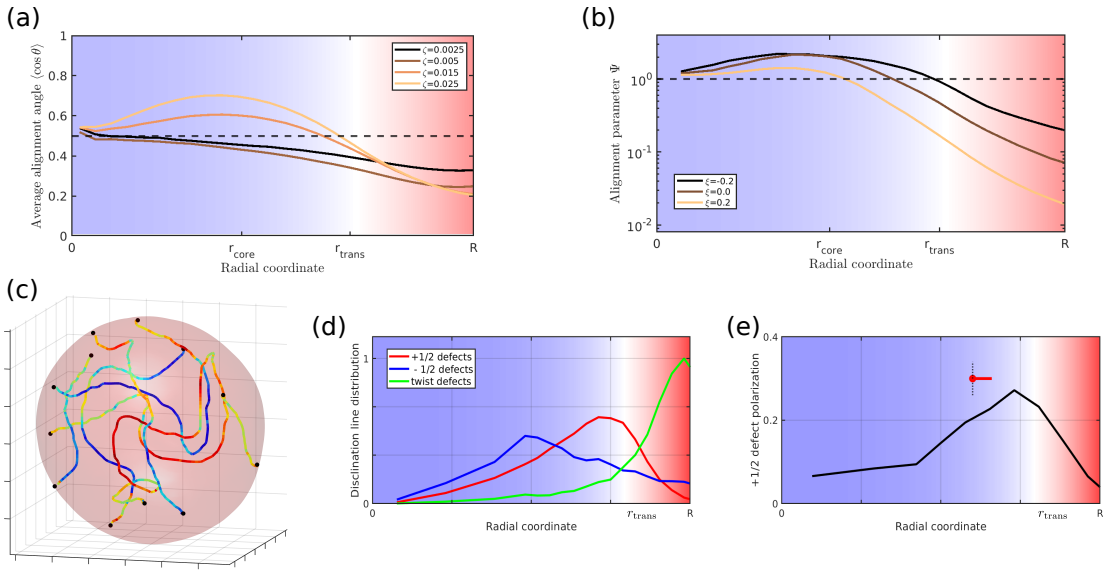


Figure 5.4: **(a)** Cell alignment quantified by the average alignment angle $\langle \cos\theta \rangle$ as a function of radial coordinate for different magnitudes of active stress ζ. The data is identical to that used in Fig. 5.3 e. **(b)** Cell alignment Ψ for different values of alignment parameter ξ. All other parameters are identical to the ones in Fig. Fig. 5.3. **(c)** Due to activity disclination lines act as self-propelled entities moving through the fluid leading to spatiotemporally chaotic flows. Disclination lines constantly undergo transformation events such as breakup, recombination, nucleation and annihilation and form either closed, charge-neutral loops in the bulk or terminate at the surface of droplets. **(d)** The distribution of disclination types follows the activity profile $\zeta^\star \sim (m - m_c)$, where contractile regions in the core are dominated by wedge-type $\pm 1/2$ disclinations and twist-type defects are preferentially formed in extensile regions close to the surface. **(e)** Activity gradients in the aggregate create active torques on $+1/2$ defects which aligns them parallel to activity gradients, where the head-to-tail vector $\mathbf{p} \sim \nabla\zeta^\star$. Using the polarization order parameter $\mathcal{P}$ defined in chapter 4, we find that $+1/2$ defects are radially polarized throughout the aggregate. The defect polarization reaches a maximum at the radius $r \approx r_{\text{trans}}$, where $\zeta^\star \approx 0$ and activity gradients dominate isotropic active turbulence. This is also reflected in the radial defect distribution in (d), where radially polarized $+1/2$ defects move outwards/inwards in contractile/extensile regions, thus accumulating around $r \approx r_{\text{trans}}$.

$r \approx 0$ since activity driven alignment cannot overcome the increasing elastic energy associated with a nematic hedgehog configuration close to the centre. These values of activity correspond to active turbulence and disclination lines are spontaneously created inside the aggregate. The density of different disclination types and the polarization of $+1/2$ segments follows spatial variations in active stress (Fig. 5.4 d,e), which is in line with the analysis of 3D bulk in chapter 4.

At very low activity ($\zeta \leq 0.005$) we find that active anchoring creates weak

tangential cell alignment close to the surface, with a magnitude that decreases with decreasing activity. The angular alignment decays monotonically towards the core of spheroids without showing any radial alignment at intermediate distances because active stress is not strong enough to overcome elastic forces. Although activity-driven director alignment does not rely on specific shear-alignment $\xi \neq 0$, it should be noted that the magnitude of alignment slightly depends on ξ, as shown in Fig. 5.4 b.

5.6 Interplay between converging cell flows and activity gradients

We now combine the main findings of sections 5.4 and 5.5 and study the interplay between converging flows set up by differential volume growth $\nabla \cdot \mathbf{u} = k_p^\star$ across spheroids and spatiotemporally chaotic flows created by dipolar stresses $\Pi_{act} = -\zeta^\star \mathbf{Q}$ arising from cell divisions and death. The spatial and temporal variations of flow fields in active turbulence are characterized by the active length-scale $\ell_a = \sqrt{K_{LC}/\zeta}$ and time scale $\tau_a = \eta/\zeta$. While instantaneous flow fields $\mathbf{u}(\mathbf{x}, t)$ inside spheroids can be indistinguishable from active turbulence if active stress is sufficiently large, $\zeta/\eta > k_p$, chaotic flow patterns average out over time scales $T \gg \tau_a$ and the time-averaged velocity field $\langle \mathbf{u}(r) \rangle_t$ reduces to the converging cell flows given by eqn. 5.9 (Fig. 5.5 a). This behaviour is expected by symmetry since spatiotemporal chaotic flows in bulk active nematics are isotropic, therefore they do not contribute to time-averaged flows [80, 123, 138].

5.6.1 Cell orientation inside spheroids

We first consider the cell orientation at the surface of a spheroid, where the strain rate of converging flows reaches a maximum. Thus, following eqn. 5.11, the director orientation is most strongly affected by converging flows at the surface. Strains due to the converging component $\langle \mathbf{u} \rangle_t$ of the flow field, which is set up by eqn. 5.3, drive radial surface cell orientation for $\xi > 0$, while active anchoring, driven by active stress, favours cells aligning tangentially to the surface. The magnitudes of

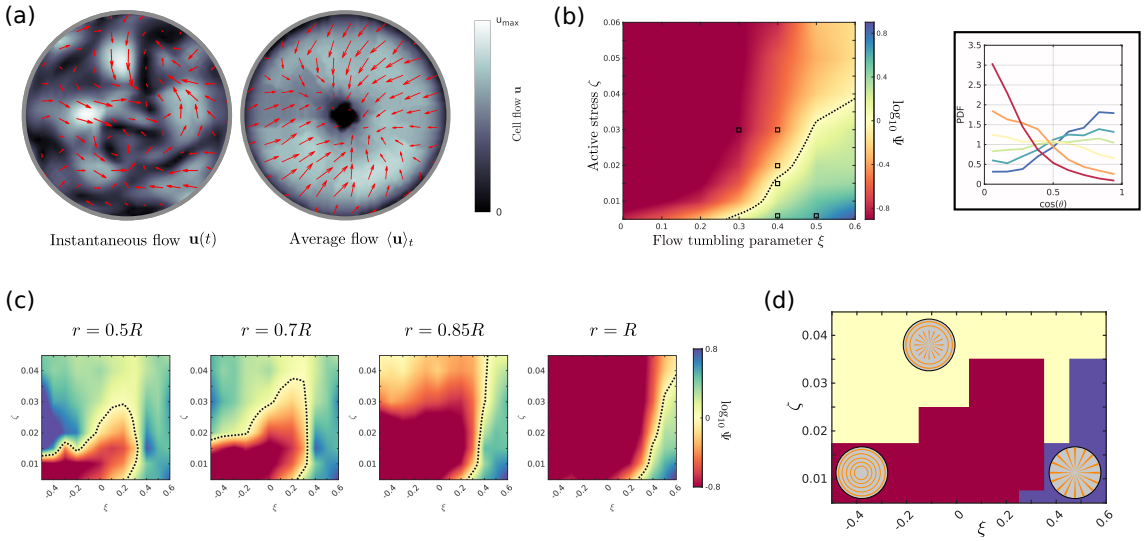


Figure 5.5: **(a)** Cross-section of an instantaneous velocity field (left) and time-averaged velocity field (right) inside spheroids with $k_p > 0$ and $\zeta > 0$. The chaotic flows of active turbulence seen in the instantaneous flow $\mathbf{u}$ average out over time scales $T \gg \tau_a$, to give a time-averaged flow $\langle \mathbf{u} \rangle_t$ resembling the converging flow-component driven by $\nabla \cdot \mathbf{u} = k_p^\star$. Arrows and colour bar show the components of the flow field in the equatorial plane. The average velocity field $\langle \mathbf{u} \rangle_t$ is obtained by averaging over time $[0, 1500\tau_a]$. **(b)** Heat map of the cell alignment parameter Ψ at the surface of steady-state spheroids $r = R$ as a function of active stress magnitude ζ and flow-alignment parameter ξ. Red/blue regions correspond to tangential/radial surface alignment, respectively. The black, dotted line indicates the transition region where the director field has a random orientation ($\Psi = 1$) because the flow-induced alignment balances active anchoring. The right panel shows the distribution of $\cos\theta$ from which Ψ was calculated for six different parameter values indicated by black squares in the left panel. **(c)** Alignment parameter Ψ shown at four different distances from the spheroid centre as a function of ζ and ξ. The shape of the contour line $\Psi = 1$ (black dots) varies along the radial direction, converging to the distribution shown in panel (b) close the surface. **(d)** Three distinct regimes can be identified from variations of the cell alignment parameter at the surface, $\Psi_s = \Psi(R)$, and in the core, $\Psi_c = \Psi(R/2)$: homogeneous spheroids with radial (blue, $\Psi_c > 0$, $\Psi_s > 0$) or tangential orientation (red, $\Psi_c < 0$ $\Psi_s < 0$) and heterogeneous spheroids with tangential cell orientation close to the surface and radial alignment in the core (yellow, $\Psi_c > 0$, $\Psi_s < 0$).

proliferation-driven alignment and active anchoring increase with the flow-alignment parameter $|\xi|$ and active stress ζ, respectively. To investigate the cross-over between these competing effects, we measure the cell alignment parameter Ψ at the surface of steady-state spheroids over a range of parameter values ξ and ζ (Fig. 5.5 b). For $\xi = 0$ the orientation of cells does not respond to the strain rate $\mathbf{E}$ of flows, thus active anchoring dominates at any activity level $\zeta > 0$, which creates strong tangential surface alignment. As $\xi > 0$ increases, however, the cell orientation

responds more strongly to the fluid strain rate at the surface and the director field aligns radially due to velocity gradients caused by proliferation as long as active anchoring is sufficiently small, $\zeta < \zeta_c$. Since shear-driven cell alignment scales as $\dot{Q}_{ij} \sim \xi \tilde{E}_{ij}$, the critical activity ζ_c above which active anchoring dominates increases with the strain rate at the surface $\tilde{E}_{rr} \sim k_p$ and ξ. The function $\zeta_c(\xi)$ is shown by the black, dotted line in Fig. 5.5 b.

In addition to cell orientation at the surface, we can also measure Ψ at a finite distance $0 < r < R$ from the centre of spheroids as a function of ζ and ξ (Fig. 5.5 c). For low activity and $\xi = 0$, the director field in the core ($r = 0.5R$) shows weak alignment since the orientation at the surface decays very slowly towards the centre due to the dominance of the elastic energy associated with distortions in the director field over active stresses. Thus, in the regime of low activity, cell orientation throughout spheroids is dictated by the cell alignment at the surface. As soon as radial shear-alignment becomes dominant at the surface for $\xi > \xi_c$, cells globally switch from angular to radial orientation (see phase diagram Fig. 5.5 d for $\zeta < 0.02$).

In section 5.5 we showed that for sufficiently large activity $\zeta > \zeta_c$, the core of spheroids shows radial alignment while at the surface cells are oriented tangentially because of the balance between activity gradient-induced radial ordering and tangential active anchoring. Surprisingly, the activity threshold ζ_c above which radial order is created in the core decreases for $\xi < 0$, even though converging flows favour tangential over radial alignment throughout spheroids for $\xi < 0$ (see boundary between red and yellow domains in Fig. 5.5 d). This non-trivial behaviour can be explained in terms of the disclination line structure inside aggregates.

5.6.2 Spheroid rotation and dancing disclinations

Active anchoring creates significant surface alignment, but usually it is not strong enough to completely enforce tangential anchoring everywhere on the surface (see Fig. 5.3 b). As $\xi < 0$ decreases, however, the tangential surface anchoring of the director field eventually becomes sufficiently strong that the Gauss–Bonnet theorem can be applied. This states that the total topological charge of a vector

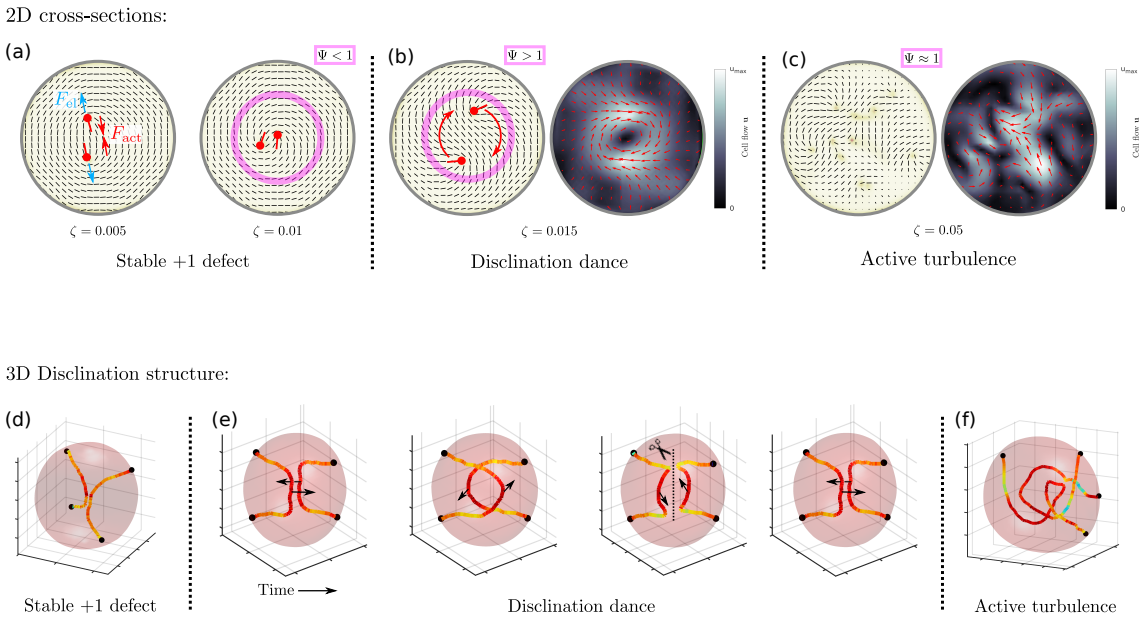


Figure 5.6: As the activity ζ is progressively increased inside proliferating spheroids with $\xi < 0$, the droplet undergoes three dynamical regimes: first a quiescent regime where converging flows are dominant (a,d), then a rotational *dancing disclination* regime, where disclination lines spontaneously set up a rotational flow and, finally, active turbulence. **(a,d)** Two-dimensional cross-sections of the director field and disclination line structure. At very low activity the director field is stationary and the 2D cross-section resembles a $+1$ defect with angular director alignment ($\Psi < 1$), where two $+1/2$ defects are located at a small finite distance to the centre. Contractile stress around defects creates active forces F_{act} pointing towards the centre (red). If activity is sufficient small, active forces are balanced by repulsive elastic forces F_{el} (blue) arising from an increased elastic energy as the distance between $+1/2$ defects decreases. **(b,e)** If activity surpasses a critical threshold ζ_c, the system reaches a steady-state where the two $+1/2$ disclination lines start orbiting around each other, thereby creating persistent rotational motion in the core of spheroids, as shown by the cross-section of the velocity field. The outward-facing orientation of the defects creates significant radial alignment of the director field in the vicinity of the orbiting defects ($\Psi > 1$). The rotational motion of defects in the core makes it inevitable that disclination lines must cross after each full rotation, thereby rewiring some line segments (see third panel in e). **(c,f)** As activity progressively increases, the motion of disclination lines and flow fields becomes more chaotic and the system eventually reaches active turbulence. The snapshots shown in this figure were obtained for $\xi = -0.4$.

field tangentially anchored on a sphere must be $+2$, the Euler-characteristic χ of the sphere [139].

At very low activity and $\xi < 0$, the director field thus relaxes into a configuration that minimizes its elastic energy while meeting the topological constraint close to the surface. This resulting defect structure consists of two $+1/2$ disclination lines which

bend towards the centre of the droplet and create four +1/2 defects at the surface. The cross-section of the director field inside droplets shows two +1/2 defects located close to the centre, hence the director field around them resembles that around a two-dimensional +1 defect (Fig. 5.6 a,d). Due to the large elastic energy associated with a point-like +1 defect, there is a finite repulsion force between the two +1/2 defects which keeps them at a finite distance. On the other hand, contractile active forces at the position of +1/2 defects oppose the elastic forces, thus the distance between the two stationary disclination lines decreases with increasing activity.

If activity reaches a critical threshold $\zeta > \zeta_c(\xi)$, the two +1/2 defects at the centre slip past each other and subsequently reach a steady-state in which both defects orbit around the centre, thereby creating persistent rotational motion in the core of spheroids (Fig. 5.6 b). In 3D this corresponds to a *dancing disclination* state, where the +1/2 line segments in the core orbit around the centre, while the end-points of disclination lines at the surface move very slowly. This motion makes it inevitable that disclination lines must cross after each full rotation, thereby rewiring some of the line segments in the core (Fig. 5.6 e). We note that the rotational motion of disclination lines is reminiscent of persistent clockwise or counter-clockwise rotations in active nematic systems in circular (2D) or spherical (3D) confinement which has been observed in experiments [140] and simulations [81, 141, 142]. The orientation of +1/2 defects in the dancing disclination state creates significant radial alignment of the director field outside the orbiting defects, hence Ψ shows a sharp transition from angular to radial director alignment in the core at $\zeta = \zeta_c(\xi)$ (Fig. 5.5 c). As the activity ζ is increased even further, the motion of the disclination lines becomes more chaotic and eventually the oscillations are lost in the active turbulent background (Fig. 5.6 c,f).

5.7 Parameter inference for biological systems

Finally we apply our theoretical active fluid model to experimental data obtained from freely grown proliferating spheroids to make quantitative predictions about dynamical tissue parameters, such as active stress ζ and the flow-alignment parameter ξ. Since it is rarely possible in experiments to simultaneously measure proliferation gradients, active stress, cell flows and cell orientations inside spheroids, we require physical estimates for model parameters ℓ_m, m_c and k_p.

5.7.1 Estimating tissue parameters

The characteristic penetration length ℓ_m of metabolites can be estimated by measuring proliferation profiles in spheroids. This can be realized either by using immuno-fluorescence staining procedures to mark proliferating cells [143] or by using spheroid models expressing Fucci (Fluorescence Ubiquitination Cell Cycle Indicators), tools that allow monitoring the cell cycle position of each cell [144]. The metabolite penetration length from the surface can vary upon the cell packing density and the cell type, however, for most types of human tumour cells grown under optimal nutrient and oxygen conditions the penetration length typically varies between $\ell_m \approx 100 - 200\ \mu m$ [145–147]. Assuming spheroids are at steady-state, the critical metabolite concentration m_c can then be inferred from the aggregate size R_c using eqn. 5.8, $m_c = 3(x \coth x - 1)/x^2$, where $x = R_c/\ell_m$ (Fig. 5.2 a).

The cell division rate k_+ is determined by the time interval between cell divisions, the cell-cycle time T_C, and the proportion of cells engaged in the cell cycle, the growth fraction $\mathfrak{f}$, such that $k_+ = \mathfrak{f}/T_C$. The growth fraction $\mathfrak{f}(\mathbf{x})$ depends on the local metabolite concentration and varies along the radial direction inside spheroids [44, 146]. Assuming $k_p^\star = k_+$ at the surface (no cell death), the growth magnitude k_p can be most easily estimated from the growth fraction $\mathfrak{f}^s$ at the surface of spheroids,

$$k_p = \mathfrak{f}^s/[T_c(1 - m_c)] \,, \tag{5.15}$$

where $\mathfrak{f}^s$ typically varies between $0.6 - 0.9$ [44, 45, 146, 148]. The cell-cycle time in carcinoma spheroids and tumours is typically around $T_C \approx 20\ h$, with slight

variations across different cell types [127, 149]. To validate the proposed parameter estimates, we compare our model to a system of freely grown CT26 spheroids at steady-state with radius $R_c = 450\ \mu m$, corresponding to $m_c \approx 0.7$. In the outer layer of the spheroids, $0.8 < r/R < 1$, eqn. 5.9 predicts an average radial flow velocity $u_r \approx 0.06\ \mathfrak{f}^s/T_c \approx 26\ \mu m\ \text{day}^{-1}$, which is in good agreement with the radial flow measured in experiments using fluorescently labelled particles, $u_r^{exp} = 21\ \mu m\ \text{day}^{-1}$ [127].

Mitotic cells in three-dimensional microenvironments generate substantial protrusive forces which were estimated to be on the order of $\zeta_+ \approx 1 - 2\ kPa$ [150]. Considering that the mitotic time T_M over which strong anisotropic forces are generated is relatively short compared to the cell cycle time, $T_M/T_C \approx 0.1$, the average stress produced by cell divisions over a cell cycle is $\zeta \approx 100 - 200\ Pa$. Similar magnitudes of cell-generated anisotropic stress were measured within proliferating multicellular spheroids using fluorescently labelled, cell-sized oil droplets or polyacrylamide microspheres to measure stresses in situ [148, 151].

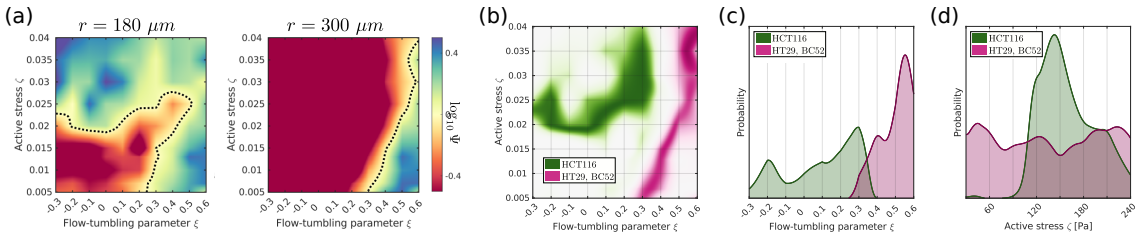


Figure 5.7: **(a)** Cell alignment Ψ in the core and close to the surface of spheroids of size $R = 300\mu m$ using simulation parameters estimated from experimental data. **(b)** Posterior distributions $p(\zeta, \xi|\mathbf{X})$ of activity ζ and flow-alignment parameter ξ inferred from cell orientations inside HCT116 (green) and HT29/BC52 spheroids (magenta) using $\sigma = 0.2$. Based on the available data [43, 137], we estimated $\mathbf{X} = [\log \Psi_c^{exp} > 0.1, \log \Psi_s^{exp} = 0]$ for HT29/BC52 spheroids and $\mathbf{X} = [\log \Psi_c^{exp} = 0, \log \Psi_s^{exp} < -0.4]$ for HCT116. **(c,d)** Marginal distributions $p(\xi|\mathbf{X})$ and $p(\zeta|\mathbf{X})$.

5.7.2 Inference of the flow-alignment parameter

We now compare our active fluid model to experimental data obtained from freely grown proliferating spheroids ($R \approx 300\mu m$) consisting of human colon carcinoma cells (HCT116) [137], colon adenocarcinoma cells (HT29) and human breast cancer

cells (BC52) [43]. It has been reported that both the orientation and the division axis of cells inside HCT116 spheroids show significant tangential alignment close to the surface ($\Psi_s^{exp} < 1$, $cos\langle\theta\rangle = 0.22$) while showing no significant alignment in the core ($\Psi_c^{exp} \approx 1$, $cos\langle\theta\rangle = 0.44$). On the other hand, the analysis of cell shapes and polarity inside HT29 and BC52 spheroids revealed that cells show only weak surface alignment ($\Psi_s^{exp} \approx 1$) while cells are increasingly radially elongated towards the core ($\Psi_c^{exp} > 1$).

Assuming $\ell_m = 150\ \mu m$, $\mathfrak{f}^s = 0.7$ and $T_C = 20\ h$, we calculated the average cell alignment Ψ_s at the surface ($r = 300\mu m$) and Ψ_c in the core of spheroids ($r = 180\mu m$) over a range of values for ζ and ξ (Fig. 5.7 a). By comparing Ψ_s and Ψ_c obtained from simulations with experimental data, we calculate the posterior distributions $p(\Theta|\mathbf{X})$ over model parameters $\Theta = [\zeta, \xi]$ given data $\mathbf{X} = [\Psi_s^{exp}, \Psi_c^{exp}]$. Given the qualitative nature of the experimental data, we assume that the likelihood function $\mathcal{L}(\mathbf{X}|\Theta)$ follows a normal distribution, $\log \Psi(\Theta) \sim \mathcal{N}(\mu = \log \Psi^{exp}, \sigma)$, where σ quantifies the allowed tolerance between data and experimental measurements. The parameter distributions $p(\zeta, \xi|\mathbf{X})$ obtained for HCT116 (green) and HT29/BC52 spheroids (magenta) are presented in Fig. 5.7 b. We find that tissue dynamics within HT29 and BC52 spheroids is governed by a positive flow-alignment parameter ($\xi \approx 0.5$) while in HCT116 spheroids shear-alignment of cells is less dominant ($\xi < 0.3$) and potentially even negative (Fig. 5.7 c). We also gain some additional information about the magnitude of active stress inside aggregates, where cell divisions inside HCT116 spheroids produce on average $\zeta = 100 - 200\ Pa$ (Fig. 5.7 c), thus confirming our previous experimental estimate based on $\zeta = \zeta_+ T_M/T_C$.

5.8 Summary and Discussion

In this chapter we have investigated how radial flows and active stresses affect cell alignment inside proliferating multicellular spheroids using three-dimensional active nematic droplets as a model system. Cell orientatiosn and flows inside aggregates are described by a continuous director $\mathbf{n}$ and velocity field $\mathbf{u}$, which follow the hydrodynamic equations of motion of active nematics. Diffusive transport of metabolites creates proliferation gradients across spheroids, where cells close to the surface have sufficient access to metabolites and divide, while metabolites are depleted in the core of spheroids and cells die. Since cell division/death is associated with a mass source/sink and extensile/contractile active stress along the cell orientation axis, proliferation gradients induce radial cell flows and activity gradients inside spheroids.

We showed that converging cell flows inside steady-state spheroids can promote radial or circumferential cell alignment, depending on the sign of the flow-alignment parameter ξ, a tissue parameter quantifying how cell orientations respond to shear-flows. The magnitude of shear-driven alignment scales with ξ and with the strain rate, the latter reaching a maximum at the surface and decreasing towards the core.

Active stress, on the other hand, creates a well-known hydrodynamic instability which leads to a chaotic steady state termed active turbulence. Activity gradients impact the average director field orientation inside spheroids in two ways: first, smooth variations between contractile stress in the core and extensile stress at the surface of spheroids drive radial cell alignment by creating flows which reorient the director field. The second contribution is active anchoring, due to the sudden drop of extensile activity across the interface of spheroids. The resulting sharp activity gradients at the surface induce flows which rotate the director field planar to the interface, thus creating strong tangential surface alignment. Therefore gradients in active stress are responsible for radial core alignment and tangential surface alignment.

Depending on the relative strength of flow-driven shear-alignment and activity induced alignment, we find three distinct cell orientation regimes inside spheroids:

for small activity, cell orientation is either tangential throughout the aggregate for $\xi < \xi_c$ or radial for $\xi > \xi_c > 0$. If active stress becomes sufficiently large, $\zeta > \zeta_c(\xi)$, one recovers spheroids with radial core alignment and tangential surface alignment (Fig. 5.5 d).

The cell orientation profile inside aggregates significantly affects the stress distribution and short-time response of spheroids to external pressure jumps [43]. It has also been shown that the elongation and orientation of cells within fibrosarcoma spheroids contribute to invasive behaviour by priming cells at the spheroid periphery to exhibit the correct morphology and polarization for effective invasion into the surrounding matrix [152]. The activity level and flow-alignment properties of cellular aggregates could thus be used as control parameters to guide the migratory behaviour of spheroids and their mechanical response to changes in their environment.

Furthermore, we apply our model to experimental systems of freely grown HCT116, HT29 and BC52 spheroids to infer distributions of tissue parameters ξ and ζ based on the distribution of cell orientations inside spheroids. We find a significant difference in shear-alignment across different systems, with $\xi \approx 0.5$ for HT29/BC52 spheroids, while for HCT116 spheroids shear-alignment $\xi < 0.3$ is less dominant and potentially even negative. It is of interest to compare these results with previous measurements of cell motion in two-dimensional systems, which indicated that cell orientation and flows in dense monolayers of myoblasts and epithelial cells are governed by a negative flow-alignment parameter ν, which corresponds to $\xi > 0$ [63, 153]. This suggests that the same biomechanical mechanisms that cause flow-induced realignment of cells in monolayers may play an important role in three-dimensional tissue organisation.

We hope that recent developments in experimental techniques and data processing will permit the measurement of 3D cell orientations inside aggregates with high spatial and temporal resolution in the future. This would allow the inference of more complex dynamics, including features like non-linear relationships between proliferation rate $k_p^\star$ and metabolite concentration m or spatial variations of ξ within aggregates. Furthermore, data with a sufficient temporal resolution would allow

the testing of hypotheses relating to the underlying dynamics of cells, such as a possible dependence of intrinsic activity ζ_0 or flow-alignment ξ on internal cell states, giving rise to time-dependent parameters $\zeta^\star(t)$ and $\xi(t)$, which could be inferred from the cell alignment profiles. Here we highlight the potential of active fluid theories to model complex biological systems and show that cell orientation profiles in proliferating spheroids can be used to extract dynamical tissue parameters, which are otherwise difficult to measure directly.

Take-home message:

Variations in the cell division rate inside spheroids generate flows and activity gradients, which reorient cells and create distinct cell alignment profiles. This motivates new ways to guide the mechanical response and migratory behaviour of spheroids, and also enables the inference of tissue parameters based on simple experimental data.

6

Application II: Decoupling cell orientation and active forces

Up to this point we have assumed that extensile or contractile active stress is always generated along the orientation of the director field $\mathbf{n}$. In the last chapter of this thesis, we will relax this constraint by decoupling cell-generated active forces from cell orientation thus allowing active dipolar forces to be generated along an arbitrary direction $\mathbf{m} \neq \mathbf{n}$. Using a 2D continuum model which models the sub-cellular structures which are responsible for active force-generation inside cells, we investigate the relationship between cell orientation, flows and the direction of cell-generated forces in confluent cell layers. We find that misalignment between cell orientation and active forces is linked to topological defects in the cell orientation field. We also report the emergence of domains in which the misalignment between cell orientation and contractile forces reaches 90°, thereby effectively creating domains of extensile activity in a monolayer of contractile cells. This challenges the prevailing understanding that cells throughout a tissue create either contractile or extensile forces and shows that the type of active forces cells generate can vary continuously across tissues.

6.1 Introduction

In many confluent cell layers cells tend to align their orientation with neighbouring cells, leading to long-range orientational order like in liquid crystals. Cells can generate forces in many different ways, typically involving the cell cortex or the cytoskeleton where molecular motors convert chemical energy in form of ATP into mechanical work. The contractile forces generated by these actin-based structures are often on average aligned along the cell orientation, defined as the major principal axis of cell shape [32, 154, 155].

The prevailing assumption in most cell modelling work so far has been that the stress and shape axes are tightly coupled. We now challenge this and show that flows in cell layers give rise to dynamic, correlated regions where the stress and cell shape axes are misaligned. By extending the continuum model of active nematics to allow for force-shape misalignment, we are able to replicate force patterns seen in experimental monolayers of MDCK cells and highlight the major role of topological defects in causing these patterns.

We start in section 6.2 by proposing a novel mechanism which can potentially lead to force misalignment in tissues and derive an equation of motion for the misalignment angle. This is followed by brief explanation of the simulation methods in section 6.3. In section 6.4 we investigate the spatiotemporal patterns of mismatched forces and topological defects in the cell orientation field. We numerically explore the phase-space of the tissue model and show that the proposed mechanism can lead to different patterns of extensile stresses depending on dynamical tissue parameters, such as the flow-alignment parameter. Subsequently we compare our simulation results to experimental MDCK data. We conclude this chapter in section 6.5 by discussing the wider implications of the proposed mechanism in the light of recent experimental and theoretical work.

6.2 Governing equations

6.2.1 Biological Motivation

Many cells contain bundles of actomyosin, termed stress fibres, that are the major mediators of cell contraction. Cortical stress fibres are a specific type of stress fibre which are embedded in the cell cortex and assemble preferentially underneath the nucleus close to the underlying substrate [156]. Stress fibres are formed by reorganising the cortical actin mesh into regular bundles and are stabilized by focal adhesions which connect the fibres to the underlying substrate [157]. Simultaneous measurements of cell-generated forces, cell orientations and the ordering of cortical stress fibres inside cells show that most stress fibres are aligned along the axis of contractile stress. Building upon these observations, we construct a continuum tissue model which includes the dynamics of the sub-cellular stress fibres based on the following assumptions:

1. Contractile dipolar stress is generated along the direction of cortical stress fibres inside cells.

2. The orientation of stress fibres tends to align with the cell shape orientation axis via reorganization of the cortical actomyosin. Since stress fibres are anchored to the substrate via focal adhesions, they are only weakly affected by the motion of surrounding cells and relaxation of their direction to the cell shape axis is slow.

3. Tissue-scale cell flows affect the shape of cells and thus change the cell orientation. Based on previous studies, we assume that cell orientations inside tissues follow the equations of motion of nematic liquid crystals.

In the following we derive equations of motion for both the cell orientation field and the orientation of sub-cellular stress fibres. Since cells in tissues are connected to each other by various adhesion mechanisms, cell orientation is affected by the motion of neighbouring cells and thus follows the equations of motion of nematic liquid crystals. The orientation of stress fibres, on the other hand, is not affected by cell

flows and follows the cell orientation via reorganization of the cortical actomyosin. This allows a finite misalignment θ between the cell orientation and stress fibres if the cell orientation changes sufficiently fast (Fig. 6.1 a). Tissues in our continuum model are therefore described by the combination of a cell orientation field and a scalar misalignment angle θ, which quantifies the misalignment of stress fibres and forces with respect to the cell orientation axis $\mathbf{n}$ (Fig. 6.1 b). As we shall show in section 6.4, spatial patterns of misalignment θ strongly correlate with the positions of $\pm 1/2$ defects in the director field.

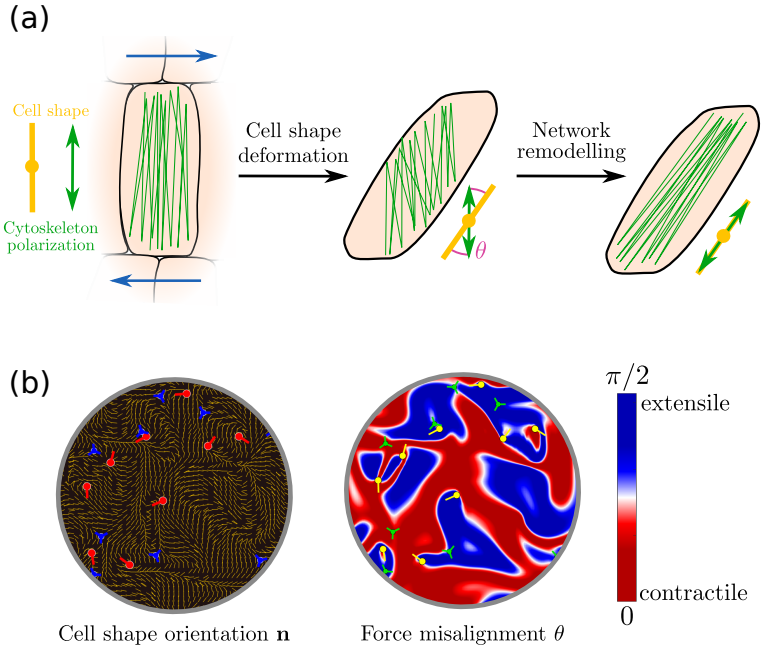


Figure 6.1: **(a)** Cell shapes change in response to the motion of neighbouring cells (cell flow). Since the cytoskeleton is more strongly anchored to the substrate, it is not immediately affected by flows and takes a finite time to re-align with the updated cell shape. This is the main mechanism which leads to misalignment between forces and shapes in cell layers. **(b)** Tissues are described by the combination of a cell orientation field $\mathbf{n}$ (left) and a scalar angle θ, which quantifies the misalignment of stress fibres with respect to the cell orientation (right). If contractile stress fibres are maximally misaligned, $\theta \approx \pi/2$, cells effectively create extensile forces along their orientation axis.

6.2.2 Coupling director fields for cell shape and stress fibres

We will now write down equations of motion for the cell orientation $\mathbf{n}$, cell flow $\mathbf{u}$ and misalignment angle θ. In the following we will denote the cell orientation axis and the orientation of sub-cellular stress fibres by director fields $\mathbf{n}$ and $\mathbf{m}$, respectively. This description allows a finite misalignment angle $\theta = \cos^{-1}(\mathbf{n} \cdot \mathbf{m})$ between the elongation axis of cells and the axis along which contractile forces are created by the cytoskeleton.

Free energy

Following empirical arguments, we assume that the tissue dynamics is governed by the free energy density,

$$f = \frac{K_1}{2}(\nabla \mathbf{n})^2 + \frac{K_2}{2}(\nabla \mathbf{m})^2 + \frac{A}{4}\sin^2(\theta)\,. \tag{6.1}$$

The first term was used throughout this thesis and penalises gradients in cell orientation $\mathbf{n}$, which arises because individual cells need to deform in order to create distortions of the director field. The cytoskeletons of neighbouring cells are usually connected via adherens junctions, which gives rise the second term penalising gradients in $\mathbf{m}$. The third term describes the tendency of actin stress fibres to align with the principal axis of the cell shape, with A being the alignment strength.

Equations of motion

We now derive the equations of motion for the orientation of cell shape $\mathbf{n}$ and stress fibres $\mathbf{m}$. In two dimensions, these quantities can be described by angles ϕ_1 and ϕ_2, respectively, where $\mathbf{n} = [\cos\phi_1, \sin\phi_1]$ and $\mathbf{m} = [\cos\phi_2, \sin\phi_2]$. Whenever neighbouring cells are moving relative to each other, their shape is distorted by viscous drag forces acting along the cell membrane or by elastic forces between cell membranes if they are connected through adhesion bonds. The ways cell orientation changes in response to cell flows can be written in the Ericksen-Leslie limit in terms of the director angle ϕ_1 (see eqn. 2.21),

$$D_t\phi_1 = \omega + \lambda\left[\cos(2\phi_1)E_{xy} - \sin(2\phi_1)E_{xx}\right] - \Gamma_1\frac{\delta\mathcal{F}}{\delta\phi_1}\,, \tag{6.2}$$

where Γ_1 is the rotational diffusivity of cell shape. The last term in eqn. 6.2 controls the relaxation of the cell orientation towards the equilibrium of free energy eqn. 6.1 in terms of ϕ_1, $\delta\mathcal{F}/\delta\phi_1 = K_1\nabla^2\phi_1 - \frac{A}{2}\sin\theta\cos\theta$.

Assuming the cytoskeleton and stress fibres are more strongly anchored to the substrate and much stiffer than the cell membrane, their orientation should be less affected by the motion of neighbouring cells compared to the cell shape. To quantify this effect, we introduce a substrate friction strength γ which modifies flow-driven rotation of stress fibres,

$$D_t\phi_2 = \frac{1}{1+\gamma}\left\{\omega + \lambda\left[\cos(2\phi_2)E_{xy} - \sin(2\phi_2)E_{xx}\right]\right\} - \Gamma_2\frac{\delta\mathcal{F}}{\delta\phi_2}\,. \tag{6.3}$$

For simplicity, in this chapter we consider the limit of strong friction, $\gamma \gg 1$, where the orientation of stress fibres only changes via network remodelling driven by the free energy $\mathcal{F}$.

Assuming that distortions of cell shape and stress fibres are associated with the same elastic energy cost, $K_1 = K_2 = K$, and $\Gamma_1 = \Gamma_2 = \Gamma$, we can derive a simple equation for the misalignment angle $\theta = \phi_1 - \phi_2$ between cell shape and stress fibres,

$$D_t\theta = \omega + \lambda(\mathbf{n}.\mathbf{E}^\star.\mathbf{n}) - \Gamma\left(A\,\sin\theta\cos\theta + K\,\nabla^2\theta\right)\,, \tag{6.4}$$

where $\mathbf{E}^\star = [(E_{xy}, -E_{xx}); (-E_{xx}, -E_{xy})]$ is a modified version of the strain rate tensor $\mathbf{E}$. Misalignment of stress fibres is thus driven by vorticity ω in the cell flow and by shear flows if $\lambda \neq 0$. The orientation of cells and stress fibres are related via $\mathbf{n} = \mathbf{R}\mathbf{m}$, where $\mathbf{R}$ is the counter-clockwise rotation matrix by angle θ, thus active forces generated along stress fibres give rise to an active stress,

$$\Pi_{act} = -\zeta\left(\mathbf{R}^T\mathbf{Q}\mathbf{R}\right)\,, \tag{6.5}$$

where $\mathbf{Q}$ is the nematic tensor constructed from the cell orientation field $\mathbf{n}$. Since stress fibres consist of contractile actomyosin, they generate contractile active stress, $\zeta < 0$.

6.3 Simulation method

We numerically solve the equations of motion for the cell orientation $\mathbf{Q}$ (eqn. 2.18), force misalignment θ (eqn. 6.4) and velocity field $\mathbf{u}$ (eqns. 2.1, 2.2) on a two-dimensional grid of size 150×150 using the hybrid lattice Boltzmann-finite difference method. We use the liquid crystal bulk free energy eqn. 2.12 and choose coefficients $\mathcal{A} = 0$, $\mathcal{B} = -4.5$, $\mathcal{C} = 4.5$ which fixes the magnitude of nematic ordering $S_0 > 0$. We use periodic boundary conditions and initialise the system with $\theta = 0$ and a random director orientation. Throughout this chapter we use the following simulation parameters, in lattice-units, unless otherwise stated: $\rho = 1$, $\eta = 2/3$, $A = 0.01$, $K = 0.05$, $\Gamma = 0.1$, $\zeta = 0.012$, $\lambda = 0$, $\Gamma_{LC} = 0.1$, $K_{LC} = 0.05$.

6.4 Flow-driven misalignment between cell orientation and forces

6.4.1 Spatial misalignment patterns

In this section we numerically investigate the full parameter space of the hydrodynamic tissue model. We start by quantifying how the distribution of force-misalignment angle θ is affected by the alignment strength A of stress fibres with respect to cell orientation and the sign and magnitude of the flow-alignment parameter λ. The numerical results are summarised in Fig. 6.2. The magnitude of the force-alignment A controls the variance of the distribution $p(\theta)$ around $\theta = 0$. For strong alignment, $p(\theta)$ is sharply peaked around $\theta = 0$ which yields a purely contractile systems. Very weak alignment, on the other hand, gives rise to systems which consist equally of extensile and contractile domains (Fig. 6.2 a,b). The flow-alignment parameter can bias the systems to form more extensile or contractile domains, depending on the sign of λ. This mechanism is related to the ways cell orientation changes in responds to self-generated shear-flows (see Fig. 2.5). If the alignment strength A of stress fibres is sufficiently small, shear flow-alignment λ can in fact shift the mode of $p(\theta)$ from $\theta = 0$ to $\theta = \pi/2$ (Fig. 6.2 a,c). Thus

flow-driven misalignment of contractile stress fibres inside cells can create a tissue in which cell on average create extensile stress (Fig. 6.2 d).

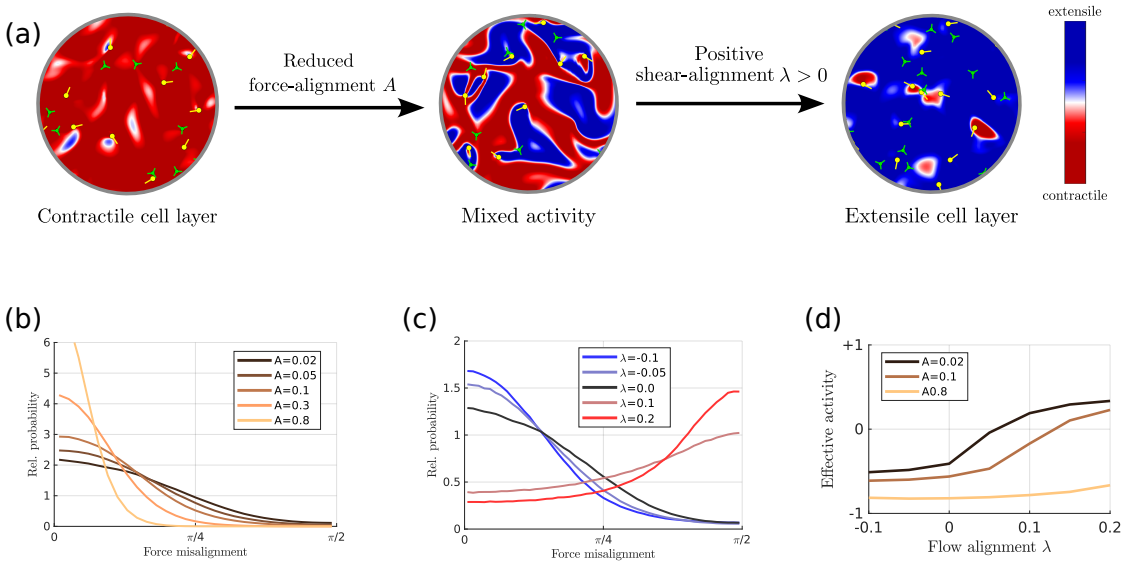


Figure 6.2: **(a)** Different cell parameters can lead to qualitatively different dynamics in cell monolayers. If there is a strong alignment A between stress fibres and cell shape, contractile active turbulence is recovered with just a few small areas where cells have extensile behaviour. Reducing the alignment strength allows larger misalignment between the force and cell shape axis, thereby creating systems of mixed activity. If additionally the cell orientation aligns along the extensional axis of shear flows (positive flow-alignment $\lambda > 0$), contractile cells effectively generate extensile stress ($\theta \approx \pi/2$), so flows and defect dynamics in the monolayer behave like in extensile active nematics. Topological $\pm 1/2$ defects shown in yellow and green for better visibility. **(b,c)** Time-averaged distribution of force-misalignment $p(\theta)$ for different values of alignment strength A and flow-alignment parameter λ. **(d)** Effective activity across cell layers as a function of alignment strength A and flow-alignment parameter λ. The effective activity is defined as the area fraction $\zeta_{\text{eff}} = (A_{ext} - A_{\text{contr}})/A_{\text{tot}}$, where A_{contr} and A_{ext} are the areas where contractile ($\theta < \pi/4$) or extensile ($\theta > \pi/4$) activity is dominant, respectively.

6.4.2 Topological defects

We next investigate the ways in which spatial misalignment patterns are linked to the position of topological defects in the cell orientation field. The numerical results are summarised in Fig. 6.3. Topological defects tend to sit at the interface between extensile and contractile domains which are points of large gradients in misalignment $|\nabla\theta|$ (Fig. 6.3 b). The active stress around $+1/2$ defects in contractile systems generates a flow field which self-propels the defect along the head-to-tail

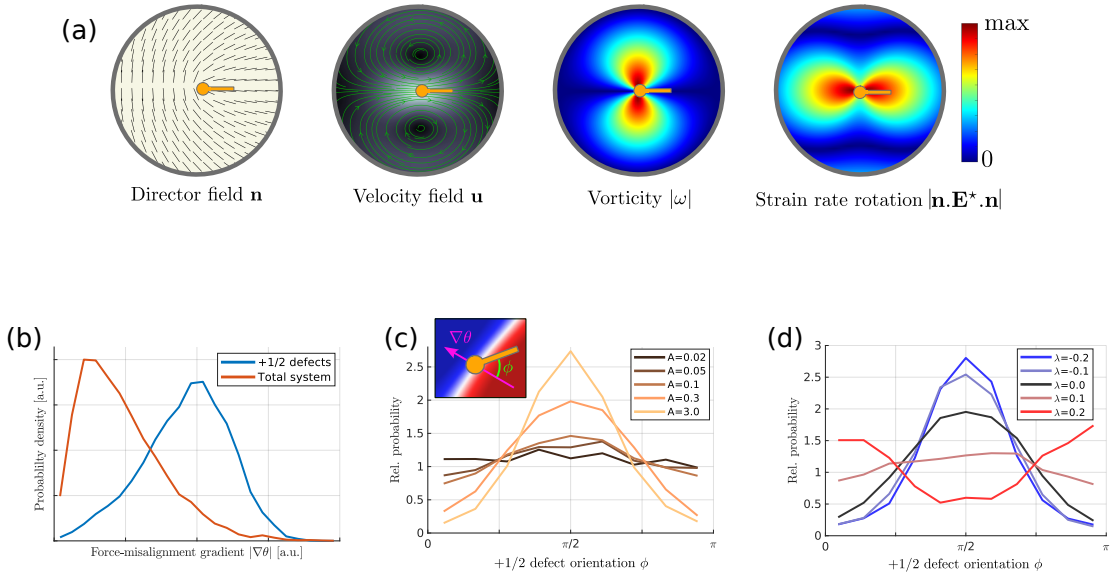


Figure 6.3: **(a)** In the presence of contractile active stress along cell orientations $\mathbf{n}$, $+1/2$ defects generate a unidirectional flow at their centre that causes self-propulsion towards their tail. The flow-field $\mathbf{u}$ around $+1/2$ defects creates a finite vorticity $|\omega|$ and strain rate rotation $|\mathbf{n}.\mathbf{E}^\star, \mathbf{n}|$ (see eqn. 6.4). While vorticity drives force misalignment predominantly at the sides of defects at an angle $\pm\pi/2$, strain rate rotation affects force misalignment in the front and rear of defects at angles $0, \pi$. **(b)** Time-averaged distribution of the force-misalignment gradient $|\nabla\theta|$ across the whole system (orange) and at the position of $+1/2$ defects (blue). Defects preferentially sit at interfaces ($|\nabla\theta| > 0$) between extensile ($\theta = \pi/2$) and contractile ($\theta = 0$) areas. **(c)** Alignment of defects $\mathbf{p}$ with respect to misalignment gradients $\nabla\theta$ for different alignment strength A and fixed $\lambda = 0$. If A is large, misalignment is limited to areas of high vorticity ω, e.g. at at the side of defects. If A is small, there are large areas of misalignment throughout the system (see Fig. 6.2 a) and defect alignment with respect to activity gradients is random. **(d)** Alignment of defects $\mathbf{p}$ with respect to misalignment gradients $\nabla\theta$ for different values of flow-alignment λ and fixed $A = 0.1$. Depending on the sign of λ, strain rate rotation $E^\star$ either promotes ($\lambda > 0$) or suppresses ($\lambda < 0$) force misalignment in the front and rear of defects. Whether defects align perpendicular or parallel with respect to an activity interface is thus controlled by the flow-alignment property λ of cells.

direction. Velocity gradients can be decomposed into an antisymmetric part, the vorticity ω, and a symmetric part, the strain rate $\mathbf{E}$ (Fig. 6.3 a). The flow field around $+1/2$ defects induces strong vorticity at the sides of defects while creating large strain rates at the head and tail regions. From the equations of motion for the misalignment angle θ, eqn. 6.4, it is evident that vorticity ω is a source of misalignment in the system. Thus, for $\lambda = 0$, the growth-rate of misalignment is maximal at the sides of defects, which makes $+1/2$ defects align at a 90° angle with respect to gradients in θ (Fig. 6.3 c). Depending on the sign of the flow-alignment

parameter λ, the term in eqn. 6.4 which contains the strain rate E can either increase or decrease misalignment, thereby promoting or inhibiting misalignment in the head and tail regions of $+1/2$ defects. This makes $+1/2$ defects either align at 90° with respect to $\nabla\theta$ for $\lambda < 0$ or at 0° and 180° for $\lambda > 0$ (Fig. 6.3 d). The alignment mechanism of $+1/2$ defects, however, only works if misalignment of stress fibres relaxes sufficiently fast compared to the time scale of flows in the system. This ensures that areas with $\theta > 0$ coincide with regions where $\dot{\theta} > 0$.

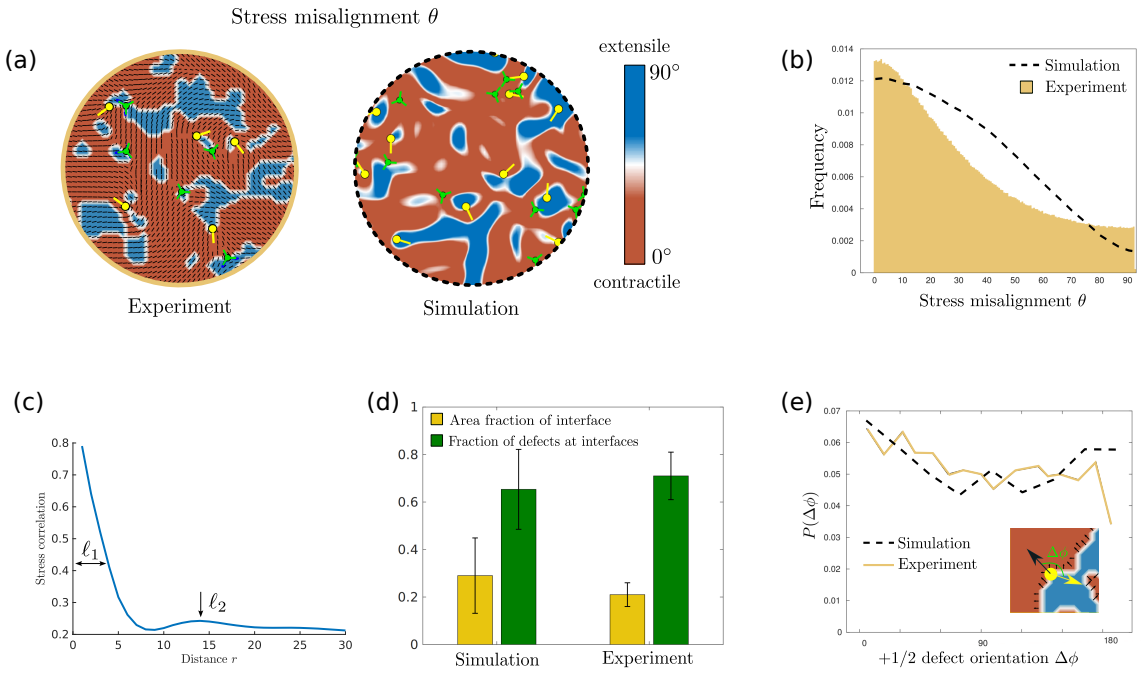


Figure 6.4: **(a)** The director field of cell orientation **n** features many $\pm 1/2$ defects (left) which preferentially sit at the boundary of extensile domains. **(b)** Time-averaged distribution of stress fibre misalignment θ in simulations (black, dashed line) compared to experiments (yellow). **(c)** The radial correlation function $\langle \zeta(x_0)\zeta(x_0 + r)\rangle$ shows two distinct length-scales, with ℓ_1, ℓ_2 quantifying the average size and separation of extensile domains, respectively. **(d)** Comparison between the area fraction of interface domains and fraction of defects within interface domains in simulations and experiments. Interface domains are defined as points which are less than $\ell_1/7$ lattice units away from an extensile-contractile interface. Error bars show the standard deviation of quantities over time. **(e)** Time-averaged distribution of the angle between the orientation of $+1/2$ defects and the normal vector of interfaces between extensile and contractile domains in simulations (black, dashed line) and experiments (yellow, solid line).

6.4.3 Comparison to biological experiments

Simultaneous measurements of cell-generated forces and cell orientations in MDCK monolayers reveal spatially correlated domains of significant force misalignment, $\theta > 45°$, which qualitatively follow spatial patterns observed in the continuum tissue model (Fig. 6.4 a,b). The radial correlation function $\langle\zeta(x_0)\zeta(x_0+r)\rangle$, where $\zeta = -1$ for $\theta < 45°$ and $\zeta = +1$ for $\theta > 45°$, confirms that misaligned domains form ordered patterns with a specific length-scale ℓ_1 (Fig. 6.4 c). To quantitatively compare the behaviour of defects in simulations and experiments, we divide the system into bulk and interface domains, where interface domains are defined in terms of the characteristic length-scale ℓ_1. In experiments we find that most defects are located at the interface of extensile domains (Fig. 6.4 d) with no preferential alignment of $+1/2$ defects with respect to interfaces (Fig. 6.4 e). This indicates that the alignment strength A of stress fibres is indeed quite small for MDCK cells.

6.5 Summary and Discussion

In this last chapter we have extended the active nematic continuum model to allow for misalignment between the cell orientation the axis along active stress is generated. Decoupling the orientational dynamics of cell shape and sub-cellular stress fibres gives rise to dynamic, spatially correlated domains in which active stress shows significant misalignment with respect to cell orientation. Since the misalignment of stress fibres is driven by flow-induced rotation of the cell orientation, misalignment patterns are linked to the positions of topological defects in the cell orientation field, which are points of large flow gradients.

The time scale over which actomyosin stress fibres reorganise inside cells was estimated to be on the order of several hours, $\tau_\theta \sim (\Gamma A)^{-1} \sim 5h$ [158]. We can estimate the time scale of flow-driven reorientation of cells τ_u by comparing the magnitude of cell flows u to the size of individual cells L. Considering that cell flows around $+1/2$ defects typically reach $\sim 20\mu m/h$ [30, 155] and a typical MDCK cell size is $\sim 10\mu m$, we obtain $\tau_u \sim L/u \sim 0.5h$. We therefore expect that flows in

MDCK layers are reorienting cells faster than stress fibres can reorganise, $\tau_u < \tau_\theta$, which would explain the observed misalignment patterns around topological defects.

If reorganisation of stress fibres is sufficiently small, $\tau_u < \tau_\theta$, positive flow-alignment $\lambda > 0$ can bias systems to predominantly form extensile domains in which stress fibres are maximally misaligned, $\theta = 90°$. This implies that cells which generate contractile forces in equilibrium, $\theta = 0°$, can form extensile cell layers under the right conditions.

In fact, it is known that MDCK epithelial layers can change from extensile to contractile active nematic behaviour in the absence of E-cadherin, which weakens the adhesion strength between cells. This behaviour has been explained in previous work by a competition between intracellular contractile stress due to stress fibres and intercellular extensile stress due to neighbour interactions [155]. Assuming extensile behaviour in MDCK layers is caused by misaligned stress fibres rather than exotic cell-cell interactions, weakening the force transmission between cells should reduce drag forces between neighbours, thus gradients in cell flows change cell orientations less efficiently. This, in turn, increases the flow-driven reorientation time of cells, $\tau_u \gtrapprox \tau_\theta$, which reduces stress fibre misalignment and makes the layer behave in more contractile way.

Take-home message:

If cell shapes are more quickly changed by the motion of neighbouring cells than the orientation of sub-cellular stress fibres, tissue-scale flows promote misalignment of active forces with respect to the cell shape orientation. This can create tissues which are contractile in some areas but extensile in others.

7 Discussion

In this thesis, we explored various aspects of how active stresses can give rise to collective motion in living matter systems, ranging from self-deforming aggregates to growth-induced cell alignment inside spheroids and defect-mediated misalignment of active forces in cell monolayers. We summarise the main findings in section 7.1 and provide an outlook for ongoing and future research in section 7.2.

7.1 Summary

In chapter 3 we investigated the behaviour of three-dimensional active nematic fluids that are confined by a soft interface. We found that gradients in active stress across the interface drive flows, which re-align the director field close to the surface of droplets. This creates an effective anchoring force, termed *active anchoring*, which leads to in-plane or normal surface alignment in extensile or contractile systems, respectively. Active anchoring also has important consequences for the dynamics of disclination lines close to the interface, such as the preferential formation of wedge-like surface disclinations in extensile systems or the creation of in-plane aligned stripes connecting twist-like surface disclination in contractile systems. If surface tension is sufficiently low, active forces induced by the director alignment and disclination line structures in turn trigger the formation of finger-like

protrusions in extensile droplets and the creation of surface wrinkles and droplet invagination in contractile systems. We identified an active length-scale ℓ_ζ of three-dimensional active turbulence, which controls both the density of disclination lines inside droplets, and the correlation length of the twist angle β along lines. We found that the morphologies of droplets are determined by two dimensionless control parameters: $A \sim \sqrt{R/\ell_\zeta}$, the ratio of droplet size to active length-scale, and $\Psi \sim K_{LC}/K_\varphi$, the ratio of nematic elastic constant to surface tension coefficient.

In chapter 4 we explored how spatial variations of active stress affect flows and defect dynamics in two- and three-dimensional bulk systems. We found that activity gradients drive flows which can align the director field either parallel or perpendicular to the gradient direction. Activity gradients generate active torques on defects and disclination lines, which affect their average orientation in the regime of active turbulence. In two-dimensional systems, active torques align the orientation of $+1/2$ defects parallel to the gradient direction. In three-dimensional nematics, disclination lines preferentially lie in the plane perpendicular to activity gradients, with their line tangent pointing perpendicular to the gradient direction. Wedge-like $+1/2$ defects, in the plane perpendicular to the line tangent, preferentially align parallel to activity gradients, while twist-type defects tend to align anti-parallel.

We then applied the theory of active nematics to 3D multicellular spheroids in chapter 5. Because cells need access to sufficient metabolites, such as nutrients or oxygen, in order to grow and divide, cells near the surface of spheroids proliferate more rapidly than those in the resource-depleted core. Using both analytical arguments and numerical simulations, we found that proliferation gradients inside spheroids set up radial flows and activity gradients, both of which can potentially align the orientation axis of cells inside the aggregates. We identified three distinct regimes of cell alignment: (i) Global radial cell alignment. (ii) Global tangential cell alignment. (iii) Tangential cell alignment close to the surface and radial alignment in the core. Comparing our results to experimentally measured cell alignment profiles allowed us to infer the active stress ζ and flow-alignment parameter ξ for freely

grown aggregates of human colon carcinoma cells (HCT116), colon adenocarcinoma cells (HT29) and human breast cancer cells (BC52).

In the last chapter 6 we relaxed the assumption that cell-generated forces are always directed along the major principal axis of cell shapes. By decoupling the orientational dynamics of cell shapes and the sub-cellular active stress fibres, we investigated the interplay between cell orientations, flows and active forces in two-dimensional cell monolayers. We showed that misalignment between cell orientations and active forces is linked to topological defects in the cell orientation field, both in simulations and experiments. This challenges the conventional belief that cells in a tissue generate either predominantly contractile or extensile forces, and shows that the type of cell-generated active stress can vary continuously across tissues.

7.2 Outlook

Active hydrodynamic models, which incorporate key biological features such as cell-generated active forces, cell division and death, are increasingly used to describe biological tissues and are now becoming a standard approach in developmental biology. In this thesis we have touched upon new aspects in this field. However, there are still many open research questions; in particular:

How does cellular heterogeneity and cell differentiation in cell aggregates affect morphogenesis?

An important aspect when considering cellular aggregates, such as embryos or tumours, is that these cell populations are often heterogeneous and are composed of phenotypically distinct sub-populations with different mechanical properties and cellular responses [159]. The distribution of sub-populations in growing systems can also evolve over time due to cell differentiation, the process by which cells change from one cell type to another. It would be interesting to study the organisation and flows of cellular aggregates consisting of two or more distinct phases, each having different mechanical properties and activity levels, and including transition rates between phases. First progress has been made recently by extending active

nematic hydrodynamics to two-fluid mixtures with separate velocity fields for each fluid component [160]. Although this study focused on micro-phase separation in active-passive bulk tissues, it would be interesting to extend this approach to three-dimensional growing systems in order to explore morphogenesis in the presence of cell differentiation.

Can sptiotemporal activity patterns be used to guide tissue morphology?

Recent experimental and theoretical work has shown that the chaotic flows of active turbulence in two-dimensional bulk systems can be controlled without having to confine the system. This was achieved by spatially structured activity in light-activated actin-myosin mixtures [118] or spatiotemporal variations of applied vorticity or activity strength in simulations using optimal control theory [161]. It would be interesting to investigate in more detail in the future how spatiotemporal activity patterns $\zeta(\mathbf{x}, t)$ could be used to control the shape of active droplets, analogous to the natural course of morphogenetic events, which are controlled by spatiotemporal patterns of biochemical signals.

How does viscoelasticity affect tissue dynamics?

Another important aspect in living matter is viscoelasticity. In this thesis we have focused on tissue dynamics in the hydrodynamic limit, where cell aggregates are modelled as a viscous fluid on long time scales. However, recent studies of two-dimensional systems revealed that tissue viscoelasticity could lead to new phenomena, such as self-sustained oscillations and flow reversals in active nematic channels [162, 163].

A promising avenue for future research would be the study of three-dimensional viscoelastic cell aggregates involving an elastic response on time scales smaller than a characteristic relaxation time τ. The viscoelastic relaxation time of cell aggregates, which is typically on the order of $\tau \approx 5 - 40$ min [90, 98], is much smaller than typical cell-cycle times of $T_C \approx 20$ h, thus elastic contributions should be negligible on the time scales of freely grown multicellular spheroids. However,

cell compressibility and elasticity become important when aggregates are subject to fast environmental changes, such as external pressure jumps [43, 45, 164].

However, cells are not the only components that make tissues viscoelastic. The space between cells is usually filled by a dense network of macromolecules, the extracellular matrix, which is known to strongly affect the migratory behaviour of cells [165, 166]. The structural support provided by this viscoelastic matrix that encloses cell aggregates can stabilise their shape by slowing down hydrodynamic instabilities [167], which could potentially lead to new and interesting morphologies.

When growing aggregates are confined by elastic surroundings, the build-up of compressive stress inside aggregates can also significantly affect the cell proliferation rate. When cell-generated forces are insufficient to create space for mitotic elongation, mitosis fails [150]. The cell division rate inside spheroids thus decreases with increasing compressive stress [44, 168]. This should limit the maximum rate at which cell aggregates can grow in viscoelastic environments.

Can active stress help aggregates to overcome diffusion-limited growth?

In chapter 5 we have investigated growing spheroids which reached a steady state at a critical radius, $\dot{R} = 0$, because metabolites have a finite penetration length ℓ_m from the surface of spheroids. For sufficiently small surface tension, however, active forces strongly deform spherical aggregates and metabolites can more easily penetrate aggregates due to the enlarged surface area. This increases the total cell production rate and the aggregate starts to grow again, $\dot{R} > 0$. This could be a potential mechanism for avascular, spherical tumours to overcome diffusion-limited growth using active forces. Preliminary results of ongoing work reveal that proliferating spheroids form growing protrusions above a certain activity level, creating a branched network structure that can grow indefinitely in environments with an unlimited supply of nutrients.

We have proposed several future research directions, including exploration of how cellular heterogeneity, spatiotemporal variation of active stress and viscoelasticity influence tissue organisation. Active matter is a rapidly developing field of research and it will be interesting to see to what extent the ideas of active continuum theories will contribute to the understanding of mechanobiology in the coming years.

Appendices

A

The hybrid lattice Boltzmann algorithm

In this thesis we numerically solve the Navier-Stokes equations 2.2 and continuity equation 2.1 for the flow field using a lattice Boltzmann algorithm, while the Cahn-Hilliard equation for φ, the Beris-Edwards equation for $\mathbf{Q}$ 2.18 and the equations of motion for the metabolite concentration m and force misalignment angle θ are solved using a finite difference method. This approach was first put forward by Marenduzzo et al. [67] and has since been widely used in the community.

A.1 Background

The Boltzmann equation and Navier-Stokes equations are two different approaches for describing fluid flow. The Boltzmann equation is a microscopic description of a fluid, which describes how density and velocity distributions of particles evolve over time due to collisions between individual particles. The Navier-Stokes equations, on the other hand, are a set of partial differential equations that describe the macroscopic behaviour of fluids in terms of a coarse-grained velocity field $\mathbf{u}$. The Navier-Stokes equations can be derived from the Boltzmann equation under certain conditions, such as the assumption of local thermodynamic equilibrium. The lattice Boltzmann method makes use of this connection by solving a discretised Boltzmann

equation on a grid, which offers several advantages over solving the Navier-Stokes equations directly, including higher numerical stability and computational efficiency.

A.2 The lattice Boltzmann equation

The distribution function $f(\mathbf{x}, \mathbf{v}, t)$ at position $\mathbf{x}$ represents the density of particles with a certain velocity $\mathbf{v}$ at a certain point in time t. In the lattice Boltzmann (LB) algorithm, the distribution function is only defined at discrete lattice sites with spacing Δx and at discrete times with time step Δt. We also discretize the velocity by decomposing the distribution function $f(\mathbf{x}, \mathbf{v}, t)$ into a set of distribution functions $\{f_i(\mathbf{x}, t)\}$, where index i labels a specific lattice direction. The fluid density ρ is related to the distribution function by

$$\rho(\mathbf{x}, t) = \sum_i f_i(\mathbf{x}, t) \, . \tag{A.1}$$

Each lattice direction i is associated with a velocity vector $\mathbf{e}_i$. In the D3Q15 velocity vector lattice, the velocity vectors are $\mathbf{e}_i = (0,0,0)$, $(\pm 1,0,0)$, $(0,\pm 1,0)$, $(0,0,\pm 1)$ and $(\pm 1,\pm 1,\pm 1)$ (see Fig. A.1). The fluid momentum is then given by

$$\rho \mathbf{u} = \sum_i f_i \mathbf{e}_i \, . \tag{A.2}$$

The set of distribution functions $f_i(\mathbf{x}, t)$ evolves over a time step Δt according to

$$f_i(\mathbf{x} + \mathbf{e}_i \Delta t, t + \Delta t) = f_i(\mathbf{x}, t) + \Delta t \, C_f(\mathbf{x}, t) \, , \tag{A.3}$$

where C_f is a collision operator. This time evolution includes two steps: free streaming with velocity $\mathbf{e}_i$ (first term, right hand side) and a collision step (second term, right hand side). In the streaming step, the distribution functions just move towards neighbouring grid positions. In the collision step, the distributions f_i relax towards a set of equilibrium distributions f_i^{eq} over a relaxation time τ,

$$C_f(\mathbf{x}, t) = -\frac{1}{\tau} \left(f_i - f_i^{eq} \right) + p_i(\mathbf{x}, t) \, , \tag{A.4}$$

where the forcing term p_i contains additional body forces, such as friction or off-diagonal stress terms. It should be noted, that there are many other collision

operators C_f available in the literature. In this thesis, we use the simplest collision operator that can be used for Navier-Stokes simulations, which is the Bhatnagar-Gross-Krook (BGK) collision operator (eqn. A.4). To ensure that solving eqn. A.3 actually yields solutions of the Navier-Stokes equation 2.2, the equilibrium distributions f_i^{eq} are constrained by

$$\sum_i f_i^{eq} = \rho, \quad \sum_i \mathbf{e}_i f_i^{eq} = \rho\mathbf{u}, \quad \sum_i \mathbf{e}_i\mathbf{e}_i f_i^{eq} = -\sigma + \rho\mathbf{u}\mathbf{u}\,, \tag{A.5}$$

where σ is the symmetric part of the stress tensor $\mathbf{\Pi}$ in the Navier-Stokes equation 2.2. While the zeroth and first moment of f_i^{eq} ensure that mass and momentum are conserved, the second moment describes momentum dissipation and contains the viscous stress $\mathbf{\Pi}^{visc}$ (eqn. 2.3), as well as the symmetric parts of the active stress $\mathbf{\Pi}^{act}$ (eqn. 2.25), elastic stress $\mathbf{\Pi}^{el}$ (eqn. 2.16) and capillary stress $\mathbf{\Pi}^{cap}$ (eqn. 2.6). The antisymmetric part of the stress tensor are added as body forces in eqn. A.4. Using these constraints, eqn. A.3 can be mapped into eqn. 2.2 using the Chapman-Enskog analysis [68, 169]. The advantages of using LB is that eqn. A.3 has second-order accuracy in lattice spacing and time step, while being a first-order solving scheme. This allows us to do a rather accurate computation on larger systems with an acceptable computation time.

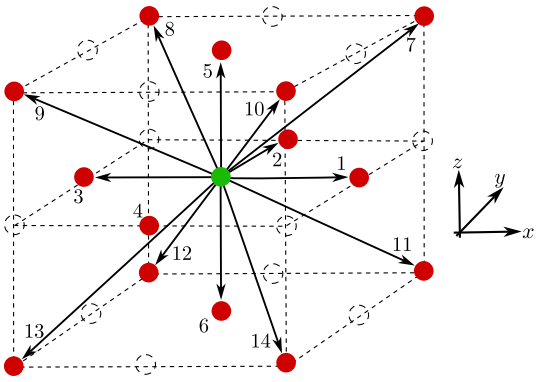


Figure A.1: Lattice geometry and lattice vectors used in the D3Q15 lattice Boltzmann model. The green node corresponds to the null vector.

To model cell division and death inside proliferating spheroids in chapter 5, we add mass sources and sinks to the fluid $\nabla \cdot \mathbf{u} = k_p$. This can be accounted for in LB by adding a particle source term S_i to eqn. A.3, which represents particles being

added or removed from the distribution functions $f_i(\mathbf{x}, t)$. For source monopoles, we can assume that the velocity distribution of added particles is at equilibrium [169]. We validate this method by comparing numerical LB predictions of converging cell flows inside spheroids to analytical solutions (Fig. A.2).

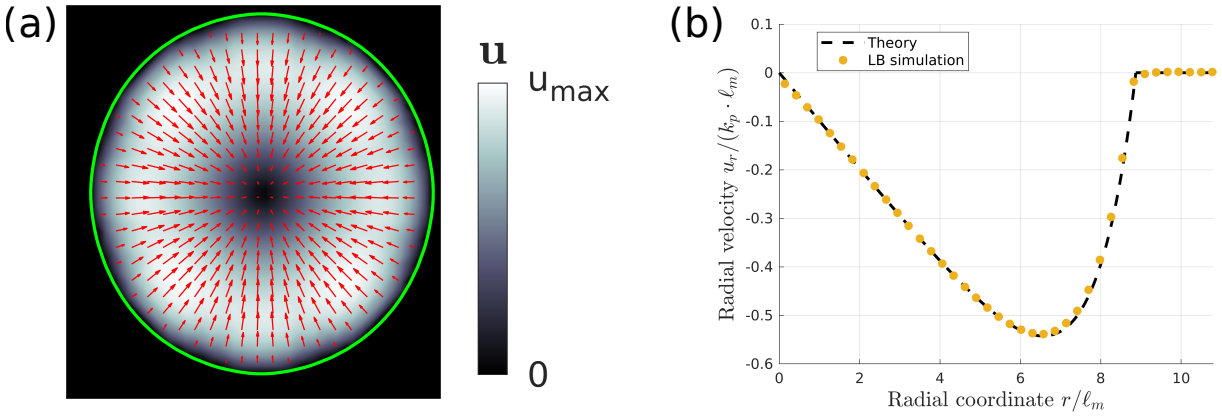


Figure A.2: **(a)** Snapshot of the velocity field $\mathbf{u}$ inside a steady-state cell aggregate as described in section 5.4 using the hybrid LB-finite difference method. **(b)** Comparison between radial velocity field u_r obtained in LB simulations (orange) and analytical solutions (black, dotted line) following eqn. 5.9. We validated that in the absence of sources and sinks in the continuity equation, $\nabla \cdot \mathbf{u} = 0$, the flow fields obtained from the lattice-Boltzmann solver remain incompressible, with density fluctuations $\delta\rho/\rho < 0.03$.

A.3 Finite-difference method

The equations of motion for the concentration field φ (eqn. 2.4) and the nematic order parameter $\mathbf{Q}$ (eqn. 2.18) are solved using a simple finite difference scheme,

$$\varphi(\mathbf{x}, t + \Delta t) = \varphi(\mathbf{x}, t) + \Delta t \left(\Gamma_\varphi \nabla^2 \mu - \partial_i (u_i \varphi) \right) , \tag{A.6}$$

$$Q_{ij}(\mathbf{x}, t + \Delta t) = Q_{ij}(\mathbf{x}, t) + \Delta t \left(\mathcal{W}_{ij} + \Gamma_{LC} H_{ij} - (u_k \partial_k) Q_{ij} \right) , \tag{A.7}$$

where we use second-order finite difference methods to evaluate spatial derivatives. The equations of motion for the metabolite concentration m (eqn. 5.2) and force misalignment angle θ (eqn. 6.4) are solved in a similar manner.

Compared to the full D3Q15 lattice Boltzmann approach, where all variables are described by a set of fifteen distribution functions, the hybrid method reduces computational costs significantly since now only one set of distribution functions

plus the values of φ and the five independent components of the $\mathbf{Q}$-tensor are needed. Also, this approach avoids error terms which arise from connecting the lattice Boltzmann model to the tensorial order parameter [170].

B

Detection of topological defects and disclination lines

B.1 2D topological defects

To detect the positions of topological defect we use Zapotoky's defect-finding for two-dimensional systems [171]. Topological defects on a two-dimensional square grid are detected by calculating the winding number for all sets of neighbouring lattice points which form a two-by-two square. If the director changes its orientation by $\pm\pi$ when stepping along the four lattice sites in the clockwise direction, we define the position of $\pm 1/2$ at the intersection of the four lattice sites.

B.2 3D disclination lines

To find defect positions on a three-dimensional grid, we use an extended version of Zapotoky's two-dimensional algorithm. The extended algorithm checks if a disclination is located at a given position by performing the two-dimensional calculation on all sets of four lattice sites forming a two-by-two square in all three coordinate planes [172] (see Fig. B.1). When a disclination is found, its rotation vector $\mathbf{\Omega}$ is determined by summing over the cross product of each pair of directors around it. Once all grid points have been classified, defect positions are sorted to

form continuous disclination lines, which we then use to calculate the tangent vector **L** (see Fig. B.2). The angle between the local line tangent **L** and the rotation vector **Ω** is the twist angle β. A shortcoming of this algorithm is that **Ω** has an arbitrary sign, hence it cannot directly distinguish between $\beta = 0$ $(-1/2)$ and $\beta = \pi$ $(+1/2)$ disclinations. To distinguish those, we calculate the saddle-splay energy

$$\bar{f}_{24} = \nabla \cdot [(\mathbf{n} \cdot \nabla)\mathbf{n} - \mathbf{n}(\nabla \cdot \mathbf{n})] \ , \tag{B.1}$$

which is negative at a $\beta = \pi$ disclination line segment, positive at a $\beta = 0$ segment, and zero for a local twist profile [173]. This algorithm agrees well with other non-local methods, which compute **Ω** from the director **n** in a larger circuit around the disclination core [37].

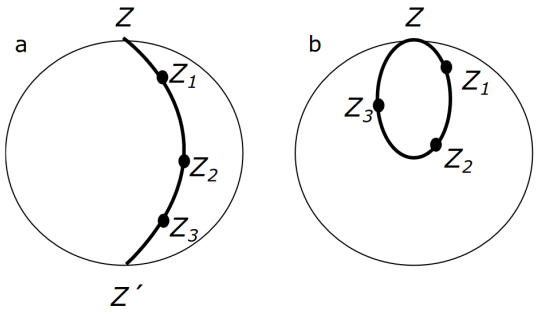


Figure B.1: Representation of a director **n** on the unit sphere. The head-less director has two equivalent projections **n** and $-\mathbf{n}$. When moving around a two-by-two lattice square, we define the first director as the origin Z on the upper half sphere and then move to the position Z_1 of the director on the next lattice site, where we always take the new director projection with the smallest angle difference to the previous one. This yields a closed walk to from $Z \to Z_1 \to Z_2 \to Z_3$ and then either back to Z (b) or to its equivalent point Z' on the lower half sphere (a). If we ended up at Z', a half-integer disclination passed through the four lattice sites. Image adapted from [171].

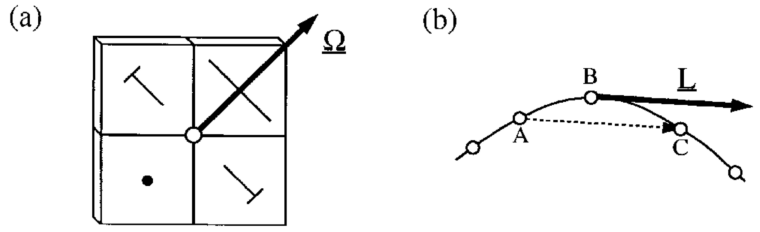


Figure B.2: (a) Example of detecting a twist-defect at the intersection of four lattice sites. The rotation vector $\mathbf{\Omega}$ is calculated by summing over the four cross products of each director pair around the disclination. **(b)** After grouping disclination points into distinct lines, the local line tangent $\mathbf{L}$ at point B is calculated by taking the displacement vector between the nearest neighbours A and C. Image taken from [172].

Limitations

The colour jumps seen for some disclination line segments occur, because the calculation of the local line tangent is performed on a discrete grid, hence the tangent vector does not vary continuously along a disclination line, especially at points of large curvature. This can sometimes create sudden jumps in the twist-angle β. Another error source is that the algorithm cannot always clearly distinguish between $+1/2$ and $-1/2$-type disclination lines if the saddle-splay energy is close to zero. Both of these error sources are relatively small and do not significantly affect defect statistics. The discretization error of the line tangent results in small jumps, $\Delta\cos(\beta) < 0.2$, and the misclassification of $\pm 1/2$ line segments are rare events ($< 5\%$).

C

Additional information and measurements

C.1 Phase-field modelling of biological membranes

The elasticity of a two-dimensional cell membrane is usually described by the following curvature energy proposed by Helfrich [86]:

$$\mathcal{F}_{mem} = \kappa/2 \int (C - C_0)^2 \, dA + \kappa_G \int G dA + \gamma \int dA \,, \tag{C.1}$$

where $C = (c_1 + c_2)$ and $G = c_1 c_2$ are the total and Gaussian curvatures of the membrane, given in terms of the principal curvatures c_1 and c_2. κ and κ_G are the bending rigidity and saddle-splay modulus, respectively, C_0 is the spontaneous curvature caused by any asymmetry in the membrane structure, and γ is the surface tension. In our model we consider a smooth concentration field φ associated with a Landau free energy density $f_{mem}[\varphi] = f_b + f_{st}$ to model the mechanical properties of an interface. The first part of our Landau free energy includes the membrane bending energy:

$$f_b = \frac{\kappa^*}{2} \left(-\varphi + \varphi^3 - \epsilon^2 \nabla^2 \varphi \right)^2 . \tag{C.2}$$

This free energy can be minimised analytically along the surface normal direction z in equilibrium, resulting in a smooth concentration profile, $\varphi_0(z) = \tanh(z/\ell)$,

which connects phases $\varphi = -1$ and $\varphi = +1$ over a characteristic width $\ell = \sqrt{2}\epsilon$. Given the analytical solution $\varphi_0(z)$, we can compare the free energies of the phase-field representation and classical Helfrich theory to obtaining a mapping between model parameters [49],

$$\gamma = 0\ ,\ C_0 = 0\ ,\ \kappa_G = 0\ ,\ \kappa = \frac{2\epsilon^3}{3\sqrt{2}}\kappa^*\ , \tag{C.3}$$

which includes only a bending contribution ($\kappa > 0$) of the membrane. To include surface tension, we need to add the following term to the free energy:

$$f_{st} = \frac{K_\varphi}{2}(\nabla\varphi)^2. \tag{C.4}$$

It should be noted that the shape of $\varphi_0(z)$ coincides with the equilibrium profile of the well-known Cahn–Hilliard equation, which is used to describe phase-separation in systems without bending rigidity. If the interface is narrow, $(\nabla\varphi_0)^2$ behaves as a δ-function, $\lim_{\ell\to 0}\frac{3}{4\ell}\mathrm{sech}^4(z/\ell) = \delta(z)$, and the volume integral over f_{st} converges to a surface integral over the interface,

$$\gamma\int dA = \gamma\int \delta(z-z')\,dV \approx \frac{3\ell}{4}\gamma\int(\nabla\varphi_0)^2 dV\ , \tag{C.5}$$

where z' is the position of the interface. Thus, the membrane surface tension is related to the phase-field parameters via $\gamma = \frac{2K_\varphi}{3\ell}$, where $\ell = \sqrt{2}\epsilon$ is width of the membrane. However, it should be noted that this equation is only valid as long as the bending term f_b is dominant and ϵ sets the length-scale of the membrane width. If the surface tension term f_{st} is dominant ($K_\varphi/\kappa^* > \epsilon^2$), the characteristic width of the equilibrium concentration profile $\varphi_0(z)$ is given by $\ell \sim \sqrt{K_\varphi/\kappa^*}$, and thus the surface tension scales as $\gamma \sim \sqrt{K_\varphi}$.

Using phase-field theories to model droplets and membranes does not necessarily mean, that the interface width ℓ must be on the same scale as the width of the physical interface. It is sufficient to ensure that ℓ is much smaller than any other length scales in the system, such as the active length-scale ℓ_ζ or droplet size R. Finally, the higher order derivatives of the phase-field φ, which show up in the bending free energy f_b, give rise to additional terms in the capillary stress tensor

$$\mathbf{\Pi}^{cap} = (f-\mu\varphi)\mathbf{I} - \nabla\varphi\left(\frac{\partial f}{\partial(\nabla\varphi)}\right) + \nabla\varphi\nabla\left(\frac{\partial f}{\partial(\nabla^2\varphi)}\right) - \nabla\nabla\varphi\left(\frac{\partial f}{\partial(\nabla^2\varphi)}\right)\ . \tag{C.6}$$

C.2 Active and passive torques acting on defects

To calculate active and elastic torques on defects, we first obtain the hydrodynamical force density F_i from the respective stress tensor,

$$F_i = \partial_j \Pi_{ij} \ , \tag{C.7}$$

where we use $\Pi_{ij} = \Pi_{ij}^{el}$ for elastic forces and $\Pi_{ij} = \Pi_{ij}^{act}$ for active forces. The torque $\mathbf{\Gamma}$ on defects is then calculated by integrating over forces in the vicinity of defects,

$$\Gamma_i = \int \epsilon_{ijk} F_j r_k \, dV \ , \tag{C.8}$$

where the origin of the coordinate system r_k is located at the centre of defects. We perform the integration over a circular domain $r < r_c$ around the defect core, where the cut-off radius r_c is chosen as the average separation between defects. In 3D systems, active and elastic torques acting on disclination line segments are calculated by integrating forces within a cylindrical domain which extends along the line tangent of disclination lines.

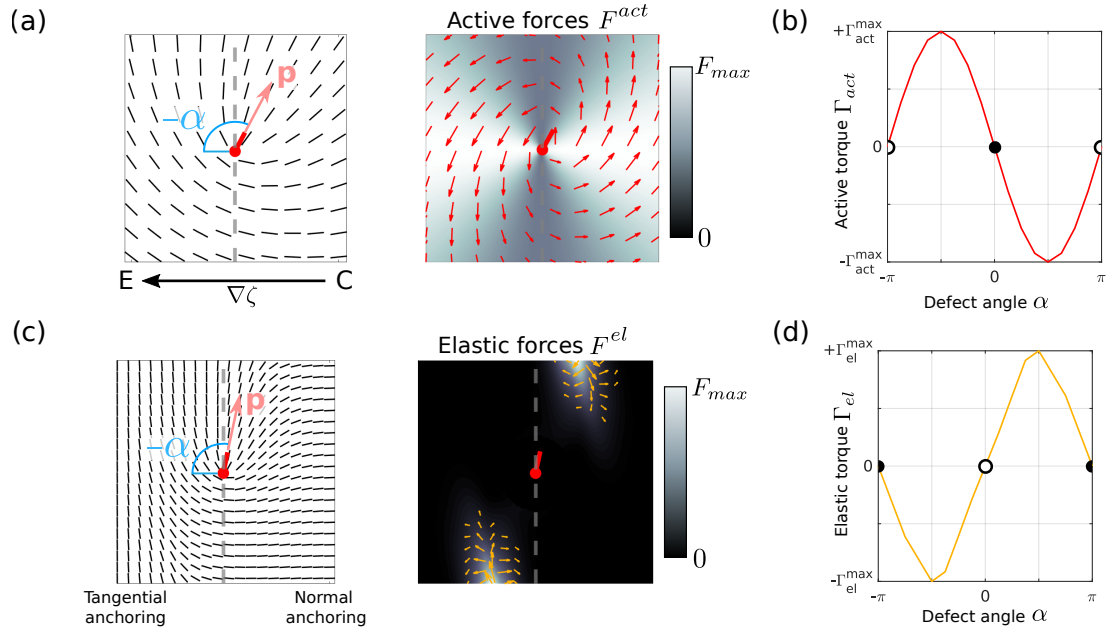


Figure C.1: **(a)** Director field (left) and active forces (right) of a $+1/2$ defect with orientation $\mathbf{p}$ at a finite angle α with respect to an activity gradient $\nabla\zeta$ (negative sign indicates clockwise rotation). **(b)** Active forces F^{act} create a torque $\Gamma_{act} \sim \mathbf{p} \times \nabla\zeta$ on the defect, which reaches a maximum at $\alpha = \pm\pi/2$ and vanishes for $\alpha = 0, \pi$. Active torques thus align $+1/2$ defects parallel to activity gradients, which is evident from the stable fixed-point at $\alpha = 0$. The magnitude of active torque Γ^{max}_{act} depends on the specific activity profile in the vicinity of defects, but generally scales with the magnitude of activity gradients, $\Gamma^{max}_{act} \sim \zeta_{max}$. **(c)** Director field (left) and elastic forces (right) of a $+1/2$ defect with orientation $\mathbf{p}$ at a finite angle α with respect to planar boundary conditions set up by the effective anchoring force, favouring normal anchoring on the contractile side and tangential anchoring on the extensile side of activity interfaces. **(d)** Elastic forces F^{el}, which are strongest at points of large bend or splay distortions, create an elastic torque Γ_{el} on the defect, which reaches a maximum at $\alpha = \pm\pi/2$ and gives rise to a stable fixed point at $\alpha = \pi$. Elastic forces thus align $+1/2$ defects anti-parallel to activity gradients. The magnitude of elastic torque Γ^{max}_{el} depends on the specific distortion profile around defects, but generally scales with the magnitude of the elastic energy f_{el}, $\Gamma^{max}_{el} \sim K_{el}$. Active and elastic forces were calculated from Π^{act} and Π^{el}, respectively, using a fixed director field $\mathbf{Q}$ on a 2D lattice of size 100×100.

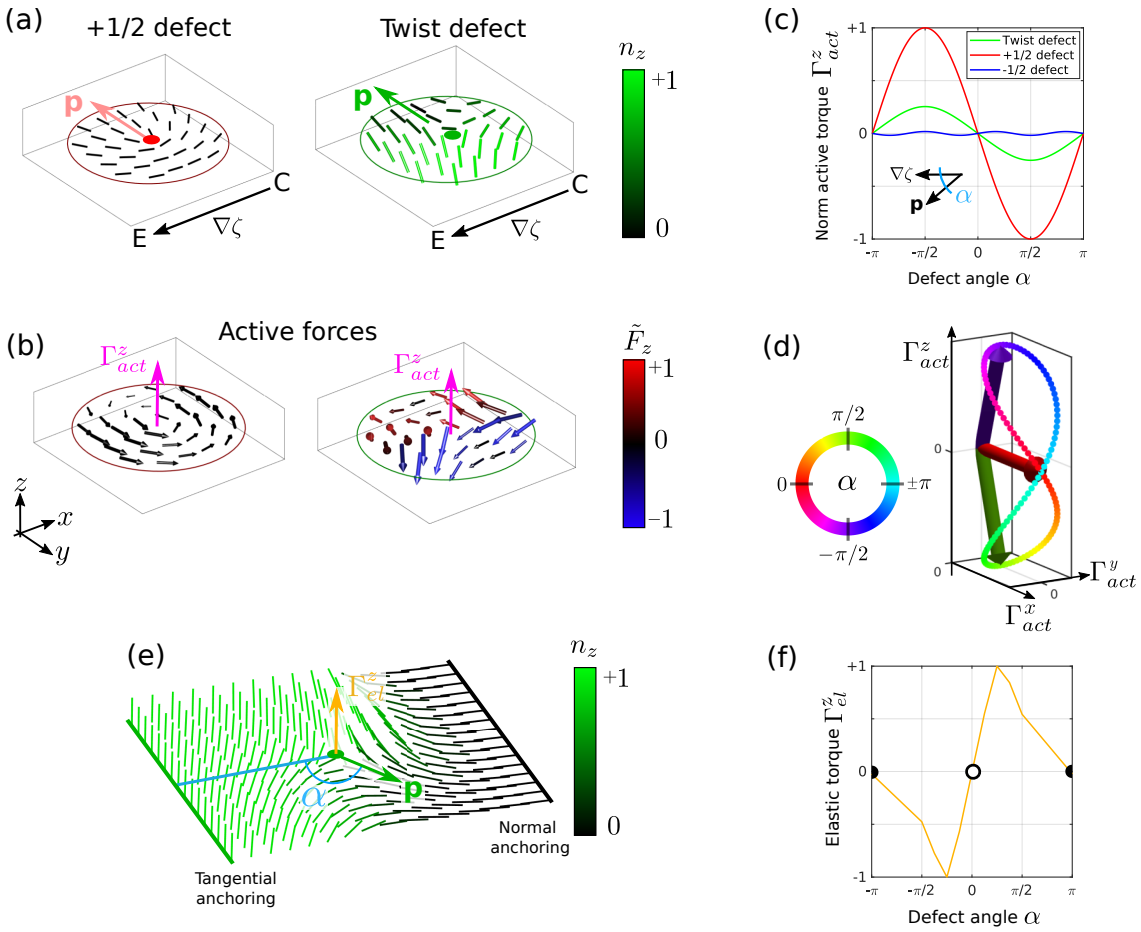


Figure C.2: **(a)** Director fields of a $+1/2$ (left) and radial twist disclination (right) with orientation $\mathbf{p}$ and an applied activity gradient $\nabla\zeta$. While $+1/2$ disclinations are quasi-2D, the director field around twist disclinations features out-of-plane components n_z. **(b)** Active forces around $+1/2$ disclinations (black arrows) are confined to the defect plane (xy) and produce a torque $\Gamma_{act} \sim \mathbf{p} \times \nabla\zeta$ along the z-axis (pink arrow), which rotates the defect orientation $\mathbf{p}$. Active forces around twist disclinations feature out-of-plane components F_z (see colour bar), creating an active torque Γ_{act} which does not strictly point along the z-axis. The in-plane defect orientation $\mathbf{p}$ is only affected by component Γ^z_{act}, while components Γ^x_{act} and Γ^y_{act} change the overall direction of the defect line. **(c)** Active torque Γ^z_{act} as a function of angle α between defect direction $\mathbf{p}$ and activity gradient $\nabla\zeta$ for different defect types. Like in 2D, active torques align defect orientations $\mathbf{p}$ parallel to activity gradients ($\alpha = 0$). The orientation $\mathbf{p}$ of twist defects, however, is much less affected by active torques compared to $+1/2$ defects. **(d)** The active torque vector Γ_{act} on twist defects changes direction as a function of defect angle α. The magnitude of the z-component Γ^z_{act} reaches a maximum for $\alpha = \pm\pi/2$, while the out-of-plane component Γ^x_{act}, which points along the gradient direction, peaks at $\alpha = 0, \pi$, where its sign depends on the chirality of the twist defect. **(e)** Director field of a twist defect with orientation $\mathbf{p}$ at a finite angle α with respect to boundary conditions set up by the effective anchoring force, favouring normal and tangential anchoring on the contractile and extensile side, respectively. **(f)** Elastic forces in the defect plane create an elastic torque Γ^z_{el} which aligns twist defects anti-parallel to activity gradients. Active and elastic forces were calculated from Π^{act} and Π^{el}, respectively, using a fixed director field $\mathbf{Q}$ on a 3D lattice of size $100 \times 100 \times 20$.

C.3 Stability analysis of isotropic spheroids

We derive the stability of the isotropic state $Q_{ij} = 0 + Q'_{ij}$ by expanding the Beris-Edwards equation to first order in the perturbation parameter $Q'_{ij} = \epsilon(n_i n_j - \delta_{ij}/3)$,

$$D_t Q'_{ij} - \mathcal{W}_{ij} = \Gamma K_{LC} \left(\partial_k \partial_k Q'_{ij} \right) + \mathcal{O}(\epsilon^2) \,. \tag{C.9}$$

To keep the nematic tensor traceless in the presence of sources and sinks, $E_{kk} \neq 0$, we are using the traceless strain rate tensor $\tilde{E}_{ij} = (E_{ij} - E_{kk}\delta_{ij}/3)$ in the co-rotation term. Following eqn. (2.20), the leading order contribution of the co-rotation term $\mathcal{W}_{ij}$ is

$$\mathcal{W}_{ij} = \frac{2}{3}\xi \tilde{E}_{ij} + \mathcal{O}(\epsilon) \,, \tag{C.10}$$

where we have used the symmetries of $\tilde{E}_{ij}$ and Q'_{ij}. The stability of the isotropic state is thus governed by

$$\dot{Q}_{ij} = \frac{2}{3}\xi \left(E_{ij} - \delta_{ij} \frac{E_{kk}}{3} \right) + \mathcal{O}(\epsilon) \,, \tag{C.11}$$

where we have neglected the advection term, $u_k \partial_k Q_{ij}$, since spatial gradients $\nabla \mathbf{Q}$ vanish in the isotropic state. In spherical coordinates, the strain rate tensor $E_{ij} = (\partial_j u_i + \partial_i u_j)/2$ has components

$$E_{rr} = \partial_r u_r \,, \tag{C.12}$$

$$E_{\theta\theta} = E_{\phi\phi} = \frac{u_r}{r} \,, \tag{C.13}$$

$$E_{r\theta} = E_{r\phi} = E_{\theta\phi} = 0 \,, \tag{C.14}$$

where we have used the symmetry of the flow field $\mathbf{u}(r, \theta, \phi) = u_r(r)\hat{\mathbf{r}}$. This yields the initial growth rate of the radial component of the nematic order,

$$\dot{Q}_{rr} = \frac{4}{9}\xi \left(\partial_r u_r - \frac{u_r}{r} \right) \,. \tag{C.15}$$

References

1. Ruske, L. J. & Yeomans, J. M. Morphology of active deformable 3D droplets. *Physical Review X* **11,** 021001 (2021).
2. Ruske, L. J. & Yeomans, J. M. Activity gradients in two-and three-dimensional active nematics. *Soft Matter* **18,** 5654–5661 (2022).
3. Ruske, L. J. & Yeomans, J. M. Activity-driven tissue alignment in proliferating spheroids. *Soft Matter* **19,** 921–931 (2023).
4. Ruske, L. J. *et al.* Topological defects drive stress-shape misalignment in confluent cell layers (in preparation).
5. Hadjifrangiskou, I., Ruske, L. J. & Yeomans, J. M. Active nematics with deformable particle (in preparation).
6. Ruske, L. J. *et al.* Coupled differentiation and division of embryonic stem cells inferred from clonal snapshots. *Physical Biology* **17,** 065009 (2020).
7. Angelini, T. E. *et al.* Glass-like dynamics of collective cell migration. *Proceedings of the National Academy of Sciences* **108,** 4714–4719 (2011).
8. Schoetz, E.-M., Lanio, M., Talbot, J. A. & Manning, M. L. Glassy dynamics in three-dimensional embryonic tissues. *Journal of The Royal Society Interface* **10,** 20130726 (2013).
9. Sadati, M., Qazvini, N. T., Krishnan, R., Park, C. Y. & Fredberg, J. J. Collective migration and cell jamming. *Differentiation* **86,** 121–125 (2013).
10. Park, J.-A. *et al.* Unjamming and cell shape in the asthmatic airway epithelium. *Nature materials* **14,** 1040–1048 (2015).
11. Oswald, L., Grosser, S., Smith, D. M. & Käs, J. A. Jamming transitions in cancer. *Journal of physics D: Applied physics* **50,** 483001 (2017).
12. Mongera, A. *et al.* A fluid-to-solid jamming transition underlies vertebrate body axis elongation. *Nature* **561,** 401–405 (2018).
13. Park, J.-A., Atia, L., Mitchel, J. A., Fredberg, J. J. & Butler, J. P. Collective migration and cell jamming in asthma, cancer and development. *Journal of cell science* **129,** 3375–3383 (2016).
14. Trappe, V., Prasad, V., Cipelletti, L., Segre, P. & Weitz, D. A. Jamming phase diagram for attractive particles. *Nature* **411,** 772–775 (2001).
15. Bi, D., Yang, X., Marchetti, M. C. & Manning, M. L. Motility-driven glass and jamming transitions in biological tissues. *Physical Review X* **6,** 021011 (2016).
16. Ranft, J. *et al.* Fluidization of tissues by cell division and apoptosis. *Proceedings of the National Academy of Sciences* **107,** 20863–20868 (2010).

17. Bi, D., Lopez, J. H., Schwarz, J. M. & Manning, M. L. Energy barriers and cell migration in densely packed tissues. *Soft matter* **10,** 1885–1890 (2014).

18. Bi, D., Lopez, J., Schwarz, J. M. & Manning, M. L. A density-independent rigidity transition in biological tissues. *Nature Physics* **11,** 1074–1079 (2015).

19. Shellard, A. & Mayor, R. Supracellular migration–beyond collective cell migration. *Journal of cell science* **132,** jcs226142 (2019).

20. Ladoux, B. & Mège, R.-M. Mechanobiology of collective cell behaviours. *Nature reviews Molecular cell biology* **18,** 743–757 (2017).

21. Chen, T., Saw, T. B., Mège, R.-M. & Ladoux, B. Mechanical forces in cell monolayers. *Journal of Cell Science* **131,** jcs218156 (2018).

22. Jülicher, F., Grill, S. W. & Salbreux, G. Hydrodynamic theory of active matter. *Reports on Progress in Physics* **81,** 076601 (2018).

23. Doostmohammadi, A., Ignés-Mullol, J., Yeomans, J. M. & Sagués, F. Active nematics. *Nature Communications* **9,** 1–13 (2018).

24. Marchetti, M. C. *et al.* Hydrodynamics of soft active matter. *Reviews of Modern Physics* **85,** 1143 (2013).

25. Keber, F. C. *et al.* Topology and dynamics of active nematic vesicles. *Science* **345,** 1135–1139 (2014).

26. Zhang, R., Zhou, Y., Rahimi, M. & De Pablo, J. J. Dynamic structure of active nematic shells. *Nature Communications* **7,** 1–9 (2016).

27. Lee, G. *et al.* Myosin-driven actin-microtubule networks exhibit self-organized contractile dynamics. *Science Advances* **7,** eabe4334 (2021).

28. Narayan, V., Ramaswamy, S. & Menon, N. Long-lived giant number fluctuations in a swarming granular nematic. *Science* **317,** 105–108 (2007).

29. Yaman, Y. I., Demir, E., Vetter, R. & Kocabas, A. Emergence of active nematics in chaining bacterial biofilms. *Nature Communications* **10,** 1–9 (2019).

30. Saw, T. B. *et al.* Topological defects in epithelia govern cell death and extrusion. *Nature* **544,** 212–216 (2017).

31. Duclos, G., Garcia, S., Yevick, H. & Silberzan, P. Perfect nematic order in confined monolayers of spindle-shaped cells. *Soft Matter* **10,** 2346–2353 (2014).

32. Mueller, R., Yeomans, J. M. & Doostmohammadi, A. Emergence of active nematic behavior in monolayers of isotropic cells. *Physical Review Letters* **122,** 048004 (2019).

33. Duclos, G., Erlenkämper, C., Joanny, J.-F. & Silberzan, P. Topological defects in confined populations of spindle-shaped cells. *Nature Physics* **13,** 58–62 (2017).

34. Saw, T. B., Xi, W., Ladoux, B. & Lim, C. T. Biological tissues as active nematic liquid crystals. *Advanced Materials* **30,** 1802579 (2018).

35. Vromans, A. J. & Giomi, L. Orientational properties of nematic disclinations. *Soft Matter* **12,** 6490–6495 (2016).

36. Binysh, J., Kos, Ž., Čopar, S., Ravnik, M. & Alexander, G. P. Three-Dimensional Active Defect Loops. *Physical Review Letters* **124,** 088001 (2020).

37. Duclos, G. *et al.* Topological structure and dynamics of three-dimensional active nematics. *Science* **367,** 1120–1124 (2020).

38. Čopar, S., Aplinc, J., Kos, Ž., Žumer, S. & Ravnik, M. Topology of three-dimensional active nematic turbulence confined to droplets. *Physical Review X* **9,** 031051 (2019).

39. Copenhagen, K., Alert, R., Wingreen, N. S. & Shaevitz, J. W. Topological defects promote layer formation in Myxococcus xanthus colonies. *Nature Physics* **17,** 211–215 (2021).

40. Maroudas-Sacks, Y. *et al.* Topological defects in the nematic order of actin fibres as organization centres of Hydra morphogenesis. *Nature Physics* **17,** 251–259 (2021).

41. Guillamat, P., Blanch-Mercader, C., Pernollet, G., Kruse, K. & Roux, A. Integer topological defects organize stresses driving tissue morphogenesis. *Nature materials* **21,** 588–597 (2022).

42. Zhang, J., Yang, N., Kreeger, P. K. & Notbohm, J. Topological defects in the mesothelium suppress ovarian cancer cell clearance. *APL bioengineering* **5,** 036103 (2021).

43. Delarue, M., Joanny, J.-F., Jülicher, F. & Prost, J. Stress distributions and cell flows in a growing cell aggregate. *Interface Focus* **4,** 20140033 (2014).

44. Montel, F. *et al.* Isotropic stress reduces cell proliferation in tumor spheroids. *New Journal of Physics* **14,** 055008 (2012).

45. Alessandri, K. *et al.* Cellular capsules as a tool for multicellular spheroid production and for investigating the mechanics of tumor progression in vitro. *Proceedings of the National Academy of Sciences* **110,** 14843–14848 (2013).

46. Vasilica Stirbat, T. *et al.* Multicellular aggregates: a model system for tissue rheology. *The European Physical Journal E* **36,** 1–14 (2013).

47. Bird, R., Dotson, P. & Johnson, N. Polymer solution rheology based on a finitely extensible bead—spring chain model. *Journal of Non-Newtonian Fluid Mechanics* **7,** 213–235 (1980).

48. Cahn, J. W. & Hilliard, J. E. Free energy of a nonuniform system. I. Interfacial free energy. *The Journal of Chemical Physics* **28,** 258–267 (1958).

49. Lázaro, G. R., Pagonabarraga, I. & Hernández-Machado, A. Phase-field theories for mathematical modeling of biological membranes. *Chemistry and physics of lipids* **185,** 46–60 (2015).

50. De Gennes, P.-G. & Prost, J. *The Physics of Liquid Crystals* (Oxford university press, 1993).

51. Stramer, B. & Mayor, R. Mechanisms and in vivo functions of contact inhibition of locomotion. *Nature reviews Molecular cell biology* **18,** 43–55 (2017).

52. Vafa, F., Bowick, M. J., Shraiman, B. I. & Marchetti, M. C. Fluctuations can induce local nematic order and extensile stress in monolayers of motile cells. *Soft Matter* **17,** 3068–3073 (2021).

53. Killeen, A., Bertrand, T. & Lee, C. F. Polar fluctuations lead to extensile nematic behavior in confluent tissues. *Physical Review Letters* **128,** 078001 (2022).

54. Onsager, L. The effects of shape on the interaction of colloidal particles. *Annals of the New York Academy of Sciences* **51,** 627–659 (1949).

55. Vink, R. L. Crossover from a Kosterlitz-Thouless phase transition to a discontinuous phase transition in two-dimensional liquid crystals. *Physical Review E* **90,** 062132 (2014).

56. Frank, F. C. I. Liquid crystals. On the theory of liquid crystals. *Discussions of the Faraday Society* **25,** 19–28 (1958).

57. Norton, M. M. *et al.* Insensitivity of active nematic liquid crystal dynamics to topological constraints. *Physical Review E* **97,** 012702 (2018).

58. Zhang, R., Kumar, N., Ross, J. L., Gardel, M. L. & De Pablo, J. J. Interplay of structure, elasticity, and dynamics in actin-based nematic materials. *Proceedings of the National Academy of Sciences* **115,** E124–E133 (2018).

59. Schimming, C. D. & Viñals, J. Anisotropic disclination cores in nematic liquid crystals modeled by a self-consistent molecular field theory. *Physical Review E* **102,** 010701 (2020).

60. Farhadifar, R., Röper, J.-C., Aigouy, B., Eaton, S. & Jülicher, F. The influence of cell mechanics, cell-cell interactions, and proliferation on epithelial packing. *Current Biology* **17,** 2095–2104 (2007).

61. Kemkemer, R., Kling, D., Kaufmann, D. & Gruler, H. Elastic properties of nematoid arrangements formed by amoeboid cells. *The European Physical Journal E* **1,** 215–225 (2000).

62. Kemkemer, R., Teichgräber, V., Schrank-Kaufmann, S., Kaufmann, D. & Gruler, H. Nematic order-disorder state transition in a liquid crystal analogue formed by oriented and migrating amoeboid cells. *The European Physical Journal E* **3,** 101–110 (2000).

63. Duclos, G. *et al.* Spontaneous shear flow in confined cellular nematics. *Nature Physics* **14,** 728–732 (2018).

64. Dell'Arciprete, D. *et al.* A growing bacterial colony in two dimensions as an active nematic. *Nature Communications* **9,** 1–9 (2018).

65. Čopar, S. Topology and geometry of nematic braids. *Physics Reports* **538,** 1–37 (2014).

66. Beris, A. N. & Edwards, B. J. *Thermodynamics of flowing systems with internal microstructure* eng (Oxford University Press, New York ; Oxford, 1994).

67. Marenduzzo, D., Orlandini, E., Cates, M. & Yeomans, J. Steady-state hydrodynamic instabilities of active liquid crystals: Hybrid lattice Boltzmann simulations. *Physical Review E* **76,** 031921 (2007).

68. Marenduzzo, D., Orlandini, E. & Yeomans, J. M. Hydrodynamics and rheology of active liquid crystals: a numerical investigation. *Physical Review Letters* **98,** 118102 (2007).

69. Leslie, F. M. Some constitutive equations for liquid crystals. *Archive for Rational Mechanics and Analysis* **28,** 265–283 (1968).

70. Ericksen, J. L. Conservation laws for liquid crystals. *Transactions of the Society of Rheology* **5,** 23–34 (1961).

71. Ericksen, J. Transversely isotropic fluids. *Kolloid-Zeitschrift* **173,** 117–122 (1960).

72. Jeffery, G. B. The motion of ellipsoidal particles immersed in a viscous fluid. *Proceedings of the Royal Society of London. Series A, Containing papers of a mathematical and physical character* **102,** 161–179 (1922).

73. Bischofs, I. B. & Schwarz, U. S. Cell organization in soft media due to active mechanosensing. *Proceedings of the National Academy of Sciences* **100,** 9274–9279 (2003).

74. Kurpinski, K., Chu, J., Hashi, C. & Li, S. Anisotropic mechanosensing by mesenchymal stem cells. *Proceedings of the National Academy of Sciences* **103,** 16095–16100 (2006).

75. Merkel, M. *et al.* Triangles bridge the scales: Quantifying cellular contributions to tissue deformation. *Physical Review E* **95,** 032401 (2017).

76. Etournay, R. *et al.* Interplay of cell dynamics and epithelial tension during morphogenesis of the Drosophila pupal wing. *Elife* **4,** e07090 (2015).

77. Simha, R. A. & Ramaswamy, S. Hydrodynamic fluctuations and instabilities in ordered suspensions of self-propelled particles. *Physical Review Letters* **89,** 058101 (2002).

78. Thampi, S. P., Golestanian, R. & Yeomans, J. M. Vorticity, defects and correlations in active turbulence. *Philosophical Transactions of the Royal Society A: Mathematical, Physical and Engineering Sciences* **372,** 20130366 (2014).

79. Ramaswamy, S. & Rao, M. Active-filament hydrodynamics: instabilities, boundary conditions and rheology. *New Journal of Physics* **9,** 423 (2007).

80. Thampi, S. & Yeomans, J. Active turbulence in active nematics. *The European Physical Journal Special Topics* **225,** 651–662 (2016).

81. Carenza, L. N., Gonnella, G., Marenduzzo, D. & Negro, G. Rotation and propulsion in 3D active chiral droplets. *Proceedings of the National Academy of Sciences* **116,** 22065–22070 (2019).

82. Carenza, L., Gonnella, G., Marenduzzo, D. & Negro, G. Chaotic and periodical dynamics of active chiral droplets. *Physica A: Statistical Mechanics and its Applications* **559,** 125025 (2020).

83. Blanch-Mercader, C. & Casademunt, J. Hydrodynamic instabilities, waves and turbulence in spreading epithelia. *Soft Matter* **13,** 6913–6928 (2017).

84. Blow, M. L., Thampi, S. P. & Yeomans, J. M. Biphasic, lyotropic, active nematics. *Physical Review Letters* **113,** 248303 (2014).

85. Doostmohammadi, A., Thampi, S. P. & Yeomans, J. M. Defect-mediated morphologies in growing cell colonies. *Physical review letters* **117,** 048102 (2016).

86. Helfrich, W. Elastic properties of lipid bilayers: theory and possible experiments. *Zeitschrift für Naturforschung C* **28,** 693–703 (1973).

87. Forgacs, G., Foty, R. A., Shafrir, Y. & Steinberg, M. S. Viscoelastic properties of living embryonic tissues: a quantitative study. *Biophysical journal* **74,** 2227–2234 (1998).

88. Duclut, C., Sarkar, N., Prost, J. & Jülicher, F. Fluid pumping and active flexoelectricity can promote lumen nucleation in cell assemblies. *Proceedings of the National Academy of Sciences* **116,** 19264–19273 (2019).

89. Stirbat, T. V. *et al.* Fine tuning of tissues' viscosity and surface tension through contractility suggests a new role for α-catenin. *PLoS One* **8,** e52554 (2013).

90. Guevorkian, K., Colbert, M.-J., Durth, M., Dufour, S. & Brochard-Wyart, F. Aspiration of biological viscoelastic drops. *Physical review letters* **104,** 218101 (2010).

91. Mgharbel, A., Delanoë-Ayari, H. & Rieu, J.-P. Measuring accurately liquid and tissue surface tension with a compression plate tensiometer. *HFSP journal* **3,** 213–221 (2009).

92. Fouchard, J. *et al.* Curling of epithelial monolayers reveals coupling between active bending and tissue tension. *Proceedings of the National Academy of Sciences* **117,** 9377–9383 (2020).

93. Trushko, A. *et al.* Buckling of epithelium growing under spherical confinement. *BioRxiv,* 513119 (2020).

94. Han, Y. L. *et al.* Cell contraction induces long-ranged stress stiffening in the extracellular matrix. *Proceedings of the National Academy of Sciences* **115,** 4075–4080 (2018).

95. Solon, J., Levental, I., Sengupta, K., Georges, P. C. & Janmey, P. A. Fibroblast adaptation and stiffness matching to soft elastic substrates. *Biophysical journal* **93,** 4453–4461 (2007).

96. Kuznetsova, T. G., Starodubtseva, M. N., Yegorenkov, N. I., Chizhik, S. A. & Zhdanov, R. I. Atomic force microscopy probing of cell elasticity. *Micron* **38,** 824–833 (2007).

97. Blumlein, A., Williams, N. & McManus, J. J. The mechanical properties of individual cell spheroids. *Scientific Reports* **7,** 1–10 (2017).

98. Marmottant, P. *et al.* The role of fluctuations and stress on the effective viscosity of cell aggregates. *Proceedings of the National Academy of Sciences* **106,** 17271–17275 (2009).

99. Shendruk, T. N., Thijssen, K., Yeomans, J. M. & Doostmohammadi, A. Twist-induced crossover from two-dimensional to three-dimensional turbulence in active nematics. *Physical Review E* **98,** 010601 (2018).

100. Rozman, J., Krajnc, M. & Ziherl, P. Collective cell mechanics of epithelial shells with organoid-like morphologies. *Nature communications* **11,** 1–9 (2020).

101. Sanchez, T., Chen, D. T., DeCamp, S. J., Heymann, M. & Dogic, Z. Spontaneous motion in hierarchically assembled active matter. *Nature* **491,** 431–434 (2012).

102. Blanch-Mercader, C. *et al.* Turbulent dynamics of epithelial cell cultures. *Physical Review Letters* **120,** 208101 (2018).

103. Schuppler, M., Keber, F. C., Kröger, M. & Bausch, A. R. Boundaries steer the contraction of active gels. *Nature Communications* **7,** 1–10 (2016).

104. Maroudas-Sacks, Y. *et al.* Topological defects in the nematic order of actin fibers as organization centers of Hydra morphogenesis. *bioRxiv* (2020).

105. Friedl, P. & Gilmour, D. Collective cell migration in morphogenesis, regeneration and cancer. *Nature Reviews Molecular Cell Biology* **10,** 445–457 (2009).

106. He, B., Doubrovinski, K., Polyakov, O. & Wieschaus, E. Apical constriction drives tissue-scale hydrodynamic flow to mediate cell elongation. *Nature* **508,** 392–396 (2014).

107. Friedl, P. & Alexander, S. Cancer invasion and the microenvironment: plasticity and reciprocity. *Cell* **147,** 992–1009 (2011).

108. Ewald, A. J., Brenot, A., Duong, M., Chan, B. S. & Werb, Z. Collective epithelial migration and cell rearrangements drive mammary branching morphogenesis. *Developmental Cell* **14,** 570–581 (2008).

109. Kusters, R. *et al.* Actin shells control buckling and wrinkling of biomembranes. *Soft Matter* **15,** 9647–9653 (2019).

110. Buccione, R., Orth, J. D. & McNiven, M. A. Foot and mouth: podosomes, invadopodia and circular dorsal ruffles. *Nature Reviews Molecular Cell Biology* **5,** 647–657 (2004).

111. Hoon, J.-L., Wong, W.-K. & Koh, C.-G. Functions and regulation of circular dorsal ruffles. *Molecular and Cellular Biology* **32,** 4246–4257 (2012).

112. Echarri, A. & Del Pozo, M. A. Caveolae–mechanosensitive membrane invaginations linked to actin filaments. *Journal of Cell Science* **128,** 2747–2758 (2015).

113. Swanson, J. A. Shaping cups into phagosomes and macropinosomes. *Nature Reviews Molecular Cell Biology* **9,** 639–649 (2008).

114. Doherty, G. J. & McMahon, H. T. Mechanisms of endocytosis. *Annual Review of Biochemistry* **78,** 857–902 (2009).

115. Tjhung, E., Cates, M. E. & Marenduzzo, D. Contractile and chiral activities codetermine the helicity of swimming droplet trajectories. *Proceedings of the National Academy of Sciences* **114,** 4631–4636 (2017).

116. Tjhung, E., Marenduzzo, D. & Cates, M. E. Spontaneous symmetry breaking in active droplets provides a generic route to motility. *Proceedings of the National Academy of Sciences* **109,** 12381–12386 (2012).

117. Metselaar, L., Yeomans, J. M. & Doostmohammadi, A. Topology and morphology of self-deforming active shells. *Physical Review Letters* **123,** 208001 (2019).

118. Zhang, R. *et al.* Spatiotemporal control of liquid crystal structure and dynamics through activity patterning. *Nature Materials* **20,** 875–882 (2021).

119. Shankar, S. & Marchetti, M. C. Hydrodynamics of active defects: from order to chaos to defect ordering. *Physical Review X* **9,** 041047 (2019).

120. Tang, X. & Selinger, J. V. Alignment of a topological defect by an activity gradient. *Physical Review E* **103,** 022703 (2021).

121. Mozaffari, A., Zhang, R., Atzin, N. & de Pablo, J. J. Defect Spirograph: Dynamical Behavior of Defects in Spatially Patterned Active Nematics. *Physical Review Letters* **126,** 227801 (2021).

122. Bhattacharyya, S. & Yeomans, J. M. Coupling Turing stripes to active flows. *Soft Matter* **17,** 10716–10722 (2021).

123. Giomi, L. Geometry and topology of turbulence in active nematics. *Physical Review X* **5,** 031003 (2015).

124. Streichan, S. J., Lefebvre, M. F., Noll, N., Wieschaus, E. F. & Shraiman, B. I. Global morphogenetic flow is accurately predicted by the spatial distribution of myosin motors. *Elife* **7,** e27454 (2018).

125. Mason, F. M., Tworoger, M. & Martin, A. C. Apical domain polarization localizes actin–myosin activity to drive ratchet-like apical constriction. *Nature Cell Biology* **15,** 926–936 (2013).

126. Jagiella, N., Müller, B., Müller, M., Vignon-Clementel, I. E. & Drasdo, D. Inferring growth control mechanisms in growing multi-cellular spheroids of NSCLC cells from spatial-temporal image data. *PLoS Computational Biology* **12,** e1004412 (2016).

127. Delarue, M. *et al.* Mechanical control of cell flow in multicellular spheroids. *Physical Review Letters* **110,** 138103 (2013).

128. Alberts, B. *Molecular Biology of the Cell* (Garland Science, 2008).

129. Pollard, T. D. & Borisy, G. G. Cellular motility driven by assembly and disassembly of actin filaments. *Cell* **112,** 453–465 (2003).

130. Dogterom, M., Kerssemakers, J. W., Romet-Lemonne, G. & Janson, M. E. Force generation by dynamic microtubules. *Current Opinion in Cell Biology* **17,** 67–74 (2005).

131. Hirschhaeuser, F. *et al.* Multicellular tumor spheroids: an underestimated tool is catching up again. *Journal of Biotechnology* **148,** 3–15 (2010).

132. Doostmohammadi, A. *et al.* Celebrating Soft Matter's 10th Anniversary: Cell division: a source of active stress in cellular monolayers. *Soft Matter* **11,** 7328–7336 (2015).

133. Pachenari, M. *et al.* Mechanical properties of cancer cytoskeleton depend on actin filaments to microtubules content: investigating different grades of colon cancer cell lines. *Journal of Biomechanics* **47,** 373–379 (2014).

134. Li, Q., Lee, G. Y., Ong, C. N. & Lim, C. T. AFM indentation study of breast cancer cells. *Biochemical and Biophysical Research Communications* **374,** 609–613 (2008).

135. Nematbakhsh, Y., Pang, K. T. & Lim, C. T. Correlating the viscoelasticity of breast cancer cells with their malignancy. *Convergent Science Physical Oncology* **3,** 034003 (2017).

136. Martin, M. & Risler, T. Viscocapillary instability in cellular spheroids. *New Journal of Physics* **23,** 033032 (2021).

137. Desmaison, A. *et al.* Impact of physical confinement on nuclei geometry and cell division dynamics in 3D spheroids. *Scientific Reports* **8,** 1–8 (2018).

138. Alert, R., Joanny, J.-F. & Casademunt, J. Universal scaling of active nematic turbulence. *Nature Physics* **16,** 682–688 (2020).

139. Eisenberg, M. & Guy, R. A proof of the hairy ball theorem. *The American Mathematical Monthly* **86,** 571–574 (1979).

140. Opathalage, A. *et al.* Self-organized dynamics and the transition to turbulence of confined active nematics. *Proceedings of the National Academy of Sciences* **116,** 4788–4797 (2019).

141. Gao, T., Betterton, M. D., Jhang, A.-S. & Shelley, M. J. Analytical structure, dynamics, and coarse graining of a kinetic model of an active fluid. *Physical Review Fluids* **2,** 093302 (2017).

142. Young, Y.-N., Shelley, M. J. & Stein, D. B. The many behaviors of deformable active droplets. *Mathematical Biosciences and Engineering* **18,** 2849–2881 (2021).

143. Yerushalmi, R., Woods, R., Ravdin, P. M., Hayes, M. M. & Gelmon, K. A. Ki67 in breast cancer: prognostic and predictive potential. *The Lancet Oncology* **11,** 174–183 (2010).

144. Sakaue-Sawano, A. *et al.* Visualizing spatiotemporal dynamics of multicellular cell-cycle progression. *Cell* **132,** 487–498 (2008).

145. Sutherland, R. M. Cell and environment interactions in tumor microregions: the multicell spheroid model. *Science* **240,** 177–184 (1988).

146. Laurent, J. *et al.* Multicellular tumor spheroid models to explore cell cycle checkpoints in 3D. *BMC Cancer* **13,** 1–12 (2013).

147. LaRue, K. E., Khalil, M. & Freyer, J. P. Microenvironmental regulation of proliferation in multicellular spheroids is mediated through differential expression of cyclin-dependent kinase inhibitors. *Cancer Research* **64,** 1621–1631 (2004).

148. Lee, W. *et al.* Dispersible hydrogel force sensors reveal patterns of solid mechanical stress in multicellular spheroid cultures. *Nature Communications* **10,** 1–14 (2019).

149. Eidukevicius, R. *et al.* A method to estimate cell cycle time and growth fraction using bromodeoxyuridine-flow cytometry data from a single sample. *BMC Cancer* **5,** 1–11 (2005).

150. Nam, S. & Chaudhuri, O. Mitotic cells generate protrusive extracellular forces to divide in three-dimensional microenvironments. *Nature Physics* **14,** 621–628 (2018).

151. Lucio, A. A. *et al.* Spatiotemporal variation of endogenous cell-generated stresses within 3D multicellular spheroids. *Scientific Reports* **7,** 1–11 (2017).

152. Valencia, A. M. J. *et al.* Collective cancer cell invasion induced by coordinated contractile stresses. *Oncotarget* **6,** 43438 (2015).

153. Aigouy, B. *et al.* Cell flow reorients the axis of planar polarity in the wing epithelium of Drosophila. *Cell* **142,** 773–786 (2010).

154. Tambe, D. T. *et al.* Collective cell guidance by cooperative intercellular forces. *Nature materials* **10,** 469–475 (2011).

155. Balasubramaniam, L. *et al.* Investigating the nature of active forces in tissues reveals how contractile cells can form extensile monolayers. *Nature materials* **20,** 1156–1166 (2021).

156. Pellegrin, S. & Mellor, H. Actin stress fibres. *Journal of cell science* **120,** 3491–3499 (2007).

157. Lehtimäki, J. I., Rajakylä, E. K., Tojkander, S. & Lappalainen, P. Generation of stress fibers through myosin-driven reorganization of the actin cortex. *Elife* **10,** e60710 (2021).

158. Yoshigi, M., Clark, E. B. & Yost, H. J. Quantification of stretch-induced cytoskeletal remodeling in vascular endothelial cells by image processing. *Cytometry Part A: The Journal of the International Society for Analytical Cytology* **55,** 109–118 (2003).

159. Marusyk, A. & Polyak, K. Tumor heterogeneity: causes and consequences. *Biochimica et Biophysica Acta (BBA)-Reviews on Cancer* **1805,** 105–117 (2010).

160. Bhattacharyya, S. & Yeomans, J. M. Phase Separation Driven by Active Flows. *arXiv preprint arXiv:2302.00153* (2023).

161. Norton, M. M., Grover, P., Hagan, M. F. & Fraden, S. Optimal control of active nematics. *Physical review letters* **125,** 178005 (2020).

162. Emmanuel, L., Yeomans, J. M. & Doostmohammadi, A. Activity pulses induce spontaneous flow reversals in viscoelastic environments. *Journal of the Royal Society Interface* **18** (2021).

163. Emmanuel, L., Le Thi, H., Yeomans, J. M. & Doostmohammadi, A. Self-sustained oscillations of active viscoelastic matter. *Journal of Physics A: Mathematical and Theoretical* **55,** 275601 (2022).

164. Delarue, M. *et al.* Compressive stress inhibits proliferation in tumor spheroids through a volume limitation. *Biophysical Journal* **107,** 1821–1828 (2014).

165. Ehrbar, M. *et al.* Elucidating the role of matrix stiffness in 3D cell migration and remodeling. *Biophysical journal* **100,** 284–293 (2011).

166. Pathak, A. & Kumar, S. Independent regulation of tumor cell migration by matrix stiffness and confinement. *Proceedings of the National Academy of Sciences* **109,** 10334–10339 (2012).

167. Emmanuel, L., Yeomans, J. M. & Doostmohammadi, A. Active matter in a viscoelastic environment. *Physical Review Fluids* **5,** 023102 (2020).

168. Desmaison, A., Frongia, C., Grenier, K., Ducommun, B. & Lobjois, V. Mechanical stress impairs mitosis progression in multi-cellular tumor spheroids. *PloS One* **8,** e80447 (2013).

169. Krüger, T. *et al. The lattice Boltzmann method* **978-3,** 4–15 (Springer, 2017).

170. Denniston, C., Marenduzzo, D., Orlandini, E. & Yeomans, J. Lattice Boltzmann algorithm for three–dimensional liquid–crystal hydrodynamics. *Philosophical Transactions of the Royal Society of London. Series A: Mathematical, Physical and Engineering Sciences* **362,** 1745–1754 (2004).

171. Zapotocky, M., Goldbart, P. M. & Goldenfeld, N. Kinetics of phase ordering in uniaxial and biaxial nematic films. *Physical Review E* **51,** 1216 (1995).

172. Hobdell, J. & Windle, A. A numerical technique for predicting microstructure in liquid crystalline polymers. *Liquid Crystals* **23,** 157–173 (1997).

173. Tran, L. *et al.* Lassoing saddle splay and the geometrical control of topological defects. *Proceedings of the National Academy of Sciences* **113,** 7106–7111 (2016).